

# OPTIMIZED BEAMFORMING AND LIMITED ANGLE TOMOGRAPHY OF THE COMPRESSED BREAST

by

Fong Ming Hooi

A dissertation submitted in partial fulfillment  
of the requirements for the degree of  
Doctor of Philosophy  
(Biomedical Engineering)  
in The University of Michigan  
2012

Doctoral Committee:

Professor Paul L. Carson, Chair  
Associate Professor Jeff Fessler  
Assistant Research Professor Oliver Kripfgans  
Assistant Professor Zhen Xu  
Chief Technologist Kai Thomenius, General Electric Co.

Brick walls are there for a reason. The brick walls are not there to keep us out. The brick walls are there to give us a chance to show how badly we want something. Because the brick walls are there to stop the people who don't want it badly enough.

---

RANDY PAUSCH (1960-2008)

© Fong Ming Hooi

---

All rights reserved  
2012

*Dedicated to my family, especially Mom and Dad, who have offered me unconditional love and support,  
and for the one who stands by me every step of the way, Dan.*

ACKNOWLEDGMENTS I would like to first acknowledge my advisor, Paul Carson, for all his advice and guidance along my graduate school career.

Without him, this dissertation would not have been possible, in more ways than one.

I would also like to thank my committee members, Jeff Fessler, Oliver Kripfgans, Zhen Xu, and Kai Thomenius, for their valuable input on my research topic and insight into improving my dissertation.

I thank the members of BRS, old and new, for their help in setting up various experiments and hunting down lab equipment, which was a monumental task in itself at times. Special thanks goes out to Fouzaan Zafar, who has spent countless hours debugging hardware with me to get speed of sound data acquisitions going, Oliver again, in so many ways, from debugging experimental setups to generously providing access to *hausboot* to run my massive computations. I owe Sumedha Sinha and Takashi Kozai my sanity, for their friendship kept me going and reminded me to relax and leave the apartment (from time to time). Last, but not least, I have to thank Sacha Verweij for his tremendous help and support within the last year, offering relevant advice that affects not only, but transcends beyond, this thesis.

# TABLE OF CONTENTS

|  |           |
|--|-----------|
| DEDICATION . . . . .   | ii        |
| ACKNOWLEDGMENTS . . . . .  | iii       |
| LIST OF FIGURES . . . . .  | vi        |
| LIST OF TABLES . . . . .   | ix        |
| <br><b>CHAPTER</b>   |           |
| <b>I. Breast Cancer Imaging . . . . .</b>                                    | <b>1</b>  |
| 1.1 Background and Significance . . . . .                                    | 1         |
| 1.2 Specific Aims . . . . .  | 5         |
| <b>II. Optimized Beamforming with 2D Reconfigurable Arrays . . . . .</b>     | <b>20</b> |
| 2.1 Benefits of Annular Arrays . . . . .                                     | 20        |
| 2.2 Constructing Beam with Extended Focus . . . . .                          | 21        |
| 2.2.1 Transmitted Beam Optimization . . . . .                                | 21        |
| 2.2.2 Comparison with purely spherical beams . . . . .                       | 26        |
| 2.2.3 Beam Steering . . . . .  | 26        |
| 2.3 Results . . . . .  | 29        |
| 2.3.1 Beam Optimization . . . . .  | 29        |
| 2.3.2 Comparison with Purely Spherical Beams . . . . .                       | 33        |
| 2.3.3 Beam Steering . . . . .  | 33        |
| 2.4 Discussion . . . . .   | 36        |
| 2.4.1 Beam Optimization . . . . .  | 36        |
| 2.4.2 Comparison with Purely Spherical Beams . . . . .                       | 38        |
| 2.4.3 Beam Steering . . . . .  | 42        |
| 2.5 Conclusion . . . . .   | 42        |
| <b>III. Speed of Sound Imaging using First Arrival Traveltimes . . . . .</b> | <b>48</b> |
| 3.1 Background . . . . .   | 48        |
| 3.2 Inverse Theory . . . . .   | 50        |
| 3.3 Application . . . . .  | 54        |
| 3.3.1 Eikonal Forward Model . . . . .  | 54        |
| 3.3.2 Cost Function Minimization via Conjugate Gradient Updates . . . . .    | 55        |

|            |  |            |
|------------|--|------------|
| 3.3.3      | Choice of Covariance Matrices . . . . .  | 55         |
| 3.3.4      | Experimental Setup . . . . .   | 57         |
| 3.4        | Results . . . . .  | 60         |
| 3.4.1      | Simulated Speed of Sound Reconstructions . . . . .   | 60         |
| 3.4.2      | Speed of Sound Reconstructions with Experimental<br>Data . . . . .   | 68         |
| 3.5        | Discussion . . . . .   | 73         |
| 3.6        | Conclusion . . . . .   | 76         |
| <b>IV.</b> | <b>Attenuation Imaging . . . . .</b>   | <b>80</b>  |
| 4.1        | Background . . . . .   | 80         |
| 4.2        | Inverse Theory . . . . .   | 81         |
| 4.2.1      | Generating Attenuation Data . . . . .  | 82         |
| 4.2.2      | Covariance Matrices . . . . .  | 83         |
| 4.2.3      | Full Wave Model . . . . .  | 84         |
| 4.3        | Results . . . . .  | 85         |
| 4.3.1      | Forward Wave Propagation Model . . . . .   | 85         |
| 4.3.2      | Experimental Data . . . . .  | 85         |
| 4.3.3      | Reconstruction . . . . .   | 87         |
| 4.4        | Discussion . . . . .   | 92         |
| 4.5        | Conclusion . . . . .   | 97         |
| <b>V.</b>  | <b>Reconstruction Algorithm Refinements for Grayscale, Speed<br/>of Sound, and Attenuation Imaging . . . . .</b> | <b>101</b> |
| 5.1        | Summary of Developed Algorithms . . . . .  | 101        |
| 5.2        | Future Work . . . . .  | 102        |

# LIST OF FIGURES

|        |  |    |
|--------|--|----|
| Figure |  |    |
| 1.1    | Acoustic properties of normal tissues and masses [56]. . . . .   | 3  |
| 1.2    | (Left) Original reflection image and (right) refraction corrected imaging using SOS [56]. Image boundaries are less distorted and image has overall improved resolution. . . . .   | 4  |
| 1.3    | Schematic diagram of iterative process of inverse problems. The number of iterations required depends on the initial guess of the medium. A reasonable guess is required for convergence lest the algorithm falls into a local minimum. . . . .  | 5  |
| 2.1    | Diagram of hybrid focusing and parameters. A cross-section of the 2D reconfigurable array aperture implementing hybrid annular focusing is shown containing the central axis of the array. . . . .   | 23 |
| 2.2    | To illustrate aperture ring selection, a 128-ring aperture steered 45° is shown. Each ring is linked to a different channel input delay. Ring shape was determined based on quantization of time delays in order to minimize artifacts due to phase error. . . . .   | 28 |
| 2.3    | The axicon beam produced by the outer axicon ring aperture. The axicon central focus is defined as the spatial peak intensity of the beam, which is located in between the intersection with the central axis of the beams normal to the axicon aperture from its inner and outer edges. Changing $r_1$ , $r_2$ , and angle $\phi$ will affect the location of the axicon central focus. . . . . | 30 |
| 2.4    | Minimization function and first energy moment averaged over beam and at focus for $r_1=2$ mm and $r_2=3$ mm aperture over various axicon angles. . . . .   | 31 |
| 2.5    | Minimization function varying axicon fraction A over different total aperture radii, $r_2$ . The best value found for A was approximately 0.25. . . . .  | 32 |
| 2.6    | PSF with 40 dB dynamic range and axial amplitude comparison for closest and farthest aperture. The corresponding central A-line is plotted on each side. The axial amplitude of the hybrid apertures shows that they outperform the spherical at the lower depths for each aperture. . . . .   | 34 |



|      |   |    |
|------|---|----|
| 2.7  | C-scan display on a 40 dB scale of the PSF of a beam steered at 45° using traditional rings (top) and rings with subelements selected by quantization (bottom). The large artifact on the top image due to phase delay error is removed. . . . .  | 35 |
| 2.8  | Surface of minimization function for aperture at deepest focal zone is shown. The chosen aperture falls within the valley signifying at least a local minimum of our cost functional. . . . .   | 38 |
| 2.9  | The A-line plots of the hybrid and spherical apertures are overlaid for the aperture of the first focal zone. At the lower depths, we see that the hybrid aperture is more sensitive when compared to the spherical aperture. . . . .   | 39 |
| 2.10 | Point spread function and spherical void simulation comparison of spherical (left) and hybrid (right) apertures for a composite of the four focal zones over the entire 4.5 cm depth. The depth extremes of each of the four transmit focal zones of the spherical void simulations show higher sensitivity for the hybrid apertures. . . . . | 41 |
| 3.1  | Schematic of inverse problem algorithm is shown. The iteration starts with an initial guess using a homogeneous medium, and ends when the problem has converged when the misfit error satisfies a chosen criterion. . . . .   | 53 |
| 3.2  | Experimental setup with two ATL L7-4 linear arrays. The distance between both transducers is approximately 5 cm apart, which is the average thickness of a compressed breast. A worm rubber contrast is placed in the center and the tank is filled with water for experimental data collection. . . . .                                      | 58 |
| 3.3  | Reconstructed image with regularization based on <i>a priori</i> information on data and model space. There are some striations noted in the image resulting from undersampling with respect to the reconstructed grid. The reconstructed SOS value reached approximately 1470 m/s. . . . .   | 62 |
| 3.4  | Reconstructed image from simulation includes regularization via correlation between assumed homogeneous pixels. The reconstructed image of cylinder reaches approximately 1440 m/s. . . . .   | 63 |
| 3.5  | Images reconstructed from simulation with correlated homogeneous region with different correlation coefficient values. As the value increases, the reconstruction improves and limited aperture smearing artifact is diminished. . . . .  | 64 |
| 3.6  | Cross-section through the simulated object when using different correlation coefficients. The speed of sound value obtained in the object monotonically approaches the correct value as we increase the value of the correlation coefficient in the values of Fig. 3.5 (0.00001 - Blue, 0.0001 - Magenta, 0.001 Black, 0.01 - Red). . . . .   | 65 |
| 3.7  | Two simulated 6 mm diameter cylinders placed close to each other to demonstrate the PSF overlap. The speed of sound dips only to 1470 m/s and the cylinders can barely be distinguished from each other. . . . .  | 66 |

|      |  |    |
|------|--|----|
| 3.8  | Reconstructed image of the same data as Fig. 3.7 but with pixels correlated together as assumed homogeneous regions. The two cylinders can now be differentiated from each other, and the reconstructed value reaches approximately 1440 m/s. . . . .  | 67 |
| 3.9  | Experimental data was taken with 128 transmitters and 128 receivers placed in an opposed array geometry with a cylinder of 1406 m/s placed in the center. The contrast is recovered, and the diamond shaped point spread function is noticeable. Similar to simulation, the value within the contrasting cylinder dips to approximately 1440 m/s due to the smearing artifact. . . . .   | 70 |
| 3.10 | A thick ray implementation of the path length matrix is demonstrated. The speed of sound image is smoother when compared to the pencil ray implementation. The value within the contrasting cylinder is similar, but the microvariations throughout the image are largely decreased. . . . .   | 71 |
| 3.11 | The homogeneous region was correlated together to aid the inversion. The reconstructed speed of sound value reached approximately 1400 m/s, which is more accurate than the inversion without regularization via correlated pixels. . . . .  | 72 |
| 4.1  | RF data recorded when transmitting with the 64 <sup>th</sup> element on one array. The experimental and simulated shots are very similar to each other. The most important data to extract from the model are the bands outside the center portion (corresponding to the beam traveling by the edge of the cylinder) as the recorded energy is very small and greatly distort attenuation image reconstructions. . . . .   | 86 |
| 4.2  | Raw signal energy data is shown, uncorrected. The large bands of low energy for the object data illustrate the diffraction and multipath phase cancellation of the wave at the edge of the low SOS cylinder. . . . .   | 88 |
| 4.3  | The energy ratio across the receivers when transmitting with the 64 <sup>th</sup> element is shown. The dips in energy shown in experimental data (green) align closely with those found from simulation (blue). . . . .   | 89 |
| 4.4  | The corrected attenuation data (lower image) to be fed into the reconstruction algorithm is illustrated. The low energy bands corresponding to the edge of the cylinder are removed, while the beams that traverse the center of the cylinder indicate a much higher attenuation than the uncorrected data. . . . .  | 90 |
| 4.5  | The resulting attenuation image using a weighted least squares model with <i>a priori</i> information is depicted for the uncorrected (top image) and corrected dataset (bottom). The cylinder is recovered with a high relative attenuation compared to the background of water when the dataset is corrected. When uncorrected, the resulting image shows only a strong silhouette of the contrasting cylinder with faint attenuation within the cylinder. . . . . | 91 |

# LIST OF TABLES

Table

|     |  |    |
|-----|--|----|
| 2.1 | Beamwidth difference ( $w(z)-w(22)$ ) at different focusing depths. . .  | 29 |
| 2.2 | Chosen parameters for each locally optimized aperture. All parameters are in mm except for $\phi$ , which is in degrees. . . . . | 32 |
| 2.3 | LSNR calculations for spherical and hybrid apertures along with p-values for statistical difference. . . . .                     | 33 |

## CHAPTER I

# Breast Cancer Imaging

### 1.1 Background and Significance

Breast cancer is one of the most predominant forms of cancer, comprising 22.9% of all cancers in women, causing approximately 450,000 deaths in 2008 [1]. However, survival rates can be greatly improved with early detection of a growing tumor, which lends importance to annual breast cancer screening and diagnosis for women above the age of 30, especially if there is a history of breast cancer in the family.

Current breast diagnostic imaging encompasses conventional mammography followed by handheld ultrasound along with use of radionuclid and MR imaging in special cases. While mammography is the standard for breast cancer screening and initial diagnosis, ultrasound is nearly always performed on suspicious lesions to reduce negative biopsies or to provide additional information when mammogram results are ambiguous [2–8] because sensitivity of mammography decreases when imaging dense breast tissue, which is prevalent among young women. Ultrasound is also used throughout the developed world outside the USA, and very modestly here for an increase in sensitivity in screening. Improving ultrasound image quality and variety of imaged tissue properties should prove beneficial to breast cancer screening and diagnosis.

Although handheld ultrasound is usually performed in addition to mammography on suspicious lesions for extra diagnostic information, the focused lesion is sometimes

different from the lesion found in the mammogram when there are several lesions in the breast. Obtaining a full 3D volume ultrasound image of the breast would eliminate this problem and inconsistencies in diagnosis due to operator error. Enabling efficient 3D scanning also removes the need for a physician or skilled technician to be present at the scan, thereby reducing overall cost of the scan itself. However, there are certain limitations to current 3D automated ultrasound scanning including the length of time it takes for each acquisition and robust positioning of translated 1D transducer arrays to minimize image artifacts due to mechanical backlash between different image slices. Currently, clinical 3D automated scans of the compressed breast using an M12L linear array on the GE Logiq 9 [9, 10] take approximately 2.5 minutes to acquire one 20 cm sweep, with average breasts requiring 2-3 sweeps.

Recent studies have also shown that diagnostic value increases when multiple modalities are used for diagnosis. Breast imaging, magnetic resonance imaging [7, 11–16] and tomosynthesis [17–21] have been shown to provide additional information for mass localization and characterization along with other modes of ultrasound such as Doppler colorflow imaging [22–34], optoacoustics [35–41], and elastography [42–49]. Using alternative ultrasound modes over other modalities is advantageous as it increases valuable diagnostic information with little expense in data acquisition time since ultrasound data is already collected with regular patient screening.

Another mode of acoustic imaging is transmission imaging. Transmission imaging encompasses speed of sound (SOS) wave imaging and the attenuation of those waves. Transmission imaging of the breast has been actively studied for enhanced tumor detection and characterization [50–55]. With breast imaging, SOS images provide vital information due to the inherent inhomogeneities present in lesions with fatty and glandular tissue. SOS imaging is advantageous when imaging the breast

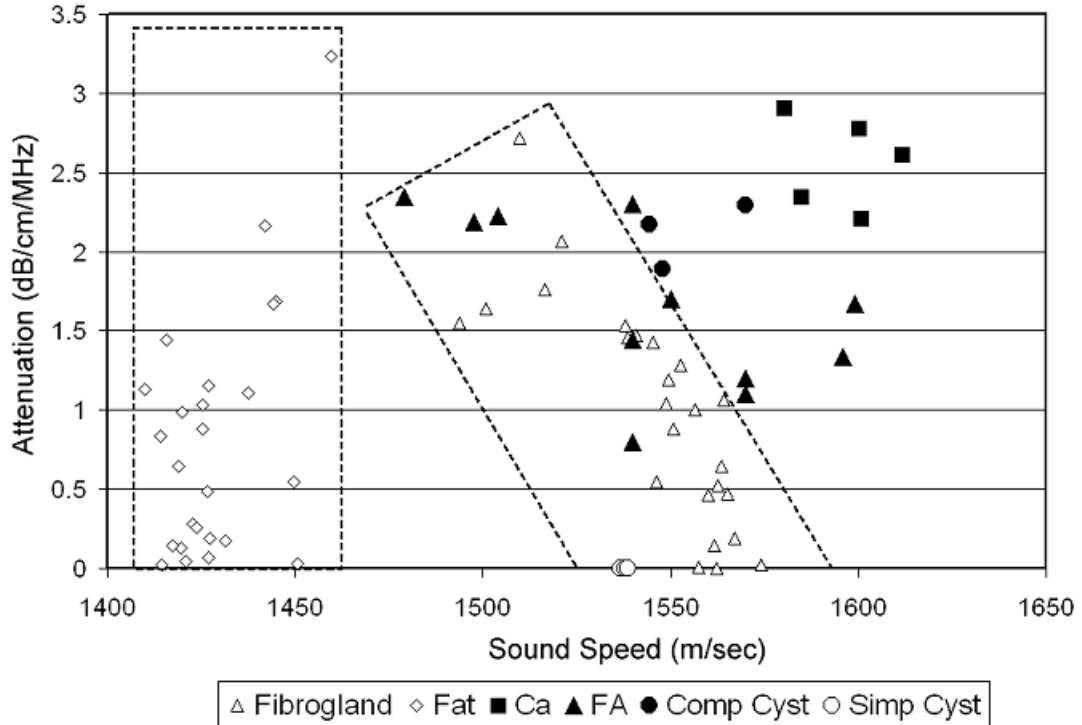


Figure 1.1: Acoustic properties of normal tissues and masses [56].

because there is a lack of specular reflectors for conventional reflection imaging [52]. Malignant lesions also have been associated with a higher speed of sound compared to surrounding tissue [50–52]. While conventional ultrasound B-mode imaging assumes a uniform speed of sound in the breast, leading to distortions in the reconstructed image, grayscale image reconstruction methods can take the variable sound speed obtained from SOS imaging into account to provide a more resolved image (Fig. 1.2).

SOS and attenuation imaging of the breast have been performed in various setup geometries such as circular [50–53, 57] and toroidal [58]. Preliminary studies investigating amplitude and velocity reconstruction in the compressed geometry have been shown to detect and differentiate lesions in a clinical setting as well [59, 60]. However, there are added complications when imaging in the compressed geometry because there are limited angles at which data is acquired, usually leading to a

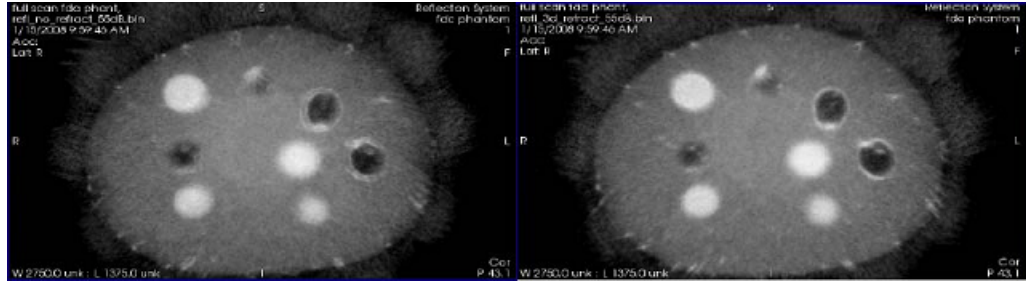


Figure 1.2: (Left) Original reflection image and (right) refraction corrected imaging using SOS [56]. Image boundaries are less distorted and image has overall improved resolution.

streaking artifact in the axial plane similar to tomosynthesis.

SOS and attenuation images can also be obtained by solving the inverse acoustic wave problem. This area of study has been of interest in multiple fields such as seismology [61–64] and electromagnetic imaging [65, 66]. The inverse problem is defined when the input and output is known and the goal is to define the unknown medium. A first guess at the imaged object is required, usually set to a homogeneous medium. Using a forward model of the current guess, an update is obtained. The current guess is then updated, and the process is repeated until the update is shown to be small, indicating that the problem has converged. A primary limitation to image reconstruction using the full wave acoustic problem is the computation power and memory needed to compute the forward model, as this step is performed for each iteration, leading to lengthy reconstruction times. Also, it is necessary that the computed forward model is accurate enough to ensure convergence, requiring precise characterization of the transmitting and receiving transducers.

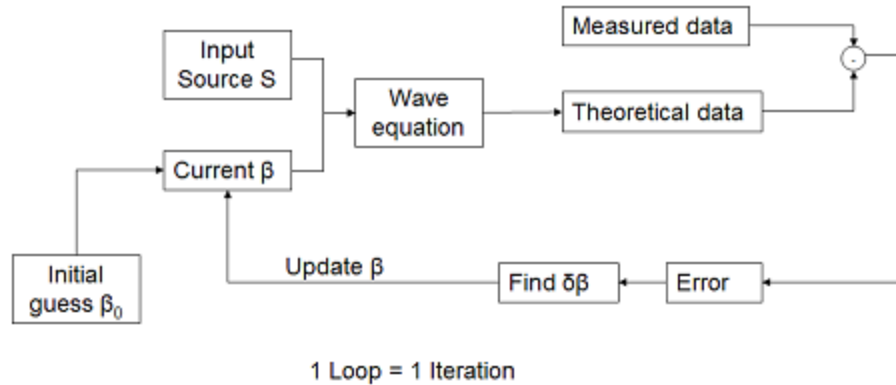


Figure 1.3: Schematic diagram of iterative process of inverse problems. The number of iterations required depends on the initial guess of the medium. A reasonable guess is required for convergence lest the algorithm falls into a local minimum.

## 1.2 Specific Aims

This dissertation focuses on developing beamforming techniques to improve grayscale B-mode imaging and proposes viable speed of sound and attenuation imaging reconstructions for the compressed breast. This geometry is advantageous because it aligns with the mammographic geometry, enabling a more convenient registration of tissue structure to the gold standard screening procedure, while also allowing for automated 3D ultrasound scanning.

Beamforming techniques will be applied in the context of reconfigurable arrays, a recent advancement in ultrasound technology, and will be described in chapter 2. Reconfigurable arrays are comprised of many small capacitive micromachined ultrasound technology (CMUT) subelements dynamically linked together to form larger elements. Ultrasound reconfigurable arrays are advantageous as they are large, 2D, and amenable to annular array configurations. Given enough elements, annular arrays provide beamforming quite superior to traditional linear arrays because their elevational beam width is equivalent to their lateral performance [67]. The number of channels or elements required for a high quality image is much less compared to



linear arrays [68]. While conventional 2D arrays can achieve the same results or better, annular arrays only require a limited number of channels as their symmetry takes advantage of the redundancy in phase delays across elements of the aperture.

Since the reconfigurable arrays are large and 2D, the arrays themselves can be used to compress the breast and minimize difficult gel coupling issues between breast tissue and the transducer. Furthermore, instead of translating 1D linear arrays across the breast, the transmitting and receiving aperture can be electronically moved across the array instead to eliminate artifacts in the 3D volume dataset stemming from mechanical backlash induced by mechanical translators. A beamforming algorithm to develop a transmit beam with extended depth of focus is investigated to ultimately increase framerate of acquisitions, which is advantageous in a 3D data acquisition setting especially when applying it to ultrasound modes such as Doppler with currently low framerates. An improved framerate also leads to lower overall data acquisition time, and consequently reduced time for the patient spent in compression. Steering the beam may sometimes be essential for more complete coverage of the breast due to the nature of the compressed geometry. Thus, optimized beam steering for the reconfigurable array is also investigated to reduce extra side lobe energy present in current focusing techniques.

Since extra diagnostic information for breast cancer screening can be garnered through other modalities, adding additional ultrasound-based modalities for the compressed breast will be investigated in chapters 3 and 4. A method for developing speed of sound and attenuation images in, but not limited to, the compressed breast geometry will be described. The technique involves solving a regularized inverse problem using the eikonal wave equation. The eikonal wave equation is a ray optics simplification of the full wave acoustic equation, and is much faster to compute in comparison to the full wave equation. Because we are working in the compressed breast geometry, data can only be acquired with limited angles compared to a full

computed tomography (CT) geometry. The streaking artifacts that are prominent in acquisitions in such a geometry will be addressed by incorporating *a priori* information to the inversion, and the reconstruction method will be first tested in simulation and then applied to a worm rubber phantom with known speed of sound and attenuation properties.

## BIBLIOGRAPHY

- [1] “World Cancer Report,” *International Agency for Research on Cancer*, 2008.
- [2] D. Rotten and J. M. Levailant, “The value of ultrasonic examination to detect and diagnose breast carcinomas. Analysis of the results obtained in 125 tumors using radiographic and ultrasound mammography.,” *Ultrasound in obstetrics & gynecology : the official journal of the International Society of Ultrasound in Obstetrics and Gynecology*, vol. 2, pp. 203–214, May 1992.
- [3] D. Rotten, J. M. Levailant, and L. Zerat, “Analysis of normal breast tissue and of solid breast masses using three-dimensional ultrasound mammography.,” *Ultrasound in obstetrics & gynecology : the official journal of the International Society of Ultrasound in Obstetrics and Gynecology*, vol. 14, pp. 114–124, Aug. 1999.
- [4] Y. Zheng, J. F. Greenleaf, and J. J. Gisvold, “Reduction of breast biopsies with a modified self-organizing map,” *Neural Networks, IEEE Transactions on*, vol. 8, pp. 1386–1396, Nov. 1997.
- [5] W. A. Berg, J. D. Blume, J. B. Cormack, E. B. Mendelson, D. Lehrer, M. Böhm-Vélez, E. D. Pisano, R. A. Jong, W. P. Evans, M. J. Morton, M. C. Mahoney, L. H. Larsen, R. G. Barr, D. M. Farria, H. S. Marques, and K. Boparai, “Combined Screening With Ultrasound and Mammography vs Mammography Alone in Women at Elevated Risk of Breast Cancer,” *JAMA*:

- The Journal of the American Medical Association*, vol. 299, pp. 2151–2163, May 2008.
- [6] E. Deurloo, “Reduction in the number of sentinel lymph node procedures by preoperative ultrasonography of the axilla in breast cancer,” *European Journal of Cancer*, vol. 39, pp. 1068–1073, May 2003.
- [7] C. K. Kuhl, S. Schrading, C. C. Leutner, N. Morakkabati-Spitz, E. Wardelmann, R. Fimmers, W. Kuhn, and H. H. Schild, “Mammography, breast ultrasound, and magnetic resonance imaging for surveillance of women at high familial risk for breast cancer.,” *Journal of clinical oncology*, vol. 23, pp. 8469–8476, Nov. 2005.
- [8] H. M. Zonderland, E. G. Coerkamp, J. Hermans, M. J. van de Vijver, and A. E. van Voorthuisen, “Diagnosis of Breast Cancer: Contribution of US as an Adjunct to Mammography1,” *Radiology*, vol. 213, pp. 413–422, Nov. 1999.
- [9] S. P. Sinha, M. A. Roubidoux, M. A. Helvie, A. V. Nees, M. M. Goodsitt, G. L. LeCarpentier, J. B. Fowlkes, C. L. Chalek, and P. L. Carson, “Multi-modality 3D breast imaging with X-Ray tomosynthesis and automated ultrasound,” in *Engineering in Medicine and Biology Society, 2007. EMBS 2007. 29th Annual International Conference of the IEEE*, pp. 1335–1338, IEEE, Aug. 2007.
- [10] S. P. Sinha, M. M. Goodsitt, M. A. Roubidoux, R. C. Booi, G. L. LeCarpentier, C. R. Lashbrook, K. E. Thomenius, C. L. Chalek, and P. L. Carson, “Automated Ultrasound Scanning on a Dual-Modality Breast Imaging System,” *Journal of Ultrasound in Medicine*, vol. 26, pp. 645–655, May 2007.
- [11] M. Kriege, C. T. M. Brekelmans, C. Boetes, P. E. Besnard, H. M. Zonderland, I. M. Obdeijn, R. A. Manoliu, T. Kok, H. Peterse, M. M. A. Tilanus-Linthorst, S. H. Muller, S. Meijer, J. C. Oosterwijk, L. V. A. M. Beex, R. A. E. M.

- Tollenaar, H. J. de Koning, E. J. T. Rutgers, and J. G. M. Klijn, "Efficacy of MRI and Mammography for Breast-Cancer Screening in Women with a Familial or Genetic Predisposition," *N Engl J Med*, vol. 351, pp. 427–437, July 2004.
- [12] S. G. Orel, M. D. Schnall, C. M. Powell, M. G. Hochman, L. J. Solin, B. L. Fowble, M. H. Torosian, and E. F. Rosato, "Staging of suspected breast cancer: effect of MR imaging and MR-guided biopsy," *Radiology*, vol. 196, pp. 115–122, July 1995.
- [13] M. O. Leach, C. R. Boggis, A. K. Dixon, D. F. Easton, R. A. Eeles, D. G. Evans, F. J. Gilbert, I. Griebisch, R. J. Hoff, P. Kessar, S. R. Lakhani, S. M. Moss, A. Nerurkar, A. R. Padhani, L. J. Pointon, D. Thompson, R. M. Warren, and MARIBS study group, "Screening with magnetic resonance imaging and mammography of a UK population at high familial risk of breast cancer: a prospective multicentre cohort study (MARIBS).," *Lancet*, vol. 365, no. 9473, pp. 1769–1778, 2005.
- [14] M. M. A. Tilanus-Linthorst, I. M. Obdeijn, K. C. M. Bartels, H. J. de Koning, M. Oudkerk, M. M. A. Tilanus-Linthorst, I. M. Obdeijn, K. C. M. Bartels, H. J. de Koning, and M. Oudkerk, "First experiences in screening women at high risk for breast cancer with MR imaging," *Breast Cancer Research and Treatment*, vol. 63, pp. 53–60, Sept. 2000.
- [15] S. J. Lord, W. Lei, P. Craft, J. N. Cawson, I. Morris, S. Walleser, A. Griffiths, S. Parker, and N. Houssami, "A systematic review of the effectiveness of magnetic resonance imaging (MRI) as an addition to mammography and ultrasound in screening young women at high risk of breast cancer," *European Journal of Cancer*, vol. 43, pp. 1905–1917, Sept. 2007.
- [16] E. Warner, D. B. Plewes, R. S. Shumak, G. C. Catzavelos, L. S. Di Prospero, M. J. Yaffe, V. Goel, E. Ramsay, P. L. Chart, D. E. Cole, G. A. Taylor,

- M. Cutrara, T. H. Samuels, J. P. Murphy, J. M. Murphy, and S. A. Narod, "Comparison of breast magnetic resonance imaging, mammography, and ultrasound for surveillance of women at high risk for hereditary breast cancer.," *Journal of clinical oncology*, vol. 19, pp. 3524–3531, Aug. 2001.
- [17] L. T. Niklason, B. T. Christian, L. E. Niklason, D. B. Kopans, D. E. Castleberry, B. H. Opsahl-Ong, C. E. Landberg, P. J. Slanetz, A. A. Giardino, R. Moore, D. Albagli, M. C. DeJule, P. F. Fitzgerald, D. F. Fobare, B. W. Giambattista, R. F. Kwasnick, J. Liu, S. J. Lubowski, G. E. Possin, J. F. Richotte, C. Y. Wei, and R. F. Wirth, "Digital tomosynthesis in breast imaging.," *Radiology*, vol. 205, pp. 399–406, Nov. 1997.
- [18] I. Andersson, D. Ikeda, S. Zackrisson, M. Ruschin, T. Svahn, P. Timberg, A. Tingberg, I. Andersson, D. M. Ikeda, S. Zackrisson, M. Ruschin, T. Svahn, P. Timberg, and A. Tingberg, "Breast tomosynthesis and digital mammography: a comparison of breast cancer visibility and BIRADS classification in a population of cancers with subtle mammographic findings," *European Radiology*, vol. 18, pp. 2817–2825, Dec. 2008.
- [19] S. P. Poplack, T. D. Tosteson, C. A. Kogel, and H. M. Nagy, "Digital Breast Tomosynthesis: Initial Experience in 98 Women with Abnormal Digital Screening Mammography," *American Journal of Roentgenology*, vol. 189, pp. 616–623, Sept. 2007.
- [20] D. Gur, G. S. Abrams, D. M. Chough, M. A. Ganott, C. M. Hakim, R. L. Perrin, G. Y. Rathfon, J. H. Sumkin, M. L. Zuley, and A. I. Bandos, "Digital Breast Tomosynthesis: Observer Performance Study," *American Journal of Roentgenology*, vol. 193, pp. 586–591, Aug. 2009.
- [21] X. Gong, S. J. Glick, B. Liu, A. A. Vedula, and S. Thacker, "A computer simulation study comparing lesion detection accuracy with digital mammography,

- breast tomosynthesis, and cone-beam CT breast imaging,” *Medical Physics*, vol. 33, no. 4, pp. 1041–1052, 2006.
- [22] D. D. Adler, P. L. Carson, J. M. Rubin, and D. Quinn-Reid, “Doppler ultrasound color flow imaging in the study of breast cancer: Preliminary findings,” *Ultrasound in Medicine & Biology*, vol. 16, pp. 553–559, Jan. 1990.
- [23] D. O. Cosgrove, J. C. Bamber, J. B. Davey, J. A. McKinna, and H. D. Sinnett, “Color Doppler signals from breast tumors. Work in progress,” *Radiology*, vol. 176, pp. 175–180, July 1990.
- [24] P. Britton and R. Coulden, “The use of duplex Doppler ultrasound in the diagnosis of breast cancer,” *Clinical Radiology*, vol. 42, pp. 399–401, Dec. 1990.
- [25] W. T. Yang, J. Chang, and C. Metreweli, “Patients with Breast Cancer: Differences in Color Doppler Flow and Gray-Scale US Features of Benign and Malignant Axillary Lymph Nodes<sup>1</sup>,” *Radiology*, vol. 215, pp. 568–573, May 2000.
- [26] W.-J. Lee, J.-S. Chu, C.-S. Huang, M.-F. Chang, K.-J. Chang, K.-M. Chen, W.-J. Lee, J.-S. Chu, C.-S. Huang, M.-F. Chang, K.-J. Chang, and K.-M. Chen, “Breast cancer vascularity: Color Doppler sonography and histopathology study,” *Breast Cancer Research and Treatment*, vol. 37, pp. 291–298, Oct. 1996.
- [27] H. Minasian and J. C. Bamber, “A preliminary assessment of an ultrasonic doppler method for the study of blood flow in human breast cancer,” *Ultrasound in Medicine & Biology*, vol. 8, pp. 357–364, Jan. 1982.
- [28] P. Wells, M. Halliwell, R. Skidmore, J. Woodcock, and A. Webb, “Tumour detection by ultrasonic Doppler blood-flow signals,” *Ultrasonics*, vol. 15, pp. 231–232, Sept. 1977.

- [29] G. Esen, B. Gurses, M. H. Yilmaz, S. Ilvan, S. Ulus, V. Celik, M. Farahmand, O. Oz Calay, G. Esen, B. Gurses, M. H. Yilmaz, S. Ilvan, S. Ulus, V. Celik, M. Farahmand, and O. Calay, "Gray scale and power Doppler US in the preoperative evaluation of axillary metastases in breast cancer patients with no palpable lymph nodes," *European Radiology*, vol. 15, pp. 1215–1223, June 2005.
- [30] J. Walsh, J. Dixon, U. Chetty, and D. Paterson, "Colour doppler studies of axillary node metastases in breast carcinoma," *Clinical Radiology*, vol. 49, pp. 189–191, Mar. 1994.
- [31] A. Hollerweger, T. Rettenbacher, P. Macheiner, and N. Gritzmann, "New signs of breast cancer: High resistance flow and variations in resistive indices evaluation by color Doppler sonography," *Ultrasound in Medicine & Biology*, vol. 23, pp. 851–856, Jan. 1997.
- [32] C. Peters-Engl, M. Medl, and S. Leodolter, "The use of colour-coded and spectral Doppler ultrasound in the differentiation of benign and malignant breast lesions.," *British journal of cancer*, vol. 71, pp. 137–139, Jan. 1995.
- [33] H. Madjar, W. Sauerbrei, H. J. Prömpeler, R. Wolfarth, and H. Guffler, "Color Doppler and Duplex Flow Analysis for Classification of Breast Lesions," *Gynecologic Oncology*, vol. 64, pp. 392–403, Mar. 1997.
- [34] W. T. Yang, C. Metreweli, P. K. W. Lam, and J. Chang, "Benign and Malignant Breast Masses and Axillary Nodes: Evaluation with Echo-enhanced Color Power Doppler US1," *Radiology*, vol. 220, pp. 795–802, Sept. 2001.
- [35] A. A. Oraevsky, A. A. Karabutov, S. V. Solomatin, E. V. Savateeva, V. A. Andreev, Z. Gatalica, H. Singh, and R. D. Fleming, "Laser optoacoustic imaging of breast cancer in vivo," in *BiOS 2001: International Biomedical*



- Optics Symposium*, vol. 4256, pp. 6+, The International Society for Optical Engineering., June 2001.
- [36] V. G. Andreev, A. A. Karabutov, S. V. Solomatin, E. V. Savateeva, V. Aleinikov, Y. V. Zhulina, R. D. Fleming, and A. A. Oraevsky, "Optoacoustic tomography of breast cancer with arc-array transducer," in *BiOS 2000: International Biomedical Optics Symposium*, vol. 3916, pp. 36+, The International Society for Optical Engineering., May 2000.
- [37] A. A. Oraevsky, E. V. Savateeva, S. V. Solomatin, A. A. Karabutov, V. G. Andreev, Z. Gatalica, T. Khamapirad, and P. M. Henrichs, "Optoacoustic imaging of blood for visualization and diagnostics of breast cancer," in *BiOS 2002: International Biomedical Optics Symposium*, vol. 4618, pp. 81+, The International Society for Optical Engineering., June 2002.
- [38] S. A. Ermilov, T. Khamapirad, A. Conjusteau, M. H. Leonard, R. Lacewell, K. Mehta, T. Miller, and A. A. Oraevsky, "Laser optoacoustic imaging system for detection of breast cancer," *Journal of Biomedical Optics*, vol. 14, pp. 024007+, Mar. 2009.
- [39] R. O. Esenaliev, A. A. Karabutov, F. K. Tittel, B. D. Fornage, S. L. Thomsen, C. Stelling, and A. A. Oraevsky, "Laser optoacoustic imaging for breast cancer diagnostics: limit of detection and comparison with x-ray and ultrasound imaging," *Proceedings of SPIE*, vol. 2979, pp. 71+, Aug. 1997.
- [40] S. A. Ermilov, A. Conjusteau, K. Mehta, R. Lacewell, P. M. Henrichs, and A. A. Oraevsky, "128-channel laser optoacoustic imaging system (LOIS-128) for breast cancer diagnostics," in *BiOS: Biomedical Optics 2006*, vol. 6086, pp. 608609+, The International Society for Optical Engineering., Feb. 2006.
- [41] M. Pramanik, G. Ku, C. Li, and L. V. Wang, "Design and evaluation of a

- novel breast cancer detection system combining both thermoacoustic (TA) and photoacoustic (PA) tomography,” *Medical Physics*, vol. 35, no. 6, pp. 2218–2223, 2008.
- [42] J. Bercoff, S. Chaffai, M. Tanter, L. Sandrin, S. Catheline, M. Fink, J. L. Gennisson, and M. Meunier, “In vivo breast tumor detection using transient elastography,” *Ultrasound in Medicine & Biology*, vol. 29, pp. 1387–1396, Oct. 2003.
- [43] A. Thomas, S. Kümmel, F. Fritzsche, M. Warm, B. Ebert, B. Hamm, and T. Fischer, “Real-Time Sonoelastography Performed in Addition to B-Mode Ultrasound and Mammography: Improved Differentiation of Breast Lesions?,” *Academic Radiology*, vol. 13, pp. 1496–1504, Dec. 2006.
- [44] H. Zhi, B. Ou, B.-M. Luo, X. Feng, Y.-L. Wen, and H.-Y. Yang, “Comparison of Ultrasound Elastography, Mammography, and Sonography in the Diagnosis of Solid Breast Lesions,” *Journal of Ultrasound in Medicine*, vol. 26, pp. 807–815, June 2007.
- [45] D. Melodelima, J. C. Bamber, F. A. Duck, J. A. Shipley, and L. Xu, “Elastography for breast cancer diagnosis using radiation force: System development and performance evaluation,” *Ultrasound in Medicine & Biology*, vol. 32, pp. 387–396, Mar. 2006.
- [46] K. M. Hiltawsky, M. Krüger, C. Starke, L. Heuser, H. Ermert, and A. Jensen, “Freehand ultrasound elastography of breast lesions: clinical results,” *Ultrasound in Medicine & Biology*, vol. 27, pp. 1461–1469, Nov. 2001.
- [47] M. M. Doyley, J. C. Bamber, F. Fuechsel, and N. L. Bush, “A freehand elastographic imaging approach for clinical breast imaging: system development

- and performance evaluation,” *Ultrasound in Medicine & Biology*, vol. 27, pp. 1347–1357, Oct. 2001.
- [48] Q.-L. Zhu, Y.-X. Jiang, J.-B. Liu, H. Liu, Q. Sun, Q. Dai, and X. Chen, “Real-Time Ultrasound Elastography: Its Potential Role in Assessment of Breast Lesions,” *Ultrasound in Medicine & Biology*, vol. 34, pp. 1232–1238, Aug. 2008.
- [49] C. Pellot-Barakat, M. Sridhar, K. K. Lindfors, and M. F. Insana, “Ultrasonic Elasticity Imaging as a Tool for Breast Cancer Diagnosis and Research,” *Current Medical Imaging Reviews*, vol. 2, pp. 157–164, Feb. 2006.
- [50] P. J. Littrup, N. Duric, S. Azevedo, D. Chambers, J. V. Candy, S. Johnson, G. Auner, J. Rather, E. T. Holsapple, P. J. Littrup, N. Duric, S. Azevedo, D. Chambers, J. V. Candy, S. Johnson, G. Auner, J. Rather, and E. T. Holsapple, “Computerized Ultrasound Risk Evaluation (CURE) System: Development of Combined Transmission and Reflection Ultrasound with New Reconstruction Algorithms for Breast Imaging Acoustical Imaging,” vol. 26 of *Acoustical Imaging*, ch. 23, pp. 175–182, Boston, MA: Springer US, 2002.
- [51] N. Duric, P. J. Littrup, E. Holsapple, A. Babkin, R. Duncan, A. Kalinin, R. Pevzner, and M. Tokarev, “Ultrasound tomography of breast tissue,” in *Medical Imaging 2003*, vol. 5035, pp. 24+, The International Society for Optical Engineering., May 2003.
- [52] N. Duric, P. Littrup, O. Rama, E. Holsapple, N. Duric, P. Littrup, O. Rama, and E. Holsapple, “Computerized Ultrasound Risk Evaluation (CURE): First Clinical Results Acoustical Imaging,” in *Acoustical Imaging* (M. P. André, I. Akiyama, M. Andre, W. Arnold, J. Bamber, V. Burov, N. Chubachi, K. Erikson, H. Ermert, M. Fink, W. S. Gan, B. Granz, J. Greenleaf, J. Hu, J. P. Jones, P. Khuri-Yakub, P. Laugier, H. Lee, S. Lees, V. M. Levin,

- R. Maev, L. Masotti, A. Nowicki, W. O'Brien, M. Prasad, P. Rafter, D. Rouseff, J. Thijssen, B. Tittmann, P. Tortoli, A. Steen, R. Waag, P. Wells, M. P. André, I. Akiyama, M. Andre, W. Arnold, J. Bamber, V. Burov, N. Chubachi, K. Erikson, H. Ermert, M. Fink, W. S. Gan, B. Granz, J. Greenleaf, J. Hu, J. P. Jones, P. Khuri-Yakub, P. Laugier, H. Lee, S. Lees, V. M. Levin, R. Maev, L. Masotti, A. Nowicki, W. O'Brien, M. Prasad, P. Rafter, D. Rouseff, J. Thijssen, B. Tittmann, P. Tortoli, A. Steen, R. Waag, and P. Wells, eds.), vol. 28 of *Acoustical Imaging*, ch. 19, pp. 173–181, Dordrecht: Springer Netherlands, 2007.
- [53] P. L. Carson, C. R. Meyer, A. L. Scherzinger, and T. V. Oughton, “Breast imaging in coronal planes with simultaneous pulse echo and transmission ultrasound,” *Science*, vol. 214, pp. 1141–1143, Dec. 1981.
- [54] H. Gemmeke and N. Ruiter, “3D ultrasound computer tomography for medical imaging,” *Nuclear Instruments and Methods in Physics Research Section A: Accelerators, Spectrometers, Detectors and Associated Equipment*, vol. 580, pp. 1057–1065, Oct. 2007.
- [55] J. S. Schreiman, J. J. Gisvold, J. F. Greenleaf, and R. C. Bahn, “Ultrasound transmission computed tomography of the breast,” *Radiology*, vol. 150, pp. 523–530, Feb. 1984.
- [56] M. P. André, C. H. Barker, N. Sekhon, J. Wiskin, D. Borup, and K. Callahan, “Pre-Clinical Experience with Full-Wave Inverse-Scattering for Breast Imaging Acoustical Imaging,” vol. 29 of *Acoustical Imaging*, ch. 10, pp. 73–80, Dordrecht: Springer Netherlands, 2009.
- [57] R. Leach, S. G. Azevedo, J. G. Berryman, H. Bertete-Aguirre, D. H. Chambers, J. E. Mast, P. J. Littrup, N. Duric, S. A. Johnson, and F. Wuebbeling, “Comparison of ultrasound tomography methods in circular geometry,” in

- Medical Imaging 2002*, vol. 4687, pp. 362+, The International Society for Optical Engineering., Apr. 2002.
- [58] M. P. André, H. S. Janée, P. J. Martin, G. P. Otto, B. A. Spivey, and D. A. Palmer, “High-speed data acquisition in a diffraction tomography system employing large-scale toroidal arrays,” *Int. J. Imaging Syst. Technol.*, vol. 8, no. 1, pp. 137–147, 1997.
- [59] K. Richter, “Clinical amplitude/velocity reconstructive imaging (CARD) – a new sonographic method for detecting breast lesions,” *Br J Radiol*, vol. 68, pp. 375–384, Apr. 1995.
- [60] K. Richter, H. Prihoda, S. H. Heywang-Köbrunner, and B. Hamm, “Description and first clinical use of a new system for combined mammography and automated clinical amplitude/velocity reconstructive imaging breast sonography,” *Investigative radiology*, vol. 32, pp. 19–28, Jan. 1997.
- [61] C. Bunks, F. M. Saleck, S. Zaleski, and G. Chavent, “Multiscale seismic waveform inversion,” *Geophysics*, vol. 60, pp. 1457–1473, Oct. 1995.
- [62] A. Tarantola, “Inversion of seismic reflection data in the acoustic approximation,” *Geophysics*, vol. 49, no. 8, pp. 1259–1266, 1984.
- [63] V. Cerveny and M. G. Brown, “Seismic Ray Theory,” vol. 113, pp. 14+, Jan. 2003.
- [64] J. Um and C. Thurber, “A fast algorithm for two-point seismic ray tracing,” *Bulletin of the Seismological Society of America*, vol. 77, pp. 972–986, June 1987.
- [65] N. Joachimowicz, C. Pichot, and J. P. Hugonin, “Inverse scattering: an iterative numerical method for electromagnetic imaging,” *Antennas and Propagation, IEEE Transactions on*, vol. 39, pp. 1742–1753, Dec. 1991.

- [66] Y. M. Wang and W. C. Chew, “An iterative solution of the two-dimensional electromagnetic inverse scattering problem,” *Int. J. Imaging Syst. Technol.*, vol. 1, no. 1, pp. 100–108, 1989.
- [67] M. Arditi, “Transient fields of concave annular arrays,” *Ultrasonic Imaging*, vol. 3, pp. 37–61, Jan. 1981.
- [68] F. S. Foster, J. D. Larson, M. K. Mason, T. S. Shoup, G. Nelson, and H. Yoshida, “Development of a 12 element annular array transducer for realtime ultrasound imaging,” *Ultrasound in Medicine & Biology*, vol. 15, pp. 649–659, Jan. 1989.

## CHAPTER II

# Optimized Beamforming with 2D Reconfigurable Arrays

## 2.1 Benefits of Annular Arrays

Annular array focusing is a viable alternative to linear and cylindrical focusing as it provides a large improvement in elevational beam width in comparison to conventional linear arrays without requiring a large number of channels [1]. Early studies showed that annular arrays with as few as 12 rings produce good quality images [2].

Reconfigurable arrays are especially advantageous with annular and other configurations because subelements are dynamically linked together to form larger elements and can be adjusted to optimize the beam for steering and partial aperture imaging at the edges of the scanning area [3–5]. Activation of subelements is electronically moved across the aperture for precise and accurate beamforming. Not only are fewer channels needed, but this technology eliminates mechanical error and failures and electronic motor noise which are prevalent when translating linear arrays for a 3D volume dataset, thereby avoiding unnecessary degradation in image spatial fidelity and signal to noise ratio [6].

The reconfigurable array concept allows us to take advantage of linear and other symmetrical beamforming as well. For instance, axicon focusing can be easily implemented with this array technology. Axicon focusing has been investigated

in optics [7, 8] along with various acoustical studies [9–12]. Axicon focusing is advantageous as the beams maintain a constant width of the main lobe over the length of the beam, allowing for a large depth of focus. However, there is considerable sidelobe energy beyond the main axis that has prevented practical use of axicon focusing in pulse echo imaging. An alternative to long depth of focus encompasses variations of the non-diffracting solution to the wave equation [13, 14]. These non-diffracting beams also propagate with a constant beam width over a long distance. Nevertheless, they consist of energy off-axis that requires suppression for high resolution and high contrast imaging. Other variations such as a Lorentz resonance curve delay have also been investigated [15].

In this section, we develop methods to improve straight beamforming and beam steering by taking advantage of array reconfigurability for breast imaging. We propose a method of optimizing such an aperture that utilizes spherical and conical focusing to produce a transmit beam with an extended depth of focus while suppressing much of the sidelobe energy usually associated with axicon focusing. A simple hybrid aperture was investigated that takes advantage of the reconfigurability of the 2D aperture as it can be easily achieved in annular configurations. This section will explain aperture choice through beam optimization and compare the optimized beams with purely spherical analogs. We also examine the selection of different elements for steering to improve beam quality.

## **2.2 Constructing Beam with Extended Focus**

### **2.2.1 Transmitted Beam Optimization**

To optimize the beam, we seek to quantify limitations that directly affect ultrasound image quality. Instead of evaluating grayscale ultrasound images, physical limitations that influence image fidelity will be investigated. Performance metrics have been defined and used before to assess quality of ultrasound scanners by evaluating



key characteristics of high quality images such as narrow beam width and deep penetration into soft tissue [16]. In this chapter, we proceed in a similar fashion and introduce slightly more complex cost functions to determine aperture choice that aim to minimize beam width over the entire depth of field while penalizing clutter energy.

We propose a hybrid transmit aperture divided into an inner, spherical portion and an outer, conical, or axicon portion. This focusing elongates the beam, preserving beam width while minimizing side lobe energy that accompanies conical focusing. In order to minimize phase distortion, the delays are matched at the edge between the spherical and conical aperture. We refer to this technique as hybrid beamforming for the rest of the section.

For the proposed hybrid aperture, there are multiple parameters that affect beam quality, including the size of the two apertures, angle of the conical beam ( $\phi$ ) and focusing depth of the spherical beam ( $z_s$ ). The parameters for aperture selection are shown in Fig. 2.1. We label  $r_1$  as the radius at which the spherical and axicon apertures intersect and  $r_2$  as the radius of the entire aperture. Axicon fraction is defined as the ratio of the axicon's to the spherical aperture:

$$A = \frac{r_2 - r_1}{r_1} \quad (2.1)$$

Beams of narrow mainlobe width translate to narrow point spread functions (PSF), or high resolution and sharp borders where they actually are sharp. Beams with low sidelobe and clutter energy result in better contrast-to-noise ratio (CNR) especially when imaging anechoic lesions [17]. Thus, low sidelobe (and clutter energy) contribute to improved detectability of large, low contrast targets [18], as well as improved contrast in what should be extremely high contrast objects such as large, simple cysts. The width at various levels below the peak of the PSF has been chosen to describe the effective beam width for pulse echo imaging. The -6 dB beam

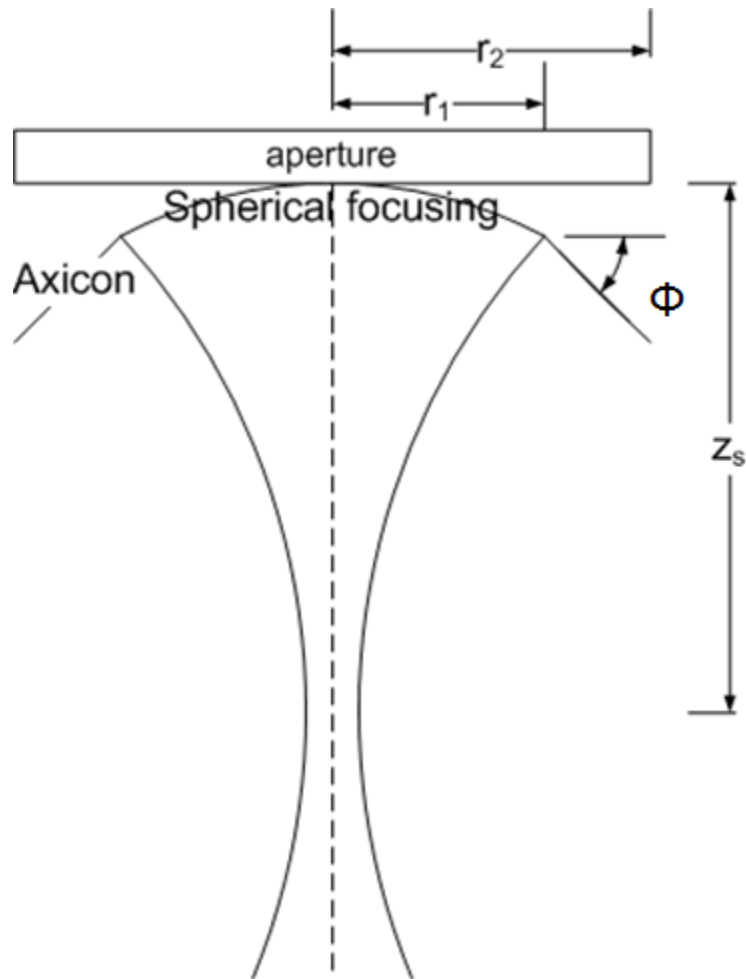


Figure 2.1: Diagram of hybrid focusing and parameters. A cross-section of the 2D reconfigurable array aperture implementing hybrid annular focusing is shown containing the central axis of the array.

width, or full width at half maximum is most common, but the -20 dB width [19] has been recommended by some as more useful in gray scale imaging. There is no one best descriptor of beam width profiles whose shapes can vary, but it is possible to avoid extreme beam shapes. To optimize this hybrid beam over an extended depth range, we implemented an initial closed form cost function that minimizes, for a given transmit pulse, the beam width at two levels over a range of depths:

$$S(w, z) = \frac{\frac{1}{W_6} \int_{z_1}^{z_2} w(6dB)z'dz' + \frac{1}{W_{20}} \int_{z_1}^{z_2} w(20dB)z'dz'}{(z_2 - z_1) \int_{z_1}^{z_2} z'dz'} \quad (2.2)$$

The ultrasound beam widths will be determined as a function of depth via numerical simulation. Given a simulated beam, this cost function integrates the -6 and -20 dB beam  $w$  over the depth range,  $z_1$  to  $z_2$ , where the beam maintains  $>-12$  dB of the peak signal. The integration term includes a  $z$  term to place emphasis on the beam width at deeper depths as sensitivity decreases as a function of depth. Another measure of beam centrality, or the amount of clutter energy in a beam, is the energy ratio, the fraction for the energy in the -6 dB beam width at depth  $z$  as a percent of the total energy passing through a plane at  $z$  and normal to the beam. We place a restriction on the useable range of a given transmission that this energy ratio be maintained at 3% from the average, typically a value around 0.95. In other words, approximately 95% of the energy of the beam at each depth is located within the 6 dB beam width. Depths at which this threshold is not met are removed from the integration range. Since the 6 dB and 20 dB integrations are naturally biased due to the absolute beam width value, they are both normalized by their corresponding spherical Bessel beam width at the spherical focus, as indicated by  $W_6$  and  $W_{20}$ . By minimizing the S metric, we seek the beam with the best combination of narrow beam width over a long depth range ( $z_2 - z_1$ ), which correlates to good lateral resolution over the entire depth of focus.

$S(w,z)$  serves as the core function for minimization of the main lobe of the

hybrid transmit beams, taking into account beam widths and depth of penetration which directly affects the PSF and image resolution. We add another criterion to the minimization factor that will limit energy dispersion of a beam, or the off-axis sidelobe and clutter energy that leads to degradation of image contrast. This metric is especially useful for separability when S values alone fall within a small range of each other. The acoustic power of a beam is centralized if the first moment of intensity is small, so we seek to minimize the ratio of the first to zeroth moment of the intensity at  $z$ :

$$T(r, z) = \mathit{mean} \left( \frac{\int_0^R I(r)r dr}{\int_0^R I(r) dr} \right)_{z_1}^{z_2} \quad (2.3)$$

The moments are calculated and averaged over the depth range of the beam.  $R$  represents the distance from the  $z$ -axis, which in these simulations will correlate to the center of the beam since there is no steering involved. Because we are dealing with symmetric array beamforming,  $r$  may be substituted with  $x$ , or the lateral axis. Smaller  $T$  values correlate to less off-axis energy and higher contrast images, and vice versa. When varying axicon angle, we will add the first moment at the focal depth as it provides a good measure of sidelobe energy.

Using a 7.5 MHz 185  $\mu\text{m}$  pitch array, beams with varying parameters of axicon angle  $\phi$ , spherical aperture radius  $r_1$ , axicon aperture radius  $r_2$ , and spherical focal depth  $z_s$  were simulated with Field II's engine [20]. Axicon angle  $\phi$  was varied from  $12.5^\circ$  to  $20^\circ$  along with aperture outer radius  $r_2$  ranging from 2-10 mm with axicon fractions  $A$  of 0.1-0.5. Spherical focusing depth relative to conical focusing depth was examined as well. With the combined minimization techniques, four optimized apertures were chosen via a semi-automated algorithm to cover a depth of 4.5 cm, coverage typical for breast imaging.

### 2.2.2 Comparison with purely spherical beams

These apertures were compared with purely spherical beams via their PSFs by examining beam width and axial amplitude versus depth. Side lobe energy was also assessed with six instances of 3 mm anechoic spherical void phantoms. Lesion detectability can be quantified with lesion signal-to-noise ratio (LSNR) computed as [21, 22]:

$$LSNR = \frac{|\mu_{lesion} - \mu_{background}|}{\sigma_{background}} \quad (2.4)$$

where  $\mu$  and  $\sigma$  corresponded to the mean and standard deviation, respectively. Each scattering phantom consisted of 10,000 scatterers/cm<sup>3</sup> as the minimum recommended by Oostervald et al for fully developed Rayleigh statistics [23]. To calculate the PSF and LSNR for both spherical and hybrid apertures, we simulated pulse echo imaging with dynamic receive focusing to mirror a practical, clinical setting. Statistical significance was investigated using a two-sided student's t-test.

### 2.2.3 Beam Steering

Beam steering can be achieved with reconfigurable arrays by placing the center of the annuli directly in front of the focus [4]. As steering usually requires finer sampling, delay approximation errors causes detectable artifacts when steering with reconfigurable configurations. To improve steered beam quality, we chose to link subelements together based on their corresponding delay lines instead of subelement location. For instance, if we have 32 channels, we first compute the ideal delay for each subelement and then quantize them to 32 values. Each subelement that shares the same quantized value will be linked to the same channel.

In a reconfigurable array, subelements are connected and disconnected to each other and to system channels via an underlying switch matrix [3]. The groups of subelements that form an element must have an access point to the channel for transmitting and receiving signals. The number of access points in the reconfigurable

array is limited electronically because more switches would be needed for additional access points, which incrementally increases the complexity of the hardware. Our quantization scheme ensures that linked subelements can form a ring without relying on a dense distribution of access points across the array by making sure subelements that share the same delay are mostly contiguous throughout the entire array. For each subelement, a close access point on the order of 5-6 subelements away would be used to minimize propagation delays from access point to subelement.

To test our technique, we simulated one-way transmit beams using two configurations: placing the center of the annular array at the point in front of the focus in the x-y plane, and by dividing the array into elements based on their delay values as illustrated in Fig. 2.2. With 128 channels and a 20 mm 150  $\mu\text{m}$  pitch aperture, the beam was focused 4 cm deep at a central frequency of 5 MHz and steered 45°.

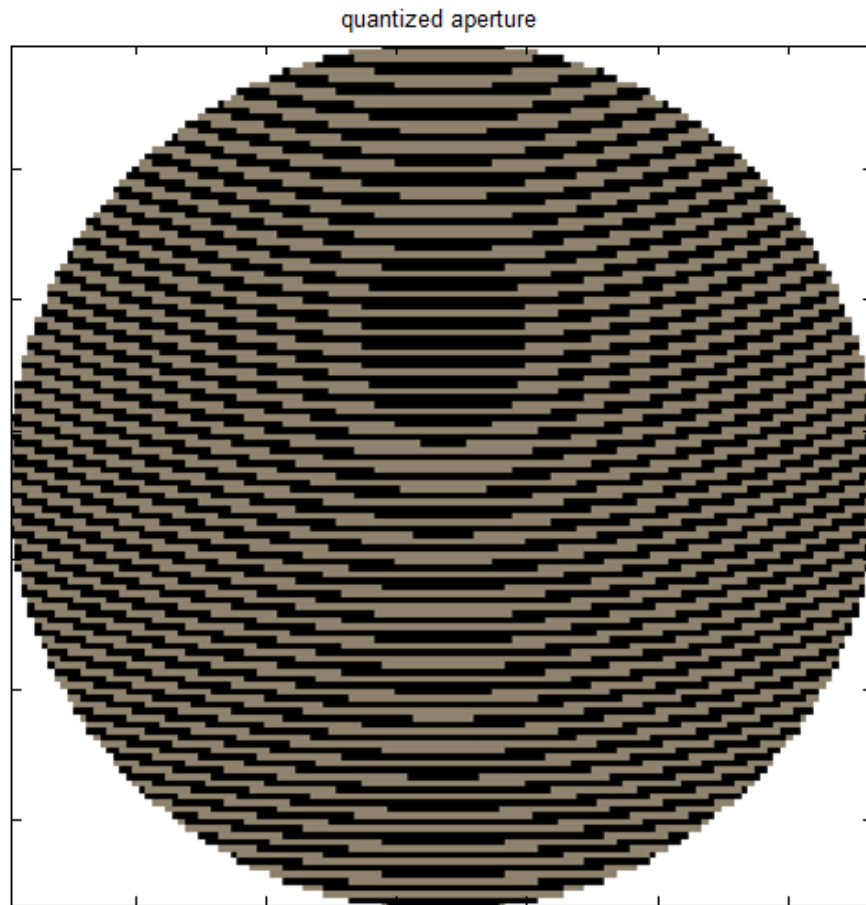


Figure 2.2: To illustrate aperture ring selection, a 128-ring aperture steered  $45^\circ$  is shown. Each ring is linked to a different channel input delay. Ring shape was determined based on quantization of time delays in order to minimize artifacts due to phase error.

## 2.3 Results

### 2.3.1 Beam Optimization

Optimization of aperture size was first performed to determine ideal F-number operation given our array properties. We examined the beam widths found from the PSFs of spherical focusing simulations as a function of aperture diameter. The best aperture at each depth  $z$  corresponds to the smallest beam width difference. The best results were obtained when maintaining an F-number of approximately 1.5 as shown in Table 1. For instance, when focusing at 28 mm, the 18 mm aperture gave the best results. This F-number was used for aperture size in dynamic receive focusing.

Table 2.1: Beamwidth difference ( $w(z)-w(22)$ ) at different focusing depths.

| Focal depth [mm] \ Aperture [mm] | 18     | 20     | 24    | 26    |
|----------------------------------|--------|--------|-------|-------|
| 28                               | -0.192 | -0.150 | 0.149 | 0.151 |
| 30                               | -0.012 | -0.027 | 0.105 | 0.158 |
| 32                               | 0.001  | -0.010 | 0.052 | 0.146 |
| 34                               | 0.023  | 0.003  | 0.030 | 0.127 |
| 36                               | 0.062  | 0.029  | 0.003 | 0.061 |
| 38                               | 0.066  | 0.016  | 0.014 | 0.070 |

For arrays with pitch greater than  $\lambda/2$ , steering angle must be limited to minimize grating lobe effects on image quality. To determine a suitable axicon angle for the hybrid aperture, different  $\phi$ s ranging from  $12.5^\circ$  to  $20^\circ$  were simulated with an aperture using axicon focusing with  $r_1=2$  mm and  $r_2=3$  mm. The spatial peak intensity of the axicon beam depends on the angle chosen and location of the inner and outer edges of the axicon,  $r_1$  and  $r_2$ , which can be determined geometrically as it lies in between the depths at which the beams of the axicon overlap. We will refer to this point of maximum intensity of the axicon beam as the axicon central focus. An illustration showing the location of the axicon central focus with respect to the aperture is shown in Fig. 2.3.

The spherical focusing depth was varied 3-5 mm deeper than the axicon central



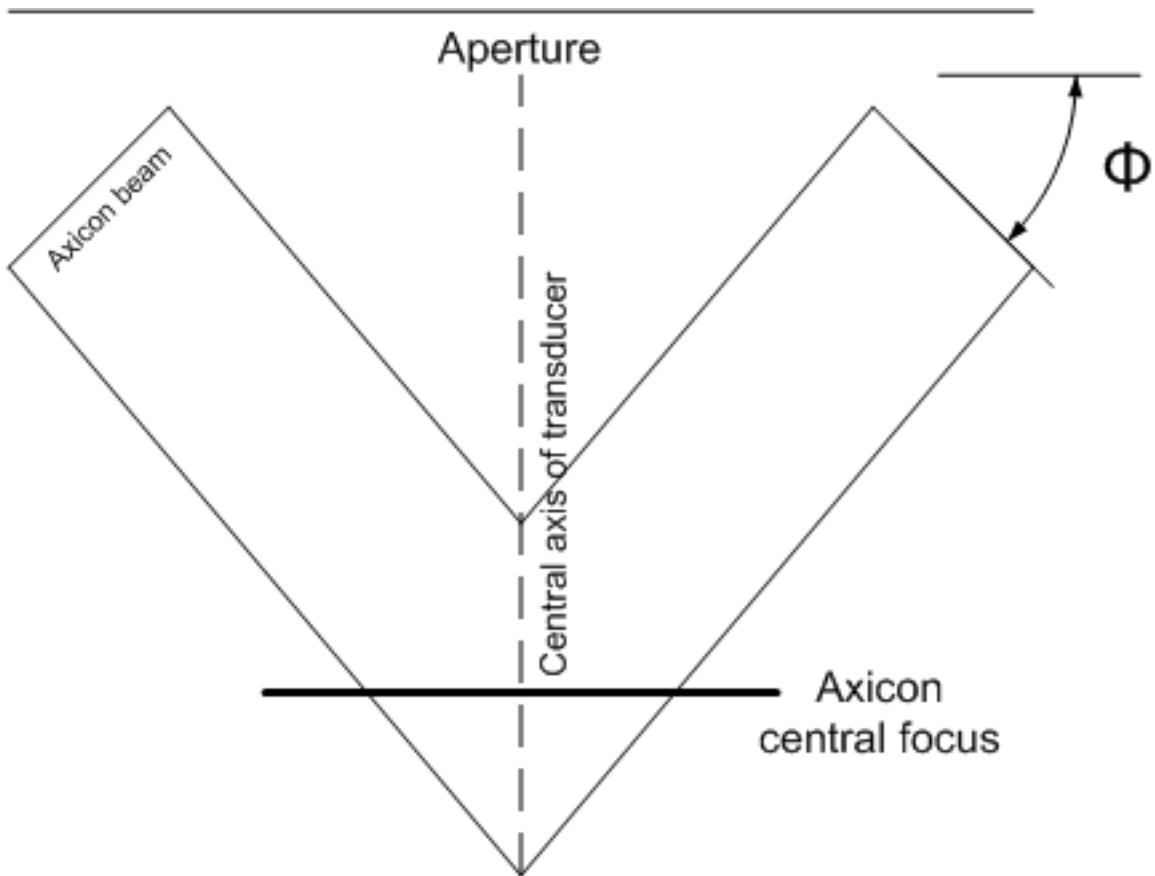


Figure 2.3: The axicon beam produced by the outer axicon ring aperture. The axicon central focus is defined as the spatial peak intensity of the beam, which is located in between the intersection with the central axis of the beams normal to the axicon aperture from its inner and outer edges. Changing  $r_1$ ,  $r_2$ , and angle  $\phi$  will affect the location of the axicon central focus.

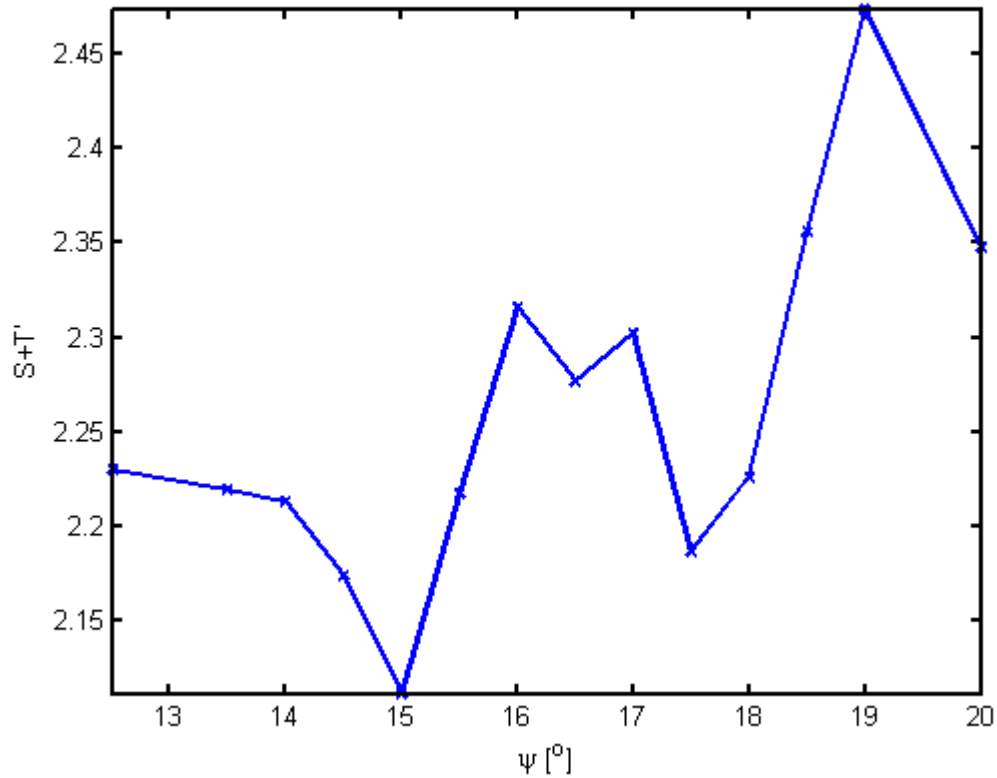


Figure 2.4: Minimization function and first energy moment averaged over beam and at focus for  $r_1=2$  mm and  $r_2=3$  mm aperture over various axicon angles.

focus to improve the uniformity of the beam width and sensitivity with depth. The latter criterion was given more weight at the deepest focal zones where sensitivity is a problem. Focusing the spherical aperture beyond the axicon central focus produces a longer beam along the entire focal zone than would a shorter spherical focal point with a slightly larger beam width. An initial small aperture radius of 3 mm was chosen to not only reduce simulation time but also to minimize the differences between depth range covered due to changing axicon angle.

The ideal axicon angle  $\phi$  was found to be approximately  $15^\circ$  for this beamforming implementation as depicted in Fig. 2.4. To determine optimal axicon fraction  $A$ , we varied aperture size  $r_2$  from 2 to 10 mm with  $A$  ranging from 0.1-0.5 and evaluated our cost functions.

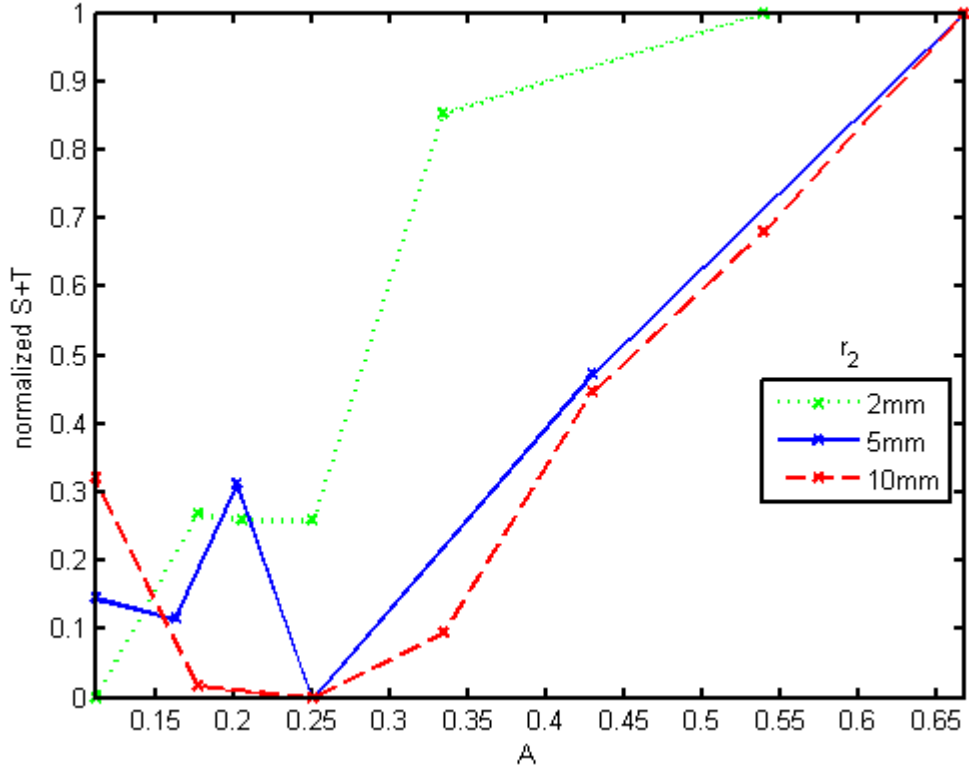


Figure 2.5: Minimization function varying axicon fraction  $A$  over different total aperture radii,  $r_2$ . The best value found for  $A$  was approximately 0.25.

As seen in Fig. 2.5, the optimal axicon fraction  $A$  was found to be approximately 0.25. With a starting axicon angle  $\phi$  of  $15^\circ$  and  $A$  of 0.25, we proceeded to optimize various apertures to cover a depth of 4.5 cm by varying the given parameters  $\phi$  and  $A$  along with spherical focal point  $z_s$ . Four apertures were then chosen to best cover this range. The chosen parameters and focal regions covered by each aperture are delineated in Table 2.2.

Table 2.2: Chosen parameters for each locally optimized aperture. All parameters are in mm except for  $\phi$ , which is in degrees.

| Aperture | Inner axicon edge [ $r_1$ ] | Outer axicon edge [ $r_2$ ] | Axicon angle [ $\phi$ ] | Spherical focal depth [ $z_s$ ] | Starting beam depth [ $z_1$ ] | Ending beam depth [ $z_1$ ] |
|----------|-----------------------------|-----------------------------|-------------------------|---------------------------------|-------------------------------|-----------------------------|
| 1        | 1.5                         | 2                           | 15                      | 10                              | 2                             | 17                          |
| 2        | 4.4                         | 5.5                         | 15                      | 22                              | 15                            | 27                          |
| 3        | 6.5                         | 7.8                         | 15                      | 31                              | 24                            | 37                          |
| 4        | 8                           | 10                          | 14.5                    | 39                              | 31                            | 46                          |

### 2.3.2 Comparison with Purely Spherical Beams

The PSF of each of the four hybrid apertures was computed and compared with purely spherical apertures at corresponding depths. The PSF of the hybrid apertures at the edges of each focal zone showed higher sensitivity and better beam width when compared to the spherical apertures. The PSF and corresponding axial waveforms for the second and fourth aperture are shown in Fig. 2.6. Relative amplitudes are revealed in the waveforms.

LSNR was calculated for comparison using anechoic void phantoms. Six unique iterations were performed at different depths for each aperture, with p-values showing statistical significance at the focal depth extremes. The differences between the hybrid and spherical apertures at the focus were insignificant. Compared to beams using spherical focusing, the hybrid beams produced an elongated, more uniform beam over the range of depths. The average LSNR for spherical and hybrid apertures calculated at specific depths are shown in Table 2.3 along with the p-values.

Table 2.3: LSNR calculations for spherical and hybrid apertures along with p-values for statistical difference.

| Depth [mm] | LSNR <sub>s</sub> [dB] | LSNR <sub>h</sub> [dB] | p-value |
|------------|------------------------|------------------------|---------|
| 13         | 4.61                   | 6.28                   | <0.0001 |
| 19         | 7.25                   | 7.84                   | 0.4126  |
| 25         | 4.10                   | 5.72                   | <0.0001 |
| 28         | 5.71                   | 5.78                   | 0.893   |
| 33         | 4.97                   | 7.52                   | <0.0001 |
| 37         | 8.51                   | 8.31                   | 0.624   |
| 44         | 6.41                   | 7.69                   | <0.0001 |

### 2.3.3 Beam Steering

By minimizing the delay errors for each subelement, we obtained a better quality beam by eliminating the “eagle-wing” artifact found with the previous method using traditional annular rings. The beams shown in Fig. 2.7 are C-scans located in the elevational and lateral plane (radial plane) perpendicular to the steered beam.

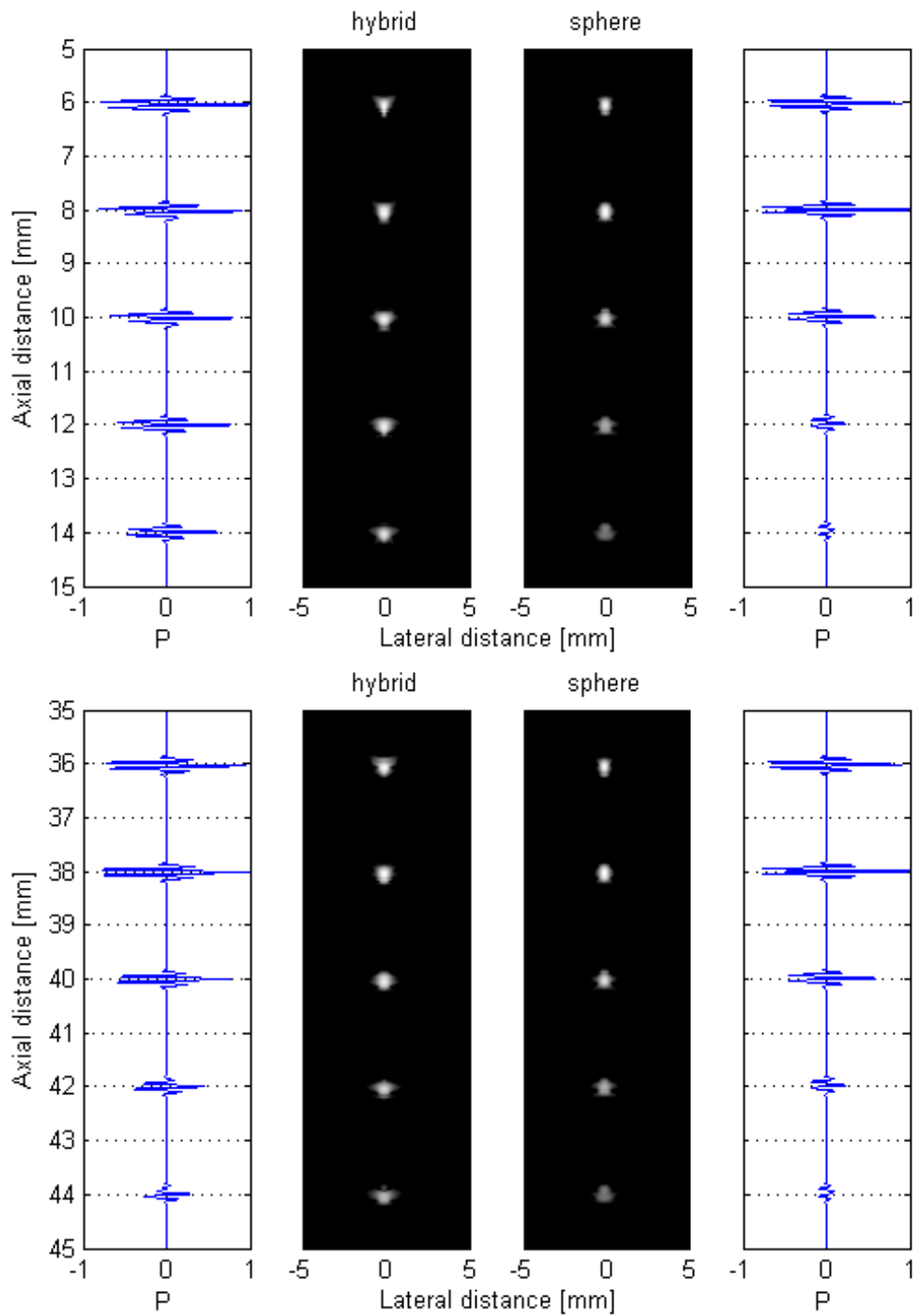


Figure 2.6: PSF with 40 dB dynamic range and axial amplitude comparison for closest and farthest aperture. The corresponding central A-line is plotted on each side. The axial amplitude of the hybrid apertures shows that they outperform the spherical at the lower depths for each aperture.

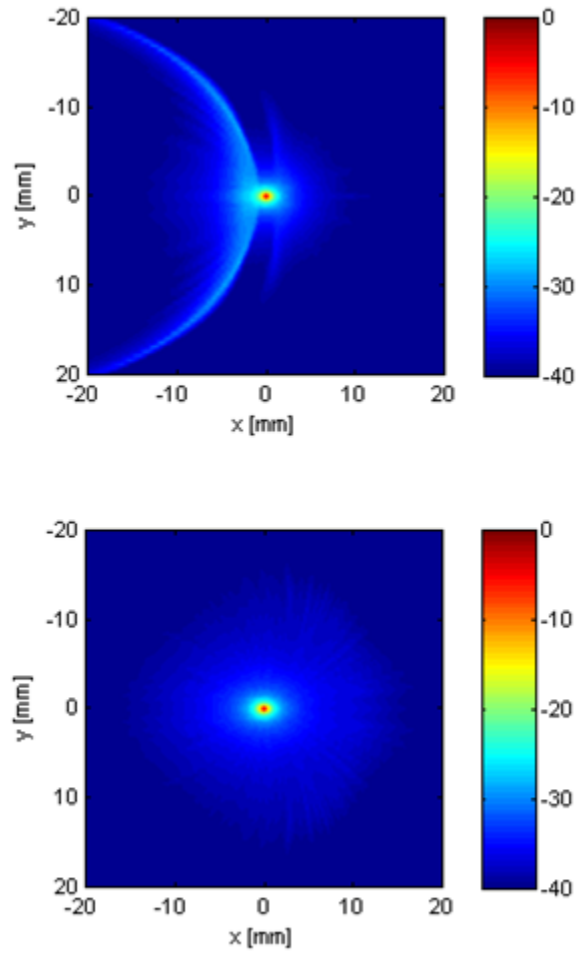


Figure 2.7: C-scan display on a 40 dB scale of the PSF of a beam steered at  $45^\circ$  using traditional rings (top) and rings with subelements selected by quantization (bottom). The large artifact on the top image due to phase delay error is removed.

## 2.4 Discussion

### 2.4.1 Beam Optimization

For practicality, we chose to proceed with the minimization in a sequential manner. This can lead to local minima, requiring additional searches if results are unsatisfactory. The first parameter examined was  $\phi$ , or axicon angle, since this parameter strongly affects how the other parameters should be chosen as well. The angles were varied from  $12.5^\circ$  to  $20^\circ$  in half degree increments. Initial results depicted in Fig. 2.4 showed that beams constructed with  $\phi=15^\circ$  demonstrated a good balance between side lobe energy and depth coverage for deeper foci and was chosen as the initial approximate angle for aperture formation.

If we examine the beams closely, those with  $\phi=20^\circ$  yielded a large amount of side lobe energy while beams with  $\phi=12.5^\circ$  had a much wider beam width, both of which would contribute to an increase in our minimization functions which favors narrower beam width and less side lobe clutter. Although angle sampling was relatively coarse, the tradeoff between side lobe energy and beam width is observed as encountered in traditional conical focusing.

Overall aperture was guided by experience with linear and phased arrays and the observation that, with our subelement geometry, the image quality factors deteriorated for F-numbers less than 1.5, as shown in Table 2.1. We also found that using an aperture larger than 22 mm resulted in worse overall beam width most likely due to excessive phase cancellation effects from focusing coming from the outer edges of the aperture, resulting in destructive interference and an overall decreased focusing effect.

To determine an optimized aperture, aperture size  $r_2$  was varied from 2 to 10 mm and axicon fraction A from 0.1-0.5. Apertures with large A showed too much energy outside the main beam; this also resulted in a discontinuous jagged beam where one could distinguish between the spherical and axicon beam. When A becomes

too small, the beam starts to resemble the purely spherical beam thereby nullifying the hybrid focusing advantage. The optimized axicon portion was found to be approximately 0.25 of its spherical counterpart to produce an optimized, elongated beam for greater depth range. The exception, shown in Fig. 2.5, is at the smallest, 2 mm, aperture. This is most likely attributable to the minute differences obtained in beam width and range for such a small aperture, functioning largely in the near field. As  $A$  increased in value, the range and beam width difference was insufficient to form a function with a minimum.

The final parameter for minimization was  $z_s$ , or spherical focal depth.  $z_s$  was varied 2 to 5 mm beyond the depth of the axicon central focus for optimization. Ideally, we strove to focus as deeply as possible to extend beam range while preserving a narrow, central beam. For all four apertures, the optimal depth choice was found to be approximately 3 mm beyond the axicon central focus. Exceeding this value produced beams with high side lobe energy due to interference between the two different focusing techniques.

Although the choice of apertures to cover our chosen depth relies on these optimized parameters, it is important to note that aperture size also influences depth selection. This occurs because depth coverage of a ringed axicon with axicon angle  $\phi$ -fixed focusing is directly related to axicon fraction  $A$  and aperture size  $r_2$ . Thus, the size of each optimized aperture needs to be chosen accordingly to cover the desired range along with optimized parameters of  $\phi$ ,  $A$ , and spherical focus  $z_s$ . While  $\phi$ ,  $A$ , and  $z_s$  were not optimized for each aperture and depth setting chosen, we did check that the image quality cost functions were at least at local minima over these parameters for each final aperture and focal range. To illustrate, we have included the surface of the cost function for selecting the fourth aperture in Fig. 2.8. We ensured that each chosen aperture was located at the minimum of our functional, providing a good combination of narrow beam width over a long depth



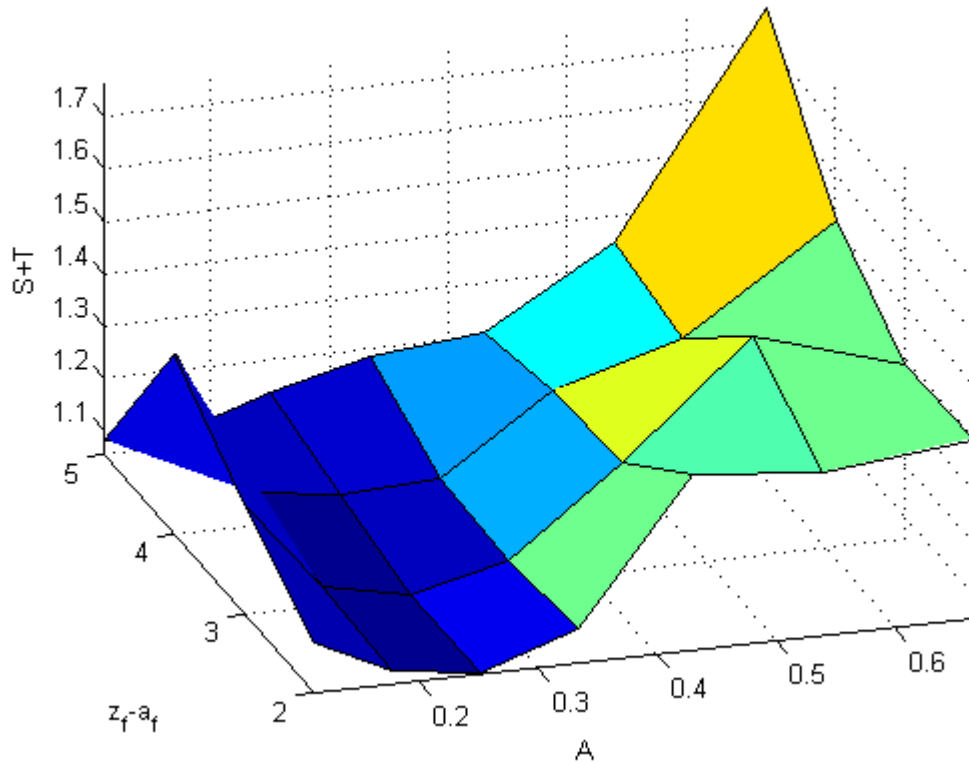


Figure 2.8: Surface of minimization function for aperture at deepest focal zone is shown. The chosen aperture falls within the valley signifying at least a local minimum of our cost functional.

with suppressed clutter energy given the axicon fraction  $A$ , spherical focus  $z_s$ , and axicon central focus parameters.

## 2.4.2 Comparison with Purely Spherical Beams

We compared the hybrid apertures' performance with standard spherically focused beams. The PSFs showed that the purely spherical beams have a narrower beam width at the focus. This is expected, as spherical focusing concentrates most of its energy at the focus. However, the PSF of the hybrid beams sustained better beam width at the focal depth extremes. The hybrid apertures excel at these locations since they direct energy equally in the main lobe at all depths in the focal zone. The hybrid beams covered 1.2 to 1.5 cm within a -12 dB threshold signal while the purely spherical beams averaged 0.8 to 1 cm.

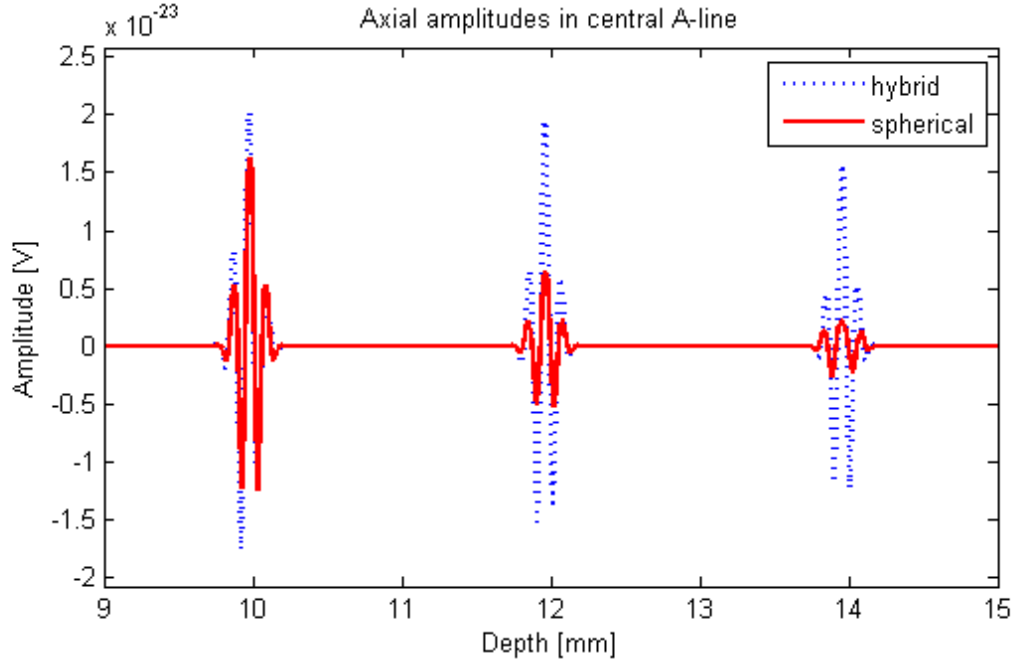


Figure 2.9: The A-line plots of the hybrid and spherical apertures are overlaid for the aperture of the first focal zone. At the lower depths, we see that the hybrid aperture is more sensitive when compared to the spherical aperture.

The central A-line of the PSFs shown in Fig. 6 also demonstrates the increased sensitivity of the hybrid aperture at the deeper extreme of the focal zone. For instance, when comparing the maximum amplitude of the signal at depths of 12 and 14 mm, we observe larger amplitudes when using the hybrid aperture. The axial amplitudes of both the hybrid and spherical apertures for the first focal zone are plotted in Fig. 2.9. At 14 mm, the improvement of the hybrid aperture over the spherical aperture is approximately 8 dB. This improvement in sensitivity is important due to typical signal loss with depth in ultrasound imaging and thus would be beneficial especially in the breast imaging environment.

To assess effects of side lobe and clutter energy, LSNR was calculated with multiple 3 mm spherical void phantoms at different depths encompassing the foci and beyond. We need to note that 10,000 scatterers/cm<sup>3</sup> were used in these phantoms to speed up simulation time. Although the phantoms generated showed well developed speckle, using more scatterers should lead to more consistent values. In our own

experience, some improvement could be seen in going to higher densities but at impractical computation times. Furthermore, simulations were run on six unique scattering phantoms at each depth. Increasing the number of phantoms should also yield better statistics, albeit at the expense of simulation time.

Given the LSNR values in Table 2.3, the purely spherical and hybrid beams both performed well at the focus as slight differences were statistically insignificant. This validates that side lobe and clutter energy usually accompanied with axicon focusing was minimized with this beamforming method. At points beyond the focus, the performance of the hybrid beams was superior to their spherical equivalents, with t-values falling well below the threshold for  $p < 0.05$ . A composite image showing the PSFs and spherical void simulations of the four focal zones chosen are depicted in Fig. 2.10. The benefit of the hybrid apertures is most apparent at the extremes of each focal zone. In some instances, the voids appeared murky when imaged with the spherical aperture but were well distinguished with the hybrid beam, e.g. at the 16 and 44 mm depths.

We should note that both the hybrid and purely spherical focused apertures used in the simulations were not amplitude apodized. The outer portion of the optimal array apertures demonstrated in this paper is effectively phase apodized. Including amplitude apodization at the edge of a spherically focused array may yield similar results; a comparison would be interesting to investigate in future work.

Beam parameters that are most important to image quality include the lateral and axial resolutions, depth of field, contrast, and frame rate [24]. Our results suggest that hybrid beamforming results in improved image quality, producing a long narrow beam that performs well at lower depths without sacrificing lateral resolution at the focus. This focusing scheme would also be advantageous in ultrasound transmit beams because fewer beams would be needed to cover the same depth range when compared to traditional spherical focusing. Being able to use fewer transmit pulses

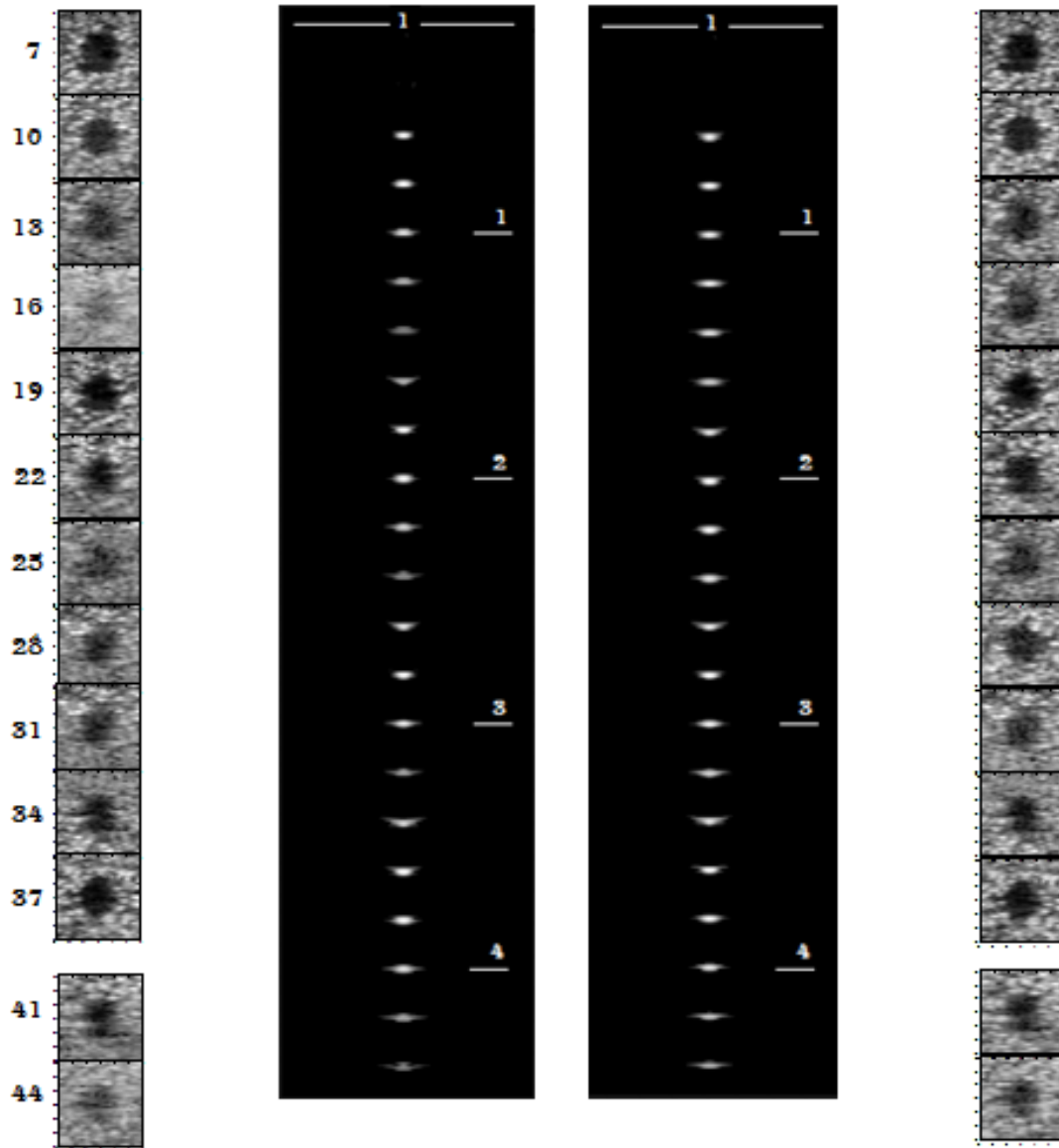


Figure 2.10: Point spread function and spherical void simulation comparison of spherical (left) and hybrid (right) apertures for a composite of the four focal zones over the entire 4.5 cm depth. The depth extremes of each of the four transmit focal zones of the spherical void simulations show higher sensitivity for the hybrid apertures.

would allow an increase in frame rate and thus be especially favorable in applications limited by low frame rate such as Doppler and compound ultrasound imaging.

### **2.4.3 Beam Steering**

Beam steering is useful to get extra information when transducer scanning angle is limited. When steering with reconfigurable arrays, the improvement in beam quality is most noticeable in the C-scan as phase delay errors are pronounced at various angles from the central axis when steering. By quantizing the delays, the maximum error of any subelement is decreased and instead distributed evenly over all the subelements. This results in removing the large artifact present in regular ring selection due to concentrated energy and spreading the side lobe energy around the PSF instead. We should note that there will still be grating lobes due to insufficient array sampling at a large steering angle; however, we found that minimizing phase error delay via delay quantization reduces excess side lobe energy associated with grating lobes as well.

The resulting PSF of the steered beam also illustrates the inherent advantage of reconfigurable arrays. Because it uses annular focusing, the beam width in the lateral direction is similar to that in the elevational direction, leading to an isotropic PSF or resolution. This uniformity improves ultrasound image quality when compared to traditional linear arrays because there will be minimal volume averaging due to the elevational beam width.

## **2.5 Conclusion**

The reconfigurability of 2D arrays affords beamforming flexibility with only a limited number of channels. Annular arrays represent a logical implementation of reconfigurable arrays. Although 12 elements were shown to be sufficient for annular array imaging [2] given the constraints of reliability of many coaxial cables under constant mechanical motion, we have found that increasing the number

of elements drastically improves image quality. This reconfigurable concept can be extended to hybrid beamforming, which improves image quality for a given number of focal zones at the focal depth extremes when compared to spherical focusing. Hybrid beamforming can potentially reduce frame rate as well because less number of transmit beams will be needed to cover the same depth range. Furthermore, reconfigurable arrays are also amenable to beam steering which is critical in diagnostic ultrasound imaging for obtaining better beam coverage when translating the active aperture is not an option.

## BIBLIOGRAPHY

- [1] M. Arditi, F. S. Foster, and J. W. Hunt, “Transient fields of concave annular arrays,” *Ultrasonic Imaging*, vol. 3, no. 1, pp. 37–61 <http://www.ncbi.nlm.nih.gov/pubmed/7195094>, 1981.
- [2] F. S. Foster, J. D. Larson, M. K. Mason, T. S. Shoup, G. Nelson, and H. Yoshida, “Development of a 12 element annular array transducer for realtime ultrasound imaging,” *Ultrasound in medicine biology*, vol. 15, no. 7, pp. 649–59, 1989.
- [3] R. Fisher, K. Thomenius, R. Wodnicki, R. Thomas, S. Cogan, C. Hazard, W. Lee, D. Mills, B. Khuri-Yakub, A. Ergun, and G. Yaralioglu, “Reconfigurable arrays for portable ultrasound,” vol. 1, pp. 495–499, 2005.
- [4] S. Cogan, R. Fisher, K. Thomenius, and R. Wodnicki, “2b-1 solutions for reconfigurable arrays in ultrasound,” pp. 116–119, 2006.
- [5] K. Thomenius, R. Fisher, D. Mills, R. Wodnicki, C. Hazard, and L. Smith, “Mosaic arrays using micromachined transducers,” US Patent 6,865,140, March 8, 2005.
- [6] “Iec 61391-1: Ultrasonics – pulse-echo scanners – part i: Techniques for calibrating spatial measurement systems and measurement of system point spread function response,” in *International Electrotechnical Commission*, (Geneva), 2006.

- [7] J. H. McLeod, “The axicon: A new type of optical element,” *Journal of the Optical Society of America (1917-1983)*, vol. 44, p. 592, 1954.
- [8] S. Fujiwara, “Optical properties of conic surfaces. i. reflecting cone,” *Journal of the Optical Society of America (1917-1983)*, vol. 52, p. 287, 1962.
- [9] M. S. Patterson and F. S. Foster, “Acoustic fields of conical radiators,” *Sonics and Ultrasonics, IEEE Transactions on*, vol. 29, no. 2, pp. 83–91, 1982.
- [10] C. B. Burckhardt, H. Hoffmann, and P. A. Grandchamp, “Ultrasound axicon: a device for focusing over a large depth,” *The Journal of the Acoustical Society of America*, vol. 54, no. 6, pp. 1628–1630, 1973.
- [11] S. Holm, “Bessel and conical beams and approximation with annular arrays,” *Ultrasonics, Ferroelectrics and Frequency Control, IEEE Transactions on*, vol. 45, no. 3, pp. 712–718, 1998.
- [12] K. Yamada, K. Tasei, and K. Nakamura, “Weighted conical transducer for generation of bessel beam ultrasound,” pp. 613–618 vol.1, 1992.
- [13] J. Durnin, “Exact solutions for nondiffracting beams. i. the scalar theory,” *Journal of the Optical Society of America A*, vol. 4, pp. 651–654, 1987.
- [14] J. Y. Lu and J. F. Greenleaf, “Nondiffracting x waves-exact solutions to free-space scalar wave equation and their finite aperture realizations,” *Ultrasonics, Ferroelectrics and Frequency Control, IEEE Transactions on*, vol. 39, no. 1, pp. 19–31, 1992.
- [15] S. I. Umemura, T. Azuma, Y. Miwa, K. Sasaki, T. Sugiyama, T. Hayashi, and H. Kuribara, “Non-cylindrical transmission focusing for large depth of field,” in *IEEE Ultrasonics Symposium*, vol. 2, pp. 1721–1724, 2002.



- [16] S. D. Pye, W. Ellis, and T. MacGillivray, “Medical ultrasound: a new metric of performance for grey-scale imaging,” *Journal of Physics: Conference Series*, p. 187, 2004.
- [17] J. T. Bushberg, J. A. Seibert, E. M. Leidholdt, and J. M. Boone, *The Essential Physics of Medical Imaging*. Philadelphia, PA: Lippincott Williams & Wilkins, 2nd ed., 1993.
- [18] P. C. Li and M. Odonnell, “Improved detectability with blocked element compensation,” *Ultrasonic Imaging*, vol. 16, no. 1, pp. 1–18, 1994.
- [19] G. Kossoff, “Analysis of focusing action of spherically curved transducers,” *Ultrasound in Medicine & Biology*, vol. 5, no. 4, pp. 359–365, 1979.
- [20] J. A. Jensen and N. B. Svendsen, “Calculation of pressure fields from arbitrarily shaped, apodized, and excited ultrasound transducers,” *Ultrasonics, Ferroelectrics and Frequency Control, IEEE Transactions on*, vol. 39, no. 2, pp. 262–267, 1992.
- [21] J. M. Kofler and E. L. Madsen, “Improved method for determining resolution zones in ultrasound phantoms with spherical simulated lesions,” *Ultrasound in medicine & biology*, vol. 27, no. 12, pp. 1667–76, 2001.
- [22] J. M. Kofler, M. J. Lindstrom, F. Kelcz, and E. L. Madsen, “Association of automated and human observer lesion detecting ability using phantoms,” *Ultrasound in Medicine & Biology*, vol. 31, no. 3, pp. 351–359, 2005.
- [23] B. J. Oosterveld, J. M. Thijssen, and W. A. Verhoef, “Texture of b-mode echograms: 3-d simulations and experiments of the effects of diffraction and scatterer density,” *Ultrasonic Imaging*, vol. 7, no. 2, pp. 142–60 <http://www.ncbi.nlm.nih.gov/pubmed/3909602>, 1985.

- [24] J.-Y. Lu, H. Zou, and J. F. Greenleaf, “Biomedical ultrasound beam forming,”  
*Ultrasound in Medicine Biology*, vol. 20, no. 5, pp. 403–428, 1994.

## CHAPTER III

# Speed of Sound Imaging using First Arrival Traveltimes

### 3.1 Background

Speed of sound information when added to B-mode images and other modalities achieves high specificity and sensitivity in detecting breast cancer lesions. Malignant breast cancer lesions have an elevated speed of sound of greater than 1500 m/s in comparison to breast fat tissue [1, 2], with some overlap with other breast tissues. Some of the rare liposarcomas, <0.01% incidence, may be a rare exception [3, 4].

Speed of sound imaging of the breast has been extensively investigated in various systems, recently in a ring-like CT configuration such as the system at Karmanos Cancer Institute [1, 5] and rotating opposed arrays [4, 6]. Our Breast Laser and Ultrasound Combined Imaging (BLUCI) system operates in the compressed breast geometry, similar to mammography. In this geometry, there is no freedom of rotation to obtain angles from the side of the breast. Even if transducers were placed accordingly to acquire the missing angles, the acoustic path length would be quite long and is subject to high attenuation and complex beam paths. However, some advantages of this compressed breast configuration include traveling through a small thickness of the breast, averaging 6 cm compressed, and allowing use of a higher center frequency than with the 15 cm average superior/inferior width at the chest wall of the breast when suspended freely in water.

With our BLUCI system, current studies include imaging the breast from both sides, photoacoustic tomography of the breast in the same geometry [7], and image based registration of BLUCI images with combined ultrasound and tomosynthesis images obtained in a different system [8]. The ability to create reasonably good speed of sound images in the compressed mammographic geometry will yield manifold benefits in our system, as they may be readily co-registered to these different modalities, particularly tomosynthesis, for breast cancer detection and characterization studies.

There are several approaches to speed of sound imaging, ranging from algorithms based in ray tracing optics [1, 5] to inverse scattering algorithms based on diffraction tomography [9], iterative Born approximation [10], and full-wave inverse scattering [4]. The main limitations of algorithms utilizing the full wave equation are the computational power and memory storage required to solve those problems, along with the ability to characterize the ultrasound transducers to sufficient accuracy in order to obtain the correct answer. Current investigation [11] with this method shows promise as far as having a tractable solution, and is being developed for improved accuracy for practical implementation.

We present a method of speed of sound reconstruction using the eikonal forward solver, which is a ray optics based, simplified model of the wave equation. Because our system only has limited viewing angles, we choose to characterize our misfit function in terms of covariance based matrices, yielding a more intuitive regularization method without dealing with *ad hoc* Tikhonov tuning parameters [12] and the ability to incorporate known homogeneous regions into the inversion to reduce artifacts stemming from limited views. The details of the inverse method will be delineated and results will be shown with simulated and experimental data obtained with dual opposed arrays.

## 3.2 Inverse Theory

The speed of sound inverse problem is quantified in the following equation:

$$Ls = t \tag{3.1}$$

where  $L$  is the ray path from transmitter to receiver,  $s$  is the slowness, or inverse velocity, of the imaged object, and  $t$  the time-of-flight needed to reach the receiver. Because the path length  $L$  is not readily known in an inhomogeneous medium due to beam bending, the problem requires an iterative algorithm sometimes called a bent-ray algorithm. The equation to solve is thus:

$$Lds = dt \tag{3.2}$$

where  $ds$  is the update to the slowness vector and  $dt$  is the difference in time-of-flight between that of a given speed of sound distribution and the actual recorded time of flight. In order to generate  $L$  and  $dt$ , the 2D eikonal wave equation comes into focus:

$$\frac{\partial^2 T}{\partial x^2} + \frac{\partial^2 T}{\partial y^2} = \frac{1}{v^2} = s^2 \tag{3.3}$$

The equation is an approximation to the wave equation, representing the chosen forward model for this problem. The input of the model is  $v$ , the sound speed, or  $s$ , slowness, inverse sound speed, and the output of the model gives  $T$ , the travel time from a source to any specific point in space. Given a specific speed of sound distribution, the expected time of flight can be computed, and consequently,  $dT$ . The path length matrix  $L$  accompanies this computation; using the gradient of the time map calculated for each source transmitter, one can trace each ray from a given receiver to transmitter by following the gradient vector backwards.

Given  $L$  and  $dT$ , we proceed to compute  $ds$  by minimizing the following cost

function of this step-wise linearized problem [13]:

$$2S = \|g(m) - d_{obs}\|_D^2 + \|m - m_{prior}\|_M^2 \quad (3.4)$$

The first term operates in data space while the second operates in model space.  $g(m)$  is the forward operator operating on the model function; in this problem, our forward model is the eikonal solver.  $d_{obs}$  is the observed data (simulated or experimental), and we seek to limit the difference between expected and observed data with the first term. The second term operates in model space. In this function, we treat  $m$ , the unknown, as a sample of known Gaussian probability density whose mean is centered at  $m_{prior}$ .

The misfit function can be written in terms of covariance to implement elegant regularization based on physical known values:

$$2S = (g(m) - d_{obs})^T C_D^{-1} (g(m) - d_{obs}) + (m - m_{prior})^T C_M^{-1} (m - m_{prior}) \quad (3.5)$$

where  $C_D$  denotes the data covariance matrix and  $C_M$  the model covariance matrix. As each data acquisition is considered independent,  $C_D$  is comprised of a diagonal with the value of epsilon, or the error between different data acquisitions.  $C_M$  allows us the flexibility of regularization based on actual physical values as we can constrain the standard deviation of values to lie within the expected region. The covariance matrix also enables us to correlate adjacent pixels to each other, which aids the inversion algorithm, and, as illustrated later, greatly diminishes the artifacts introduced with the limited aperture given sufficient *a priori* information.

The update will be iterative, and follows the schematic denoted in Fig. 3.1. The iteration stops when the problem reaches convergence, which can be set to a criterion based on the misfit error between actual data and expected data from our forward model for all transmit-receive pairs as denoted in the following equation:

$$error = \sum (T_{model} - T_{observed})^2 \quad (3.6)$$

To note, solving this problem requires high accuracy of the forward eikonal solver and precise knowledge of transmitter and receiver locations. We shall demonstrate our calibration methods when using two commercial transducers mounted in an opposed array geometry. These methods have been sufficiently accurate to ensure convergence in our inverse problem.

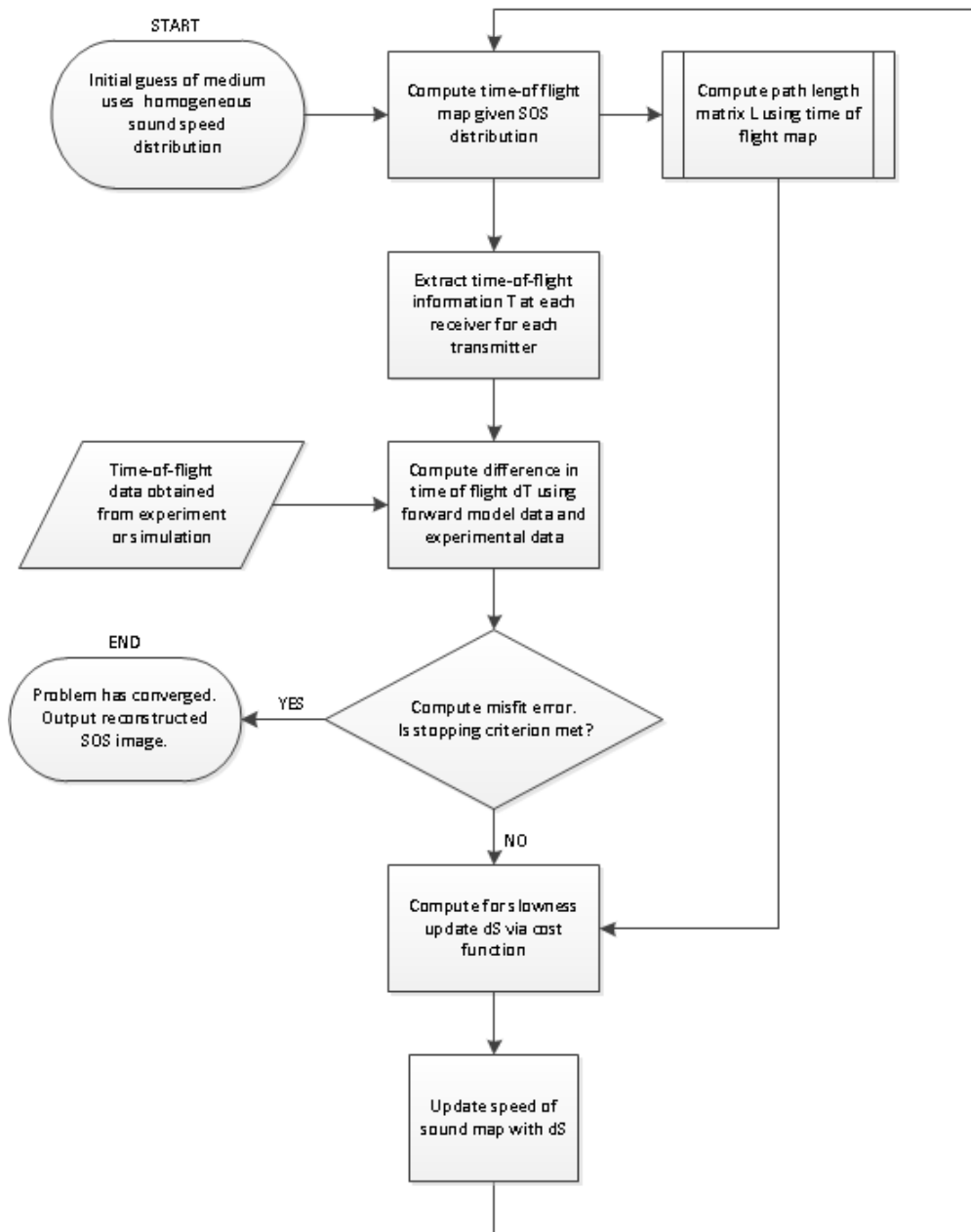


Figure 3.1: Schematic of inverse problem algorithm is shown. The iteration starts with an initial guess using a homogeneous medium, and ends when the problem has converged when the misfit error satisfies a chosen criterion.



## 3.3 Application

### 3.3.1 Eikonal Forward Model

When using commercial transducers in the compressed breast geometry, the relative location of the transmitting and receiving element is not fixed; furthermore, with such transducers, there is the presence of a lens with a drastic change in sound speed that will affect time-of-flight data calculations nontrivially. Careful calibration and forward modeling is essential in order to ensure problem convergence.

This paper examines the use of two ATL L7-4 linear arrays (ATL/Philips, Bothel, Washington) to obtain speed of sound reconstructions with phantom data. Details in proper forward modeling of the problem, obtaining the precise location of the transmitter and receiver elements (to sub-wavelength accuracy), and extracting time-of-flight information will be delineated.

To compute the eikonal equation, a 2D multi-stencil fast marching algorithm was implemented [14, 15]. In relation to the cost function, the eikonal solver is used to compute the  $g(m)$  term, that is the forward model operating on our model function. Given a source element location and a speed map, the output of the model is a time map that depicts the time of flight from a source to any given location in physical space. As the receiver location does not always coincide with a grid location, we perform bilinear interpolation of the four adjacent nodes to extract the time-of-flight.

To compute the pathlength matrix  $L$ , the path is first traced in physical space following the gradient (which essentially gives a direction vector onto which to traverse) until it is sufficiently close to the source. The pathlength matrix is then constructed accordingly with the desired grid spacing.

### 3.3.2 Cost Function Minimization via Conjugate Gradient Updates

Let us define  $m$  to be:

$$m = s - s_{background} \quad (3.7)$$

This allows us to work with smaller, contrast values and ensure a Gaussian probability distribution since the contrast can take both positive and negative values. The contrast value will be defined in relation to the slowness of the background. To obtain  $m_{prior}$ ,  $s$  is set to the mean value of the Gaussian distribution, which is also the slowness of the background. This yields an  $m_{prior}$  of 0.

We solve the inverse problem by minimizing the cost function via a conjugate gradient update. The steepest descent vector update for this problem can be computed as:

$$\gamma = C_M L C_D^{-1} (g(m) - d_{obs}) + m - m_{prior} \quad (3.8)$$

The conjugate gradient updates are then given by:

$$m = m_{n-1} - \alpha_n v_n v_n = \gamma_n + \beta_n v_{n-1} \quad (3.9)$$

where  $m$  is the model vector,  $v$  is the search direction, and  $\alpha$  is the step length. The value of  $\beta$  is determined via Polak-Ribière method, and the step length is chosen such that the cost function is minimized at each step. This parameter is derived analytically to be:

$$\alpha_n = \frac{v_n C_M^{-1} \gamma}{(L v_n)^T C_D^{-1} (L v_n) + v_n C_M^{-1} v_n} \quad (3.10)$$

### 3.3.3 Choice of Covariance Matrices

#### Variance Values

As pointed out in [11], the advantage of covariance-based cost functions is regularization, chosen specifically given the physical *a priori* information for the problem. There are two covariance matrices in this problem—one that operates on

the data space, and one on the model space. Both shall be examined in detail below.

Each pixel in the image is treated as a Gaussian distribution with a corresponding standard deviation it is constrained to oscillate between. To construct the covariance matrix, the values are denoted as follows:

$$C = \begin{pmatrix} \rho_{11}\sigma_1\sigma_1 & \rho_{12}\sigma_1\sigma_2 & \rho_{13}\sigma_1\sigma_3 & \dots \\ \rho_{21}\sigma_2\sigma_1 & \rho_{22}\sigma_2\sigma_2 & \rho_{23}\sigma_2\sigma_3 & \dots \\ \rho_{31}\sigma_3\sigma_1 & \rho_{32}\sigma_3\sigma_2 & \rho_{33}\sigma_3\sigma_3 & \dots \\ \dots & \dots & \dots & \dots \end{pmatrix} \quad (3.11)$$

where  $\rho_{ij}$  is the correlation coefficient between the  $i^{th}$  and  $j^{th}$  pixel, and  $\sigma_i$  is the standard deviation set for the  $i^{th}$  pixel.

The data covariance matrix  $C_D$  encompasses experimental noise. As the noise is usually independent from acquisition to acquisition,  $C_D$  should be made up of only diagonal elements with the rest set to 0. The amount of noise expected from our data acquisition becomes the value of  $\sigma$ .

The model covariance matrix  $C_M$  controls the extent that which the model function varies, and one can also adjust the correlation between pixels with this matrix. Note that if each pixel is deemed independent and allowed to vary identically,  $C_M$  is reduced to a constant diagonal and the problem is simplified into Tikhonov regularization. The use of  $C_M$  is ideal because it eliminates the painstaking need to determine the optimal Tikhonov tuning parameter with each different problem, but rather, be set to the real physical expected values for the given experimental setup and domain. Furthermore, it also enables the flexibility for spatial regularization of the inverse problem. We will show later in this chapter that this flexibility will enable us to reduce the artifact introduced by limited angle acquisitions. In the context of this problem, the variances in  $C_M$  are chosen as follows:

$$\sigma = \max(s_{\text{minimum}} - s_{\text{background}}, s_{\text{maximum}} - s_{\text{background}}) \quad (3.12)$$

Where  $s_{background}$  is the slowness of the background as defined in Eq. 3.7, and  $s_{minimum}$  and  $s_{maximum}$  are the minimum and maximum slowness you expect your model function to attain.

## Storage and Computation

We need to note that although the size of the covariance matrices is very large ( $N^2$  x  $N^2$ ), with  $N$  being the number of pixels in the image, they are in fact sparse and symmetric. The inverse covariance matrices are never actually computed but solved via a mini-inverse problem in the context of the equation we implement the LSQR method for this purpose.

### 3.3.4 Experimental Setup

Two ATL L7-4 linear arrays are mounted opposing each other in a water tank, and are connected to the Verasonics system, which allows for independent channel and element control for speed of sound data acquisitions (Fig. 3.2). The distance between these two transducers can be altered, and care was taken to machine the mounts to be as symmetric as possible. The arrays are comprised of 128, 300  $\mu\text{m}$  elements, which at a distance of 5-6 cm is suitable for approximately an angular range of 30. The exact location of the transducer elements are determined via careful water-shot calibration.

Data is acquired at a frequency of 3.75 MHz. Although the frequency is slightly below the bandwidth of the transducer, the pulses look well-formed without signal-to-noise ratio complications. Each element on the transmitter is fired once and recorded on all 128 elements of the receiving transducer for a full RF dataset of 128 x 128 traces.

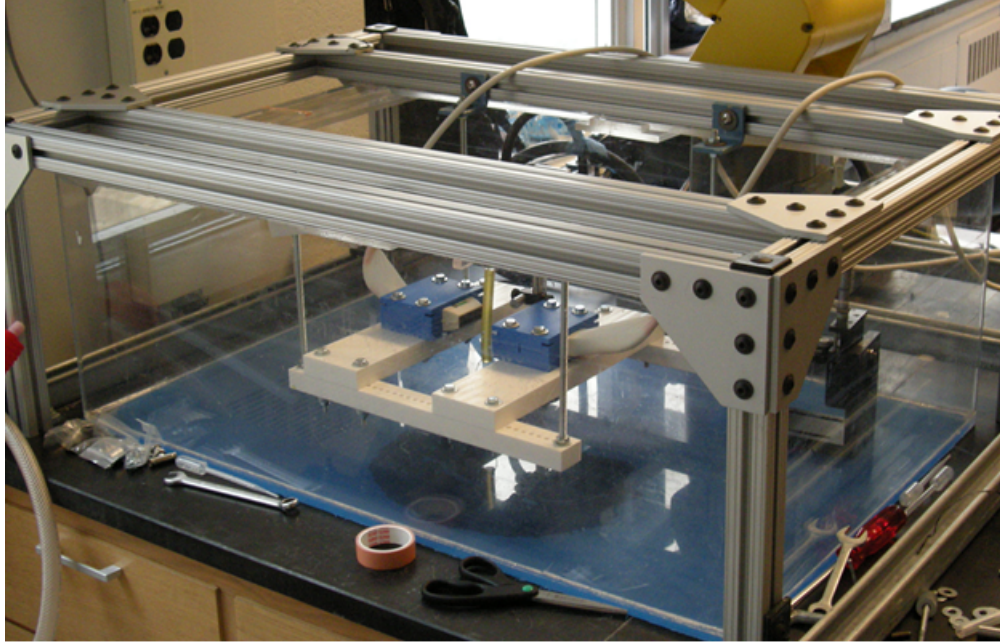


Figure 3.2: Experimental setup with two ATL L7-4 linear arrays. The distance between both transducers is approximately 5 cm apart, which is the average thickness of a compressed breast. A worm rubber contrast is placed in the center and the tank is filled with water for experimental data collection.

### Eikonal Forward Modeling

For experimental data, a matching lens layer was input into the simulation grid as well. Setting the values that correspond to the pixels that encompass the entirety of the lens is trivial—however, at the edges where the lens does not occupy the complete pixel, a mean sound speed is calculated for those pixels instead based on the proportion of the pixels the lens occupies.

In order to achieve the level of accuracy necessary for speed of sound reconstructions, grid spacing must be sub-wavelength in size. However, the grid must not be too fine because computation complexity increases with  $O(N^2)$ , with  $N$  being the number of pixels, not to mention the amount of memory necessary to store the time maps for each source transmitter. To find the optimal grid cell size, we compared the error found with different cell sizes with analytical truth based on Fermat’s principle.

## **Inverting for Transmit and Receive Element Locations**

To create a precise forward model of the problem, it is crucial to know the position of each transmit and receive element within fractions of a wavelength. Assuming that once mounted, the transducers do not move, we solve an inverse problem in order to invert for the positions of each element.

We set the transmit transducer to a fixed location and search for a vector that delineates the location of the receive transducer in terms of axial and lateral distance, along with rotation of the transducer where the axis of rotation is perpendicular to the face of the transducer. We perform a minimization problem with an initial crude guess given the axial distance between the transducers, and set the lateral distance and rotation to 0. In essence, we seek to minimize the difference in time of flight produced by the forward model and the time of flight recorded with watershot data as we adjust the receiving transmitter to minimize the misfit in the cost function. We do this with the built-in MATLAB `fminsearch` function.

Note that this minimization problem assumes that the transducers are lined up well elevationally because it cannot differentiate the difference in time of flight when the receiving transducer is in plane with the transmitting transducer, or within the arc of the same distance. The position inversion algorithm is very computationally expensive but very simply parallel. The inversion was performed by enabling shared memory access within the operating system and taking advantage of a multiple core CPU, readily available within the MATLAB file exchange [16].

## **Time of flight Picker**

There are many ways to approach time of flight extraction, with correlation methods being very robust given correct windowing [17] and good first arrival methods. The latter are available, stemming from seismology and involving use of the Akaike Information Criterion (AIC) [18]. We will use a combination of both methods to

extract time of flight information from our experimental data.

We first construct an empirical matched filter using a water shot dataset for calibration. Using the weighted AIC criterion [18], we extract the window of each received pulse by determining the time that the pulse arrives, and as the criterion works symmetrically, the time the pulse finishes as well. The pulses are all then averaged by taking the mean signal at each time increment to produce a mean receive pulse over all transmit-receive pairs. The transmit pulse found in the beginning of each trace is then obtained and also averaged across all traces to obtain an averaged transmit. The averaged receive pulse is correlated to this transmit section to obtain the system lag, that is the delay before the transducer actually begins transmitting pulses—the empirical matched filter is thus obtained by padding the average received pulse with the measured offset so that the time of flight information extracted will take the delay in transmitting the signal out of the element into account.

To extract the time of flight information from the recorded datasets, we implemented a correlation based method with interpolated RF traces. This approach yielded a time of flight matrix with excellent accuracy when tested with the water path dataset, with average error ranging from 0.02-0.05  $\mu\text{s}$ , well within the resolution of the sampling rate of the Verasonics system.

## 3.4 Results

### 3.4.1 Simulated Speed of Sound Reconstructions

To simulate two linear array transducers, 128 transmitters and receivers were placed on opposite sides at a distance of 6 cm. Simulated time of flight data was obtained via the forward eikonal solver given different speed of sound maps. The background of the medium was set to 1500 m/s and the object SOS to 1440 m/s, well within the 7% now being reported in breast tissue with a range from 1410 for fat tissue to 1610 m/s for cancers [4].

To begin the iterations, an initial guess of the medium is needed for the forward model. The initial guess was set to a homogeneous medium coinciding with the background of 1500 m/s. The conjugate gradient update to the model was computed via methods delineated above and the model was updated accordingly. As a stopping criterion, the residual error computed after each iteration was used. Updates were stopped once the residual error began increasing.

The standard deviation  $\sigma$  of the data covariance matrix was set to 0.05 to reflect data measurement error, and 0.048 for the model covariance matrix to reflect variation in sound speeds between 1400-1600 m/s. Reconstruction without additional regularization is depicted in Fig. 3.3.

To further examine the usefulness of the covariance matrix, the pixels encompassing the contrasting cylinder were correlated in Fig. 3.4, that is, setting the correlation coefficient  $\rho_{ij}$  to a non-zero value when the  $i^{th}$  and  $j^{th}$  pixels are within the pixels of the cylinder. The SOS values initially obtained hovered at approximately 1470 m/s with no correlation within the model covariance matrix and 1440 m/s with the introduction of correlation.

The choice of correlation coefficient affects the improvement of the reconstruction. Reconstructions with different correlation values are demonstrated in Fig. 3.5. Higher correlation coefficients produce a greater improvement in the reconstructed image, although the highest value we chose was only 0.01. We show the cross-section through the contrasting object in Fig. 3.6.

To illustrate the extent of the smearing artifact ubiquitous in limited aperture acquisitions, an image is reconstructed where two circular cylinders of the same worm rubber of 6 mm diameter are stacked one above the other in the axial direction, without assuming a spatial correlation of the pixels Fig. 3.7. With covariance regularization with a correlation coefficient of 0.01, the two objects are now distinguishable from each other in Fig. 3.8.



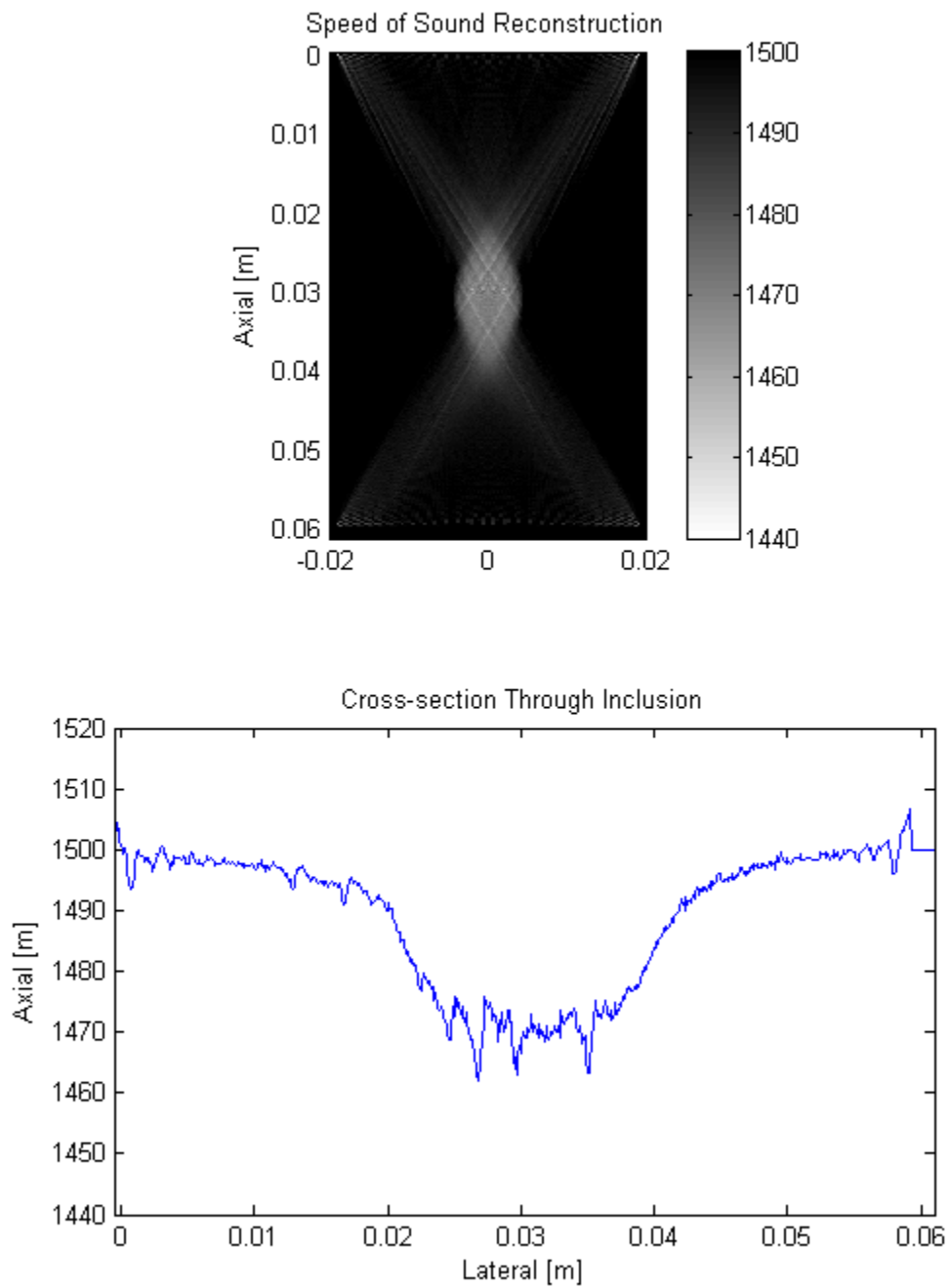


Figure 3.3: Reconstructed image with regularization based on *a priori* information on data and model space. There are some striations noted in the image resulting from undersampling with respect to the reconstructed grid. The reconstructed SOS value reached approximately 1470 m/s.

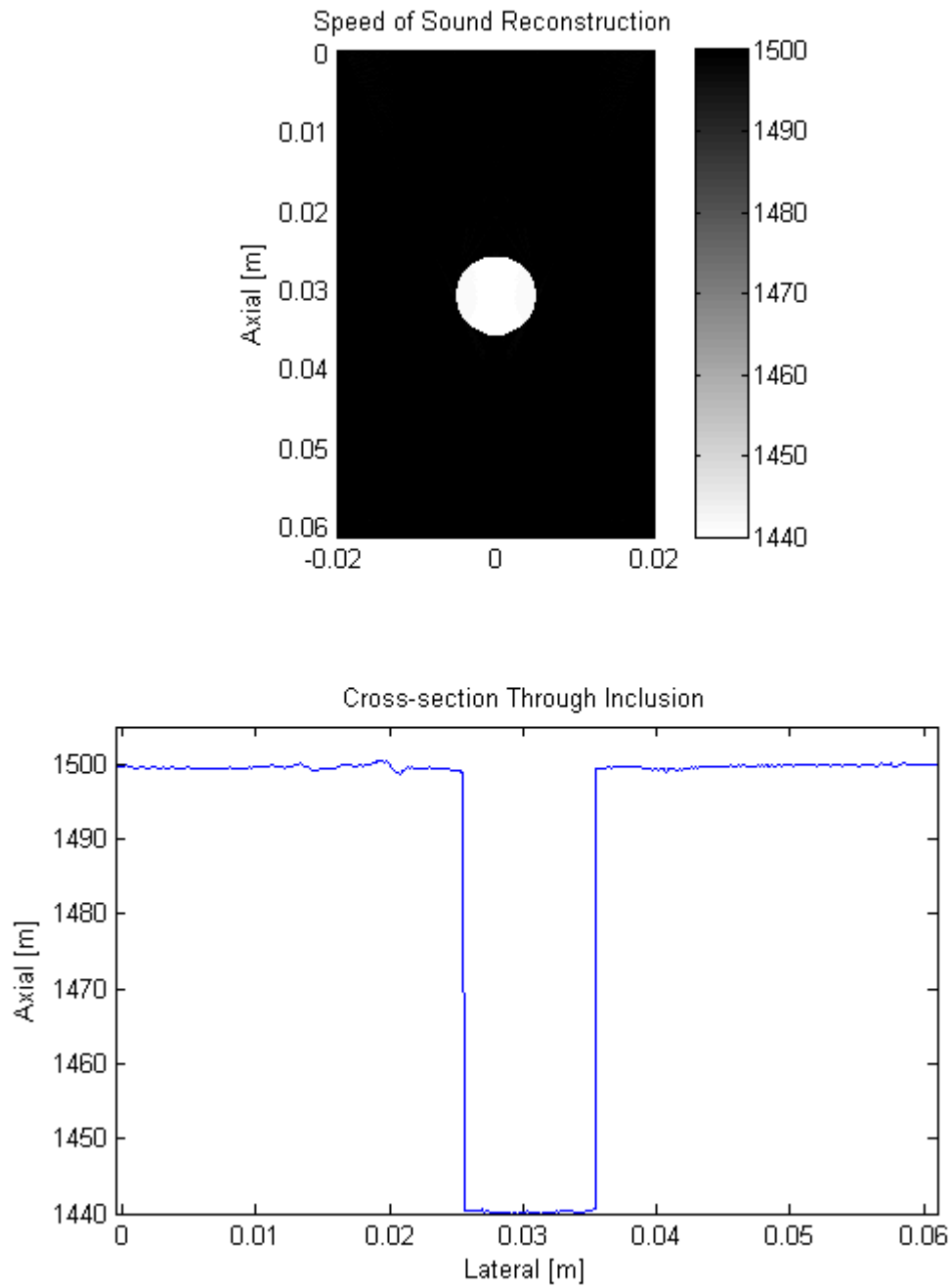


Figure 3.4: Reconstructed image from simulation includes regularization via correlation between assumed homogeneous pixels. The reconstructed image of cylinder reaches approximately 1440 m/s.

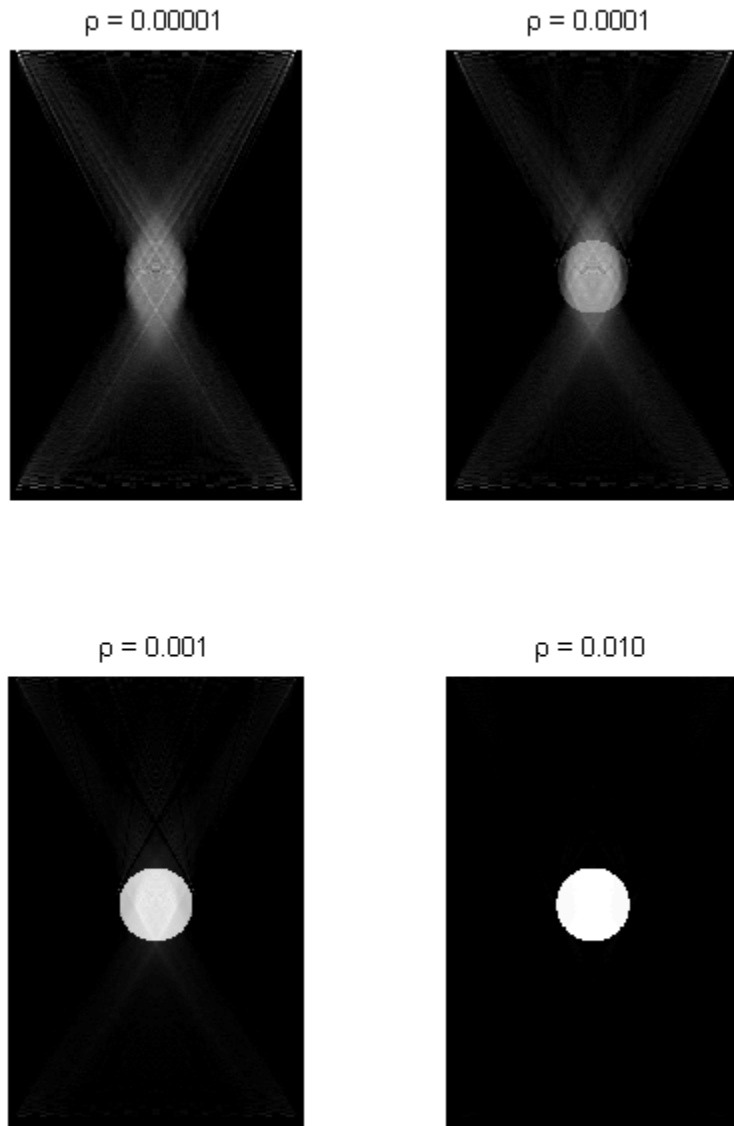


Figure 3.5: Images reconstructed from simulation with correlated homogeneous region with different correlation coefficient values. As the value increases, the reconstruction improves and limited aperture smearing artifact is diminished.

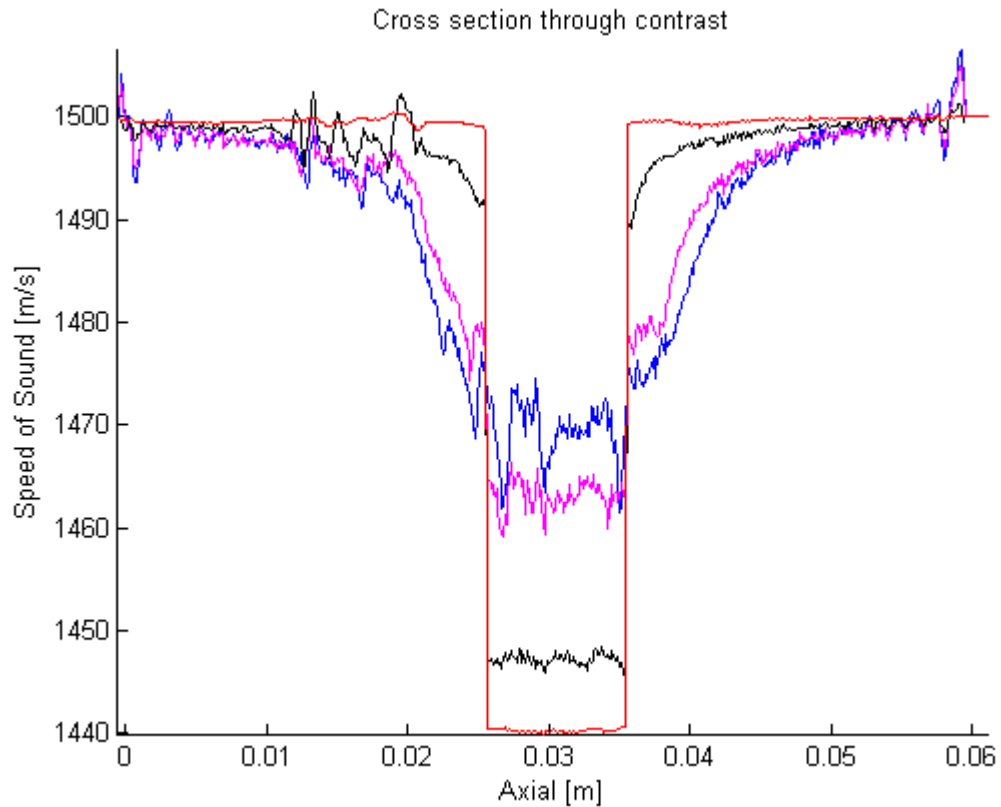


Figure 3.6: Cross-section through the simulated object when using different correlation coefficients. The speed of sound value obtained in the object monotonically approaches the correct value as we increase the value of the correlation coefficient in the values of Fig. 3.5 (0.00001 - Blue, 0.0001 - Magenta, 0.001 Black, 0.01 - Red).

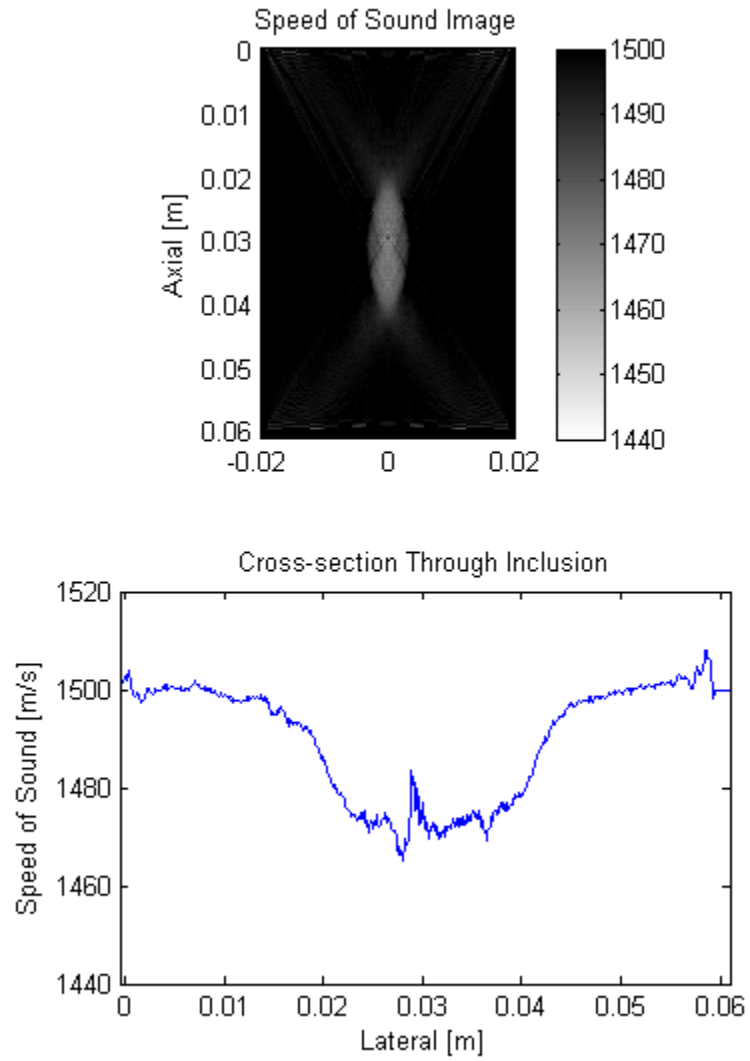


Figure 3.7: Two simulated 6 mm diameter cylinders placed close to each other to demonstrate the PSF overlap. The speed of sound dips only to 1470 m/s and the cylinders can barely be distinguished from each other.

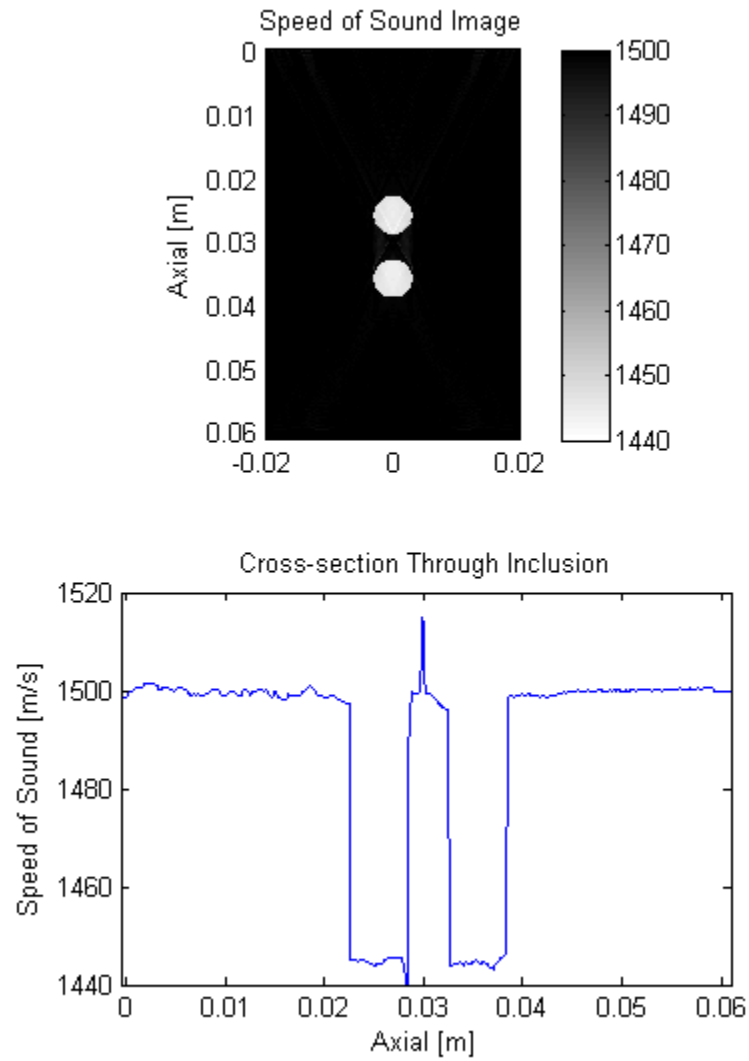


Figure 3.8: Reconstructed image of the same data as Fig. 3.7 but with pixels correlated together as assumed homogeneous regions. The two cylinders can now be differentiated from each other, and the reconstructed value reaches approximately 1440 m/s.

### 3.4.2 Speed of Sound Reconstructions with Experimental Data

#### Eikonal Forward Solver

It is important that our forward model accurately model the imaging setup. In order to determine the optimal grid spacing, the fineness of our grid spacing was varied and the mean error between each setup was compared. Given the current linear array setup with focusing lenses, the cell size of the grid should be at least at  $\lambda/6$  to achieve sufficient accuracy. Increasing the precision of the grid past that level depicted little increase in accuracy at a large cost of memory and computation.

#### Position Inversion of Transmitter and Receiver Elements

We found that even with fairly precise machining, the transducers were offset from each other in the lateral direction by approximately 1.1 mm (about three elements) and slightly angled with respect to each other (closer at one end than the other). Accounting for this slight misalignment, the median error in time of flight between expected and recorded signals was found to be approximately 1.2 ns without correction for individual element to element transit times.

Two data acquisitions were obtained: a water shot for system calibration, and an object shot with a 12.5 mm diameter cylindrical phantom made of rubber used for fishing worms (MF Plastics, Ft. Worth, TX) of a different speed of sound than the surrounding water medium. The reconstruction was initially performed without assuming spatially correlated pixels using both a pencil ray (Fig. 3.9) and a thicker ray L matrix (Fig. 3.10). Each ray was modeled as a generalized normal distribution where points within the main ray thickness of 300  $\mu\text{m}$  were weighted heavily, and a rapid falloff for points located approximately 50  $\mu\text{m}$  beyond the ray thickness was specified by a  $\sigma$  parameter to prevent over-fitting of the model. We found that varying the  $\sigma$  parameter showed minor changes in the image. Given the object location found from this latter image, local pixels were correlated in the same circular region for an

improved reconstruction. The algorithm was able to reconstruct the contrast with much better accuracy, with values in the object dipping to approximately 1400 m/s (Fig. 3.11).



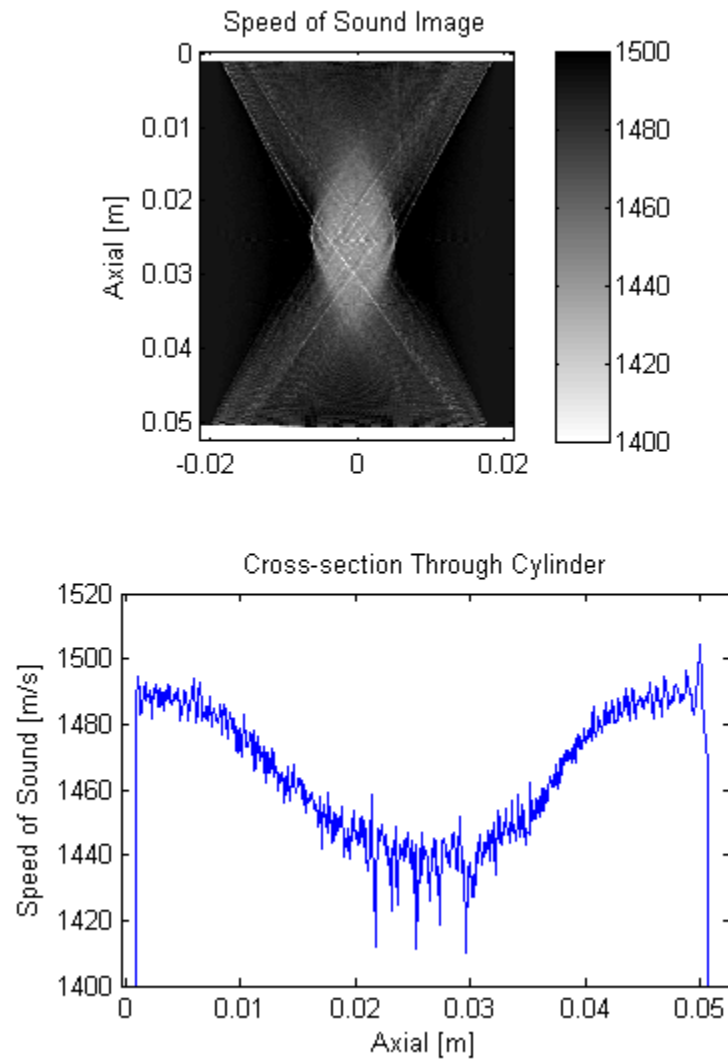


Figure 3.9: Experimental data was taken with 128 transmitters and 128 receivers placed in an opposed array geometry with a cylinder of 1406 m/s placed in the center. The contrast is recovered, and the diamond shaped point spread function is noticeable. Similar to simulation, the value within the contrasting cylinder dips to approximately 1440 m/s due to the smearing artifact.

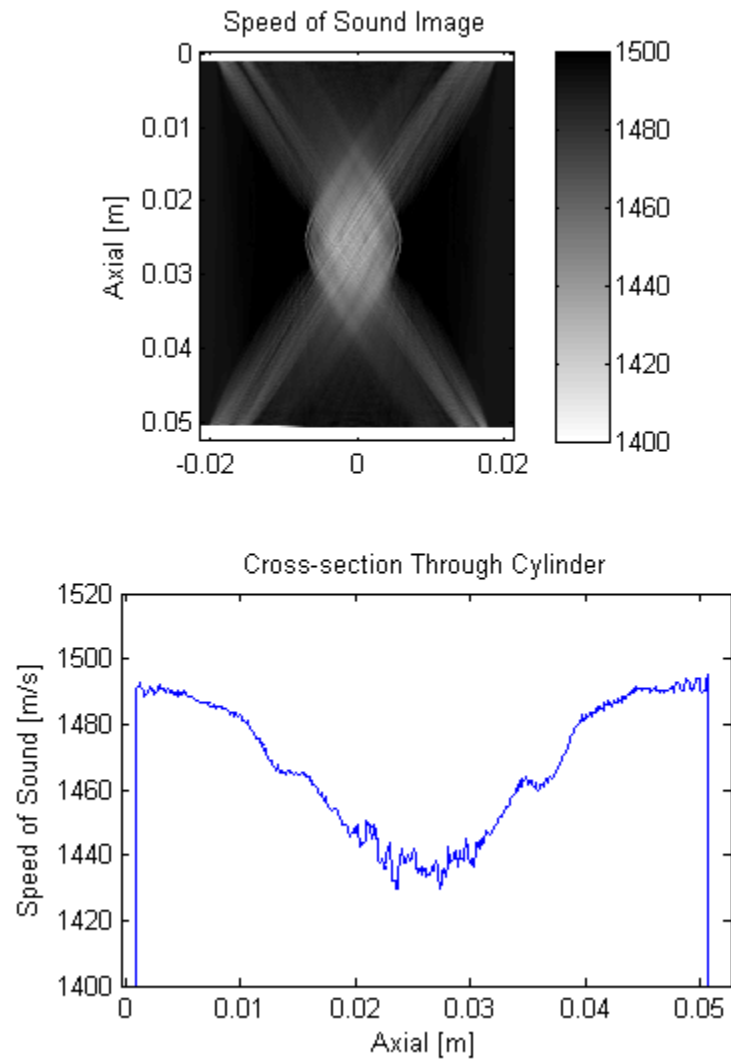


Figure 3.10: A thick ray implementation of the path length matrix is demonstrated. The speed of sound image is smoother when compared to the pencil ray implementation. The value within the contrasting cylinder is similar, but the microvariations throughout the image are largely decreased.

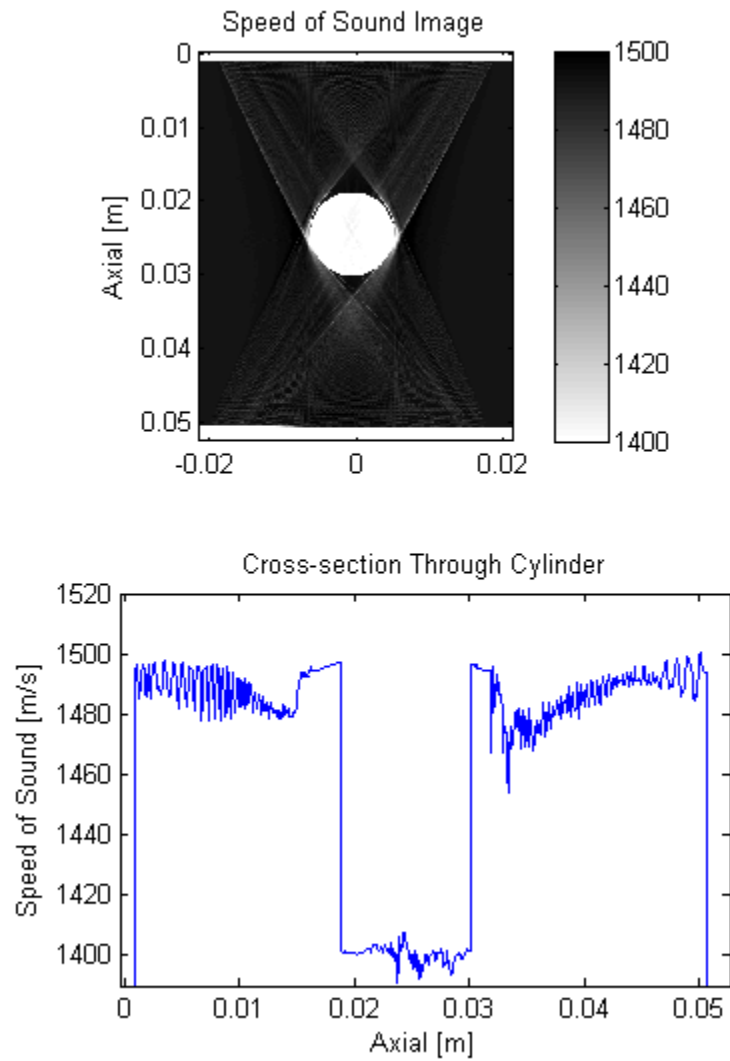


Figure 3.11: The homogeneous region was correlated together to aid the inversion. The reconstructed speed of sound value reached approximately 1400 m/s, which is more accurate than the inversion without regularization via correlated pixels.

## 3.5 Discussion

Because we are employing a limited aperture in this geometry, we expect to see elongation and spread ray artifacts similar to those found in other limited angle acquisitions such as in X-ray tomosynthesis. The resolution in the lateral direction is quite good, but the resolution in the axial direction is much poorer [19].

The advantage of this algorithm over other similar algorithms is the ability to define the regularization parameters directly based on the physical information of the problem. With the traditional bent-ray algorithm, choice of the Tikhonov tuning parameter highly affects the reconstruction and must be chosen via trial and error for each reconstruction.

A circle of 1 cm diameter was placed in the center of the simulated image and reconstructed with a diagonal model covariance matrix. There are some striations noted in the image (Fig. 3.9) which is attributed to the sparse sampling in comparison to the reconstruction grid. Currently, the transmitters and receivers are sampled at  $300\ \mu\text{m}$ , while the reconstruction grid has a spacing of  $100\ \mu\text{m}$ . Thus, there are some gaps at which some rays traverse certain pixels while missing adjacent ones completely. The algorithm currently assumes that the ray traverses through only 1 pixel at a time (assuming a pencil thin ray)—for more correct modeling, we may need to assume fat rays as we trace from receiver to transmitter so that this does not occur. However, this effect is highly diminished when we introduce correlation into the covariance matrix, as we shall demonstrate further in the paper. Cross-sections through reconstructed image (Fig. 3.11) still show micro-variation though, which can be attributed to this sampling artifact.

There is also a spread of energy in the axial direction corresponding to beams that go through the region of contrast in the image. This is intuitive and expected because we are currently missing angles from the side view. As a direct result, the true speed of sound is never quite attained, with values of the inclusion settling in

at approximately to 1470 m/s. The inclusion also resembles more of a diamond shaped instead of a circular region due to the locations of the transmitters and receivers. This is a fundamental limitation of the limited aperture method as there is insufficient information to remove the spreading energy artifact.

In order to reduce the smearing artifact presented with limited aperture acquisitions, we can use *a priori* information, such as that perhaps obtainable from fat vs. high water content or connective tissue segmentation of pulse echo images, guided by the initial speed of sound images, to essentially help the inversion in finding the correct answer (Fig. 3.4 and 3.8).

The improved images of Fig. 3.4 and 3.8 were obtained by only correlating the pixels in the inclusion; further refinement could also include correlating the background pixels as well. We need to note that when we start using large correlation regions, the covariance matrix will become less sparse thereby increasing the computational and storage complexity exponentially.

With the case of limited aperture acquisitions, the lateral resolution is quite good, but the axial resolution is poor. We demonstrate the inherent artifact when two regions are closely stacked in the axial direction (Fig. 3.7) and great reductions in artifacts when the pixels within the contrast are correlated (Fig. 3.8). There are still some artifacts present mostly between the two regions. This may be further refined in a few ways. For example, the background regions can also be correlated, the correlation values in the inclusion were set to a higher value, or perhaps fat rays incorporated into the model so that local pixels would mirror values closer to each other. The extra energy found in these artifacts accounts for the SOS values not reaching the true value of 1440 m/s.

The experimental data taken with a 12.5 mm diameter cylindrical inclusion of 1406 m/s and reconstructed without spatially correlated pixels resulted in a grainy image was formed with object SOS values close to 1450 m/s. The use of fat rays was

also explored briefly on this dataset. The major difference between the pencil ray and fat ray reconstruction was that the profile was significantly smoother in the fat ray case. The fat ray inversion however, is both more computationally demanding with a much higher storage cost as the sparsity of the  $L$  matrix is greatly reduced. Further efforts to optimize the fat ray inversion will be necessary to implement the inversion on a consistent basis.

Given the location of the contrasting object from the speed of sound image, local pixels in its given size and shape were correlated. With the added covariance matrix regularization via correlation with a coefficient of 0.01, the inclusion was recovered with SOS values at approximately 1400 m/s. The covariance matrix essentially constrains the algorithm such that the allotted pixels vary together, leading to a reduction in the inherent artifacts accompanying limited angle acquisitions (Fig. 3.11).

In a practical setting, one can use the ultrasound B-mode grayscale image and the initial SOS reconstructions to segment out likely homogeneous regions of high SOS contrast, which we can then feed into the inversion algorithm for improved speed of sound images in the limited aperture configuration. Segmentation methods on ultrasound B-mode images are beyond the scope of this dissertation however, and may be investigated for this application in a future study. Another possible approach may be to institute an adapting covariance matrix that changes depending on the answer of the present iteration. This allows us to not be completely reliant on the B-mode image for segmentation of regions which are not fully outlined in the pulse echo mode. Our work with two sided pulse echo imaging in the lightly compressed breast [20] should allow visualization of the distal side of a breast cancer which is often obscured in a single sided ultrasound image. The same linear arrays employed for pulse echo could be used for this limited angle SOS imaging.

As the inversion algorithm is developed based on a cost function, it can also be

readily extended to do inversion for attenuation and simultaneous inversion with synthetic aperture algorithms. It would only require a modification of the cost function and introduction of additional model functions in their respective model spaces.

The choice of covariance matrices strongly impacts the reconstruction image when acquiring with limited angles. As this matrix can be made very complex, determining the optimal covariance matrix to reconstruct images in an *in vivo* setting may be investigated thoroughly in a future paper.

### 3.6 Conclusion

We have demonstrated in this paper an algorithm that reconstructs speed of sound images with limited angled data. The goal of the algorithm is to illustrate the ability to form images using two opposed linear arrays to mimic ultrasound image acquisition in the compressed mammographic geometry. Images in this limited angle tomography are plagued by artifacts when using traditional ray tracing bent ray algorithms, with the additional necessity to tune parameters for each reconstruction. The use of a cost function defined via covariance matrices eliminates the need for such tweaking and instead offers more elegant regularization based on physical known values of the problem itself such as the dimensions of high contrast objects and their loosely estimated acoustic properties.

The model covariance matrix also yields a flexible method to constrain the problem to allow groups of contiguous pixels to vary together. This extra *a priori* information may be garnered from major breast structures noted in ultrasound B-mode, MRI, or X-ray CT images and is shown to drastically reduce the smearing artifacts that accompany reconstructions based on limited viewing angles.

## BIBLIOGRAPHY

- [1] C. Li, N. Duric, and L. Huang, “Breast Imaging Using Transmission Ultrasound: Reconstructing Tissue Parameters of Sound Speed and Attenuation,” *BioMedical Engineering and Informatics, International Conference on*, vol. 2, pp. 708–712, 2008.
- [2] J. S. Schreiman, J. J. Gisvold, J. F. Greenleaf, and R. C. Bahn, “Ultrasound transmission computed tomography of the breast.,” *Radiology*, vol. 150, pp. 523–530, Feb. 1984.
- [3] A. L. Scherzinger, R. A. Belgam, P. L. Carson, C. R. Meyer, J. V. Sutherland, F. L. Bookstein, and T. M. Silver, “Assessment of ultrasonic computed tomography in symptomatic breast patients by discriminant analysis.,” *Ultrasound in medicine & biology*, vol. 15, no. 1, pp. 21–28, 1989.
- [4] M. P. André, C. H. Barker, N. Sekhon, J. Wiskin, D. Borup, and K. Callahan, “Pre-Clinical Experience with Full-Wave Inverse-Scattering for Breast Imaging Acoustical Imaging,” vol. 29 of *Acoustical Imaging*, ch. 10, pp. 73–80, Dordrecht: Springer Netherlands, 2009.
- [5] C. Li, N. Duric, P. Littrup, and L. Huang, “In vivo breast sound-speed imaging with ultrasound tomography.,” *Ultrasound in medicine & biology*, vol. 35, pp. 1615–1628, Oct. 2009.
- [6] J. Wiskin, D. Borup, S. Johnson, M. Berggren, D. Robinson, J. Smith, J. Chen,



- Y. Parisky, and J. Klock, “Inverse scattering and refraction corrected reflection for breast cancer imaging,” vol. 7629, pp. 76290K+, SPIE, 2010.
- [7] Z. Xie, X. Wang, R. F. Morris, F. R. Padilla, G. L. Lecarpentier, and P. L. Carson, “Photoacoustic imaging for deep targets in the breast using a multichannel 2D array transducer,” *Proceedings of SPIE*, vol. 7899, pp. 789907+, Feb. 2011.
- [8] S. P. Sinha, M. A. Roubidoux, M. A. Helvie, A. V. Nees, M. M. Goodsitt, G. L. LeCarpentier, J. B. Fowlkes, C. L. Chalek, and P. L. Carson, “Multi-modality 3D breast imaging with X-Ray tomosynthesis and automated ultrasound,” in *Engineering in Medicine and Biology Society, 2007. EMBS 2007. 29th Annual International Conference of the IEEE*, pp. 1335–1338, IEEE, Aug. 2007.
- [9] F. Simonetti, L. Huang, and N. Duric, “Transmission and Reflection Diffraction Tomography in Breast Imaging,” in *2008 International Conference on BioMedical Engineering and Informatics*, pp. 723–727, IEEE, May 2008.
- [10] M. P. André, H. S. Janée, P. J. Martin, G. P. Otto, B. A. Spivey, and D. A. Palmer, “High-speed data acquisition in a diffraction tomography system employing large-scale toroidal arrays,” *Int. J. Imaging Syst. Technol.*, vol. 8, no. 1, pp. 137–147, 1997.
- [11] M. Haynes and M. Moghaddam, “Large Domain, Low-Contrast Acoustic Inverse Scattering for Ultrasound Breast Imaging,” *IEEE transactions on bio-medical engineering*, July 2010.
- [12] M. Moghaddam and W. C. Chew, “Simultaneous inversion of compressibility and density in the acoustic inverse problem,” *Inverse Problems*, vol. 9, pp. 715+, Dec. 1993.

- [13] A. Tarantola, *Inverse Problem Theory and Methods for Parameter Estimation*. 2004.
- [14] M. S. Hassouna and A. A. Farag, “MultiStencils Fast Marching Methods: A Highly Accurate Solution to the Eikonal Equation on Cartesian Domains,” *IEEE Transactions on Pattern Analysis and Machine Intelligence*, vol. 29, pp. 1563–1574, 2007.
- [15] D.-J. Kroon, “Accurate Fast Marching,” *MATLAB Central File Exchange*, 2011.
- [16] M. Buehren, “Multicore Parallel Processing on Multiple Cores,” *MATLAB Central File Exchange*, 2011.
- [17] T. L. Chenevert, D. I. Bylski, P. L. Carson, C. R. Meyer, P. H. Bland, D. D. Adler, and R. M. Schmitt, “Ultrasonic computed tomography of the breast. Improvement of image quality by use of cross-correlation time-of-flight and phase-insensitive attenuation measurements,” *Radiology*, vol. 152, pp. 155–159, July 1984.
- [18] C. Li, L. Huang, N. Duric, H. Zhang, and C. Rowe, “An improved automatic time-of-flight picker for medical ultrasound tomography,” *Ultrasonics*, vol. 49, pp. 61–72, Jan. 2009.
- [19] Y.-H. H. Hu, B. Zhao, and W. Zhao, “Image artifacts in digital breast tomosynthesis: investigation of the effects of system geometry and reconstruction parameters using a linear system approach,” *Medical physics*, vol. 35, pp. 5242–5252, Dec. 2008.
- [20] P. L. Carson, F. Zafar, S. A. Verweij, M. M. Goodsitt, G. L. LeCarpentier, S. Sinha, F. Hooi, M. Roubidoux, and J. B. Fowlkes, “Dual sided automated ultrasound system in the mammographic geometry,” Oct. 2011.

## CHAPTER IV

# Attenuation Imaging

### 4.1 Background

Attenuation imaging seeks to quantify the reduction in amplitude of the ultrasound beam as the wave propagates through the medium. Attenuation images can be obtained with the same data used to produce speed of sound images, and it has been shown that coupling attenuation information with speed of sound can improve the specificity and sensitivity in detecting breast lesions [1–9].

There are varied approaches to ultrasound attenuation tomography of the breast, encompassing different methods of obtaining the attenuation data given the RF signal [9–12]. However, there are several sources of error prevalent in attenuation imaging. This includes complex loss and interference of signals that are not fully accounted for in existing approaches to attenuation imaging from several sources. These signal loss mechanisms include diffraction, refraction, scattering, reflection, speed of sound variations, noise in the RF data, inadequate aperture and fine sampling of the transmitters and receivers, and inaccurate knowledge of their positions. The goal here is to obtain an attenuation coefficient representative of the bulk properties of the different tissues in the breast, i.e., including attenuation from local absorption and isotropic scattering of the ultrasonic energy. There have been several variations on attenuation tomography that account for the refraction effects by accounting for attenuation due to traversed pathlength [11] and refraction effects

using an angular spectrum method [12]. Without proper correction, attenuation images are sub-optimal, usually displaying enhanced attenuation and reduced attenuation therein around the lesion due to anisotropic attenuation at the boundaries and undetected energy.

An algorithm for attenuation image reconstruction is proposed that addresses the different sources of error noted above in the context of opposed imaging arrays for transmission data. An inverse problem is used to invert for element position location since the array positions are not static from acquisition to acquisition. Using a known speed of sound distribution, the attenuation data is corrected using data from a full wave forward model to account for any signal loss due to macroscopic speed of sound variations including scattering, and subcategories thereof, diffraction, and refraction, all without loss of the attenuation due to local energy absorption and isotropic scattering. To construct the attenuation image, a regularized least squares algorithm in weighted space is solved to account for experimental noise and *a priori* information based on the size, shape, and expected variation of attenuation values by characterizing our misfit function in terms of covariance based matrices. The method is demonstrated on experimental data of a simple cylindrical phantom to illustrate the working algorithm on real-world data obtained from a pair of commercial ultrasound transducers.

## 4.2 Inverse Theory

Attenuation imaging is largely based on the existence of a speed of sound map, which is delineated in the previous chapter. The analogous attenuation inverse problem is quantified in the following equation:

$$La = C \tag{4.1}$$

where  $L$  is the ray path from transmitter to receiver, whose pathlengths are

discretized and placed in the appropriate grid pixel,  $a$  is the attenuative properties of the medium, and  $C$  is the observed attenuation in the experimental data. The values for the pathlength  $L$  values are identical to the one found from the speed of sound inversion.

In order to solve this problem, we follow the same sequence as the speed of sound algorithm by solving for the attenuation update via minimization of the same cost function and employing conjugate gradient updates. The choice of covariance matrices will differ in values to accommodate the parameter change as expected.

### 4.2.1 Generating Attenuation Data

To generate preliminary attenuation data, we first create an empirical matched filter from water shot data. Using the weighted Akaike Information Criterion (AIC) [13], we extract the window of each receiving pulse by determining the time that the pulse arrives, and as the criterion works symmetrically, the time the pulse finishes as well. The pulses are all then averaged together to produce a mean receive pulse.

To calculate attenuation, the complex signal energy ratio is used. The total complex energy for recorded RF data is given in [9]:

$$E = \int_{t_1}^{t_2} |I(t)|^2 dt \quad (4.2)$$

$t_1$  is given by the first arrival time-of-flight selection via the AIC picker, and  $t_2$  is a set window of time corresponding to the length of the empirical matched filter pulse.  $I(t)$  represents the amplitude envelope of the signal, which is calculated using the absolute value of the Hilbert transform of the signal.

Attenuation is then defined as:

$$\int_{ray} a_0 dl = 20 \log_{10} \frac{E_W}{E_O} = C \quad (4.3)$$

Where  $a_0$  represents the attenuation coefficient in dB/length, W represents water shot data, and O represents the object shot data. A direct ratio of the water

shot and the medium shot is not completely accurate due to the complex beam path of the acoustic wavefront. Some energy is lost to more complex interactions between the acoustic wave front and the medium, including diffraction, refraction, and scattering. The  $E_W/E_O$  term will be normalized with the amount of energy lost that is not due to energy absorption. Let the corrected energy of the measured object shot,  $E_O^m$  be defined as:

$$E_O^{m'} = AE_O^m \quad (4.4)$$

Where  $A$  is a correction factor that is obtained via the energy ratio found with simulated data:

$$A = \frac{E_W^s}{E_O^s} \quad (4.5)$$

The updated numerator in equation 4.3 follows:

$$\frac{E_W^m}{E_O^{m'}} = \frac{E_W^m}{E_O^m} \left( \frac{E_W^s}{E_O^s} \right)^{-1} \quad (4.6)$$

If the terms within the log reduce to 1, the attenuation is thereby 0 for that ray. This is expected because there is no energy variation between the water shot and the object shot, and thus, no attenuation. The correction factor will be obtained via a full wave simulation given the speed of sound map, which will be described further below.

## 4.2.2 Covariance Matrices

The choice of  $\sigma_d$  for the data covariance matrix corresponds to the maximum error expected in the data. The noise in experimental data will be gathered from energy calculations pertaining to rays that are only traversing water, coinciding with edge of each dataset in this setup.  $\sigma_d$  will be defined as:

$$\sigma_d = |\log_{10}(1 + dE)| \quad (4.7)$$

where  $dE$  is the maximum variation found in the energy ratio between simulated

and experimental data. For the model covariance matrix, we will set  $\sigma_m$  to be the maximum integrated attenuation expected in the reconstruction. Although the reconstructed attenuation values are not strictly Gaussian, as they should never be negative, the algorithm will still work as pointed out in [14].

### 4.2.3 Full Wave Model

To model wave propagation and scattering, the k-wave MATLAB toolbox was used. The algorithm is based on a spectral method which also utilizes a perfectly matched layer (PML) as a boundary condition to decrease the size of the domain to lower computation time and storage cost [15].

The simulation functions used in the k-wave toolbox are based on three coupled first-order equations:

$$\begin{aligned} \frac{\partial u}{\partial t} &= \frac{1}{\rho_0} \nabla \rho \\ \frac{\partial \rho}{\partial t} &= -\rho_0 \nabla \cdot u - u \cdot \nabla \rho_0 \\ p &= c_0^2 (\rho + d \cdot \nabla \rho_0) \end{aligned} \tag{4.8}$$

where  $\rho$  and  $p$  represents the density and pressure field and  $u$  and  $d$  correspond to particle velocity and displacement.

Each transducer element was modeled as a 400  $\mu\text{m}$  effective width element. The source signal is set to mirror the empirical matched filter in frequency and phase, but filtered and smoothed out to minimize undesirable transients in the wave computation. The recorded signal is computed for each receiver. Each field computation for every transmitter takes approximately 10 minutes on a 2.93 GHz i7 quad-core computer.

## 4.3 Results

### 4.3.1 Forward Wave Propagation Model

The field is modeled for each transmit and receive element pair for a total of 128 x 128 RF lines with and without the phantom. The complex signal energy ratio is calculated for each RF line of the simulated data to generate the effective attenuation caused by a diffractive medium with the speed of sound pattern images, but without homogeneous bulk attenuation, i.e., homogeneous absorption and isotropic scattering. The modeled field from the k-space algorithm matches well with the recorded RF data as far as capturing the energy lost due to diffraction and scattering (Fig. 4.1).

### 4.3.2 Experimental Data

Experimental data was acquired for a rubber (MF Plastics, Ft. Worth, TX) cylinder of 12.5 mm with a measured sound speed of 1406 m/s and 12 dB/cm attenuation coefficient at 3.5 MHz. The rubber cylinder was placed approximately in the center between the two transducers. The complex signal energy ratio was calculated for each recorded RF line for both the water shot and medium shot case (Fig. 4.2). To note, there is a dark line through both energygrams because element 26 on the transmitting transducer is not functioning properly.

The attenuation calculated from the difference of the complex signal energy ratios encompasses not only the bulk attenuation of the medium but also the effective attenuation caused by the more complex interactions such as diffraction and coherent scattering. The energy ratios do not represent a perfect match because of noise in the experimental data and slight discrepancies that may arise in the speed of sound distribution (Fig. 4.3).

To reconstruct the attenuation coefficient representative of the bulk of the properties of the materials imaged, the calculated ratio is normalized by the effective



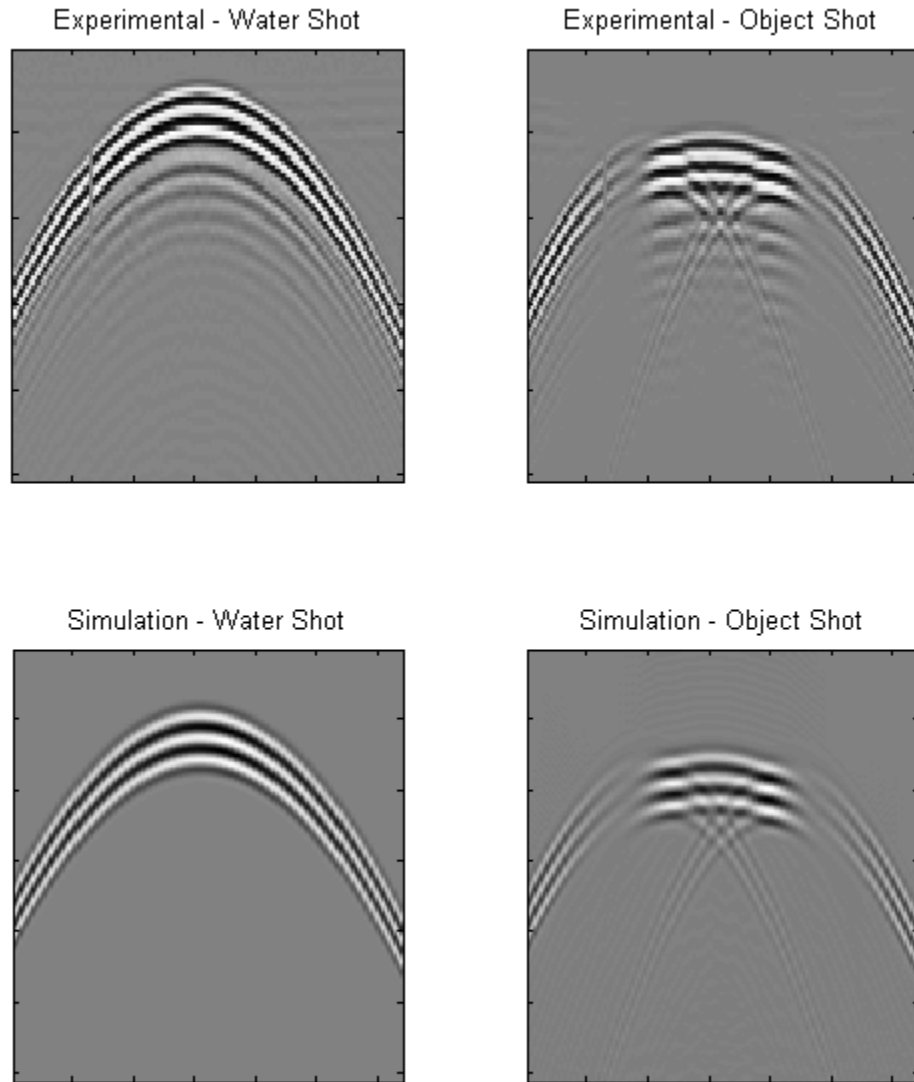


Figure 4.1: RF data recorded when transmitting with the 64<sup>th</sup> element on one array. The experimental and simulated shots are very similar to each other. The most important data to extract from the model are the bands outside the center portion (corresponding to the beam traveling by the edge of the cylinder) as the recorded energy is very small and greatly distort attenuation image reconstructions.

attenuation determined from the simulated data (Fig. 4.4). As all computations are based on the log scale, small differences below one are amplified unnecessarily. The energy ratios are adjusted by applying a DC offset of 1 to prevent minor discrepancies between simulated and experimental data from largely affecting normalization. Though the absolute values are slightly offset, the relative trend between both energy ratios is still monotonically preserved.

### **4.3.3 Reconstruction**

Using the pathlengths acquired from the speed of sound reconstruction, an initial attenuation image was first formed using a straight thick ray pathlength matrix using the normalized attenuation data. This seed image was then used with the final pathlength matrix to construct the final attenuation image.

In the inversion algorithm, local pixels within the object location were correlated with a coefficient of 0.01 to aid the inversion to reduce the smearing artifact as demonstrated in the previous chapter. The algorithm was able to reconstruct an attenuation image with the corrected attenuation data to give the correct shape to the low SOS cylinder (Fig. 4.5).

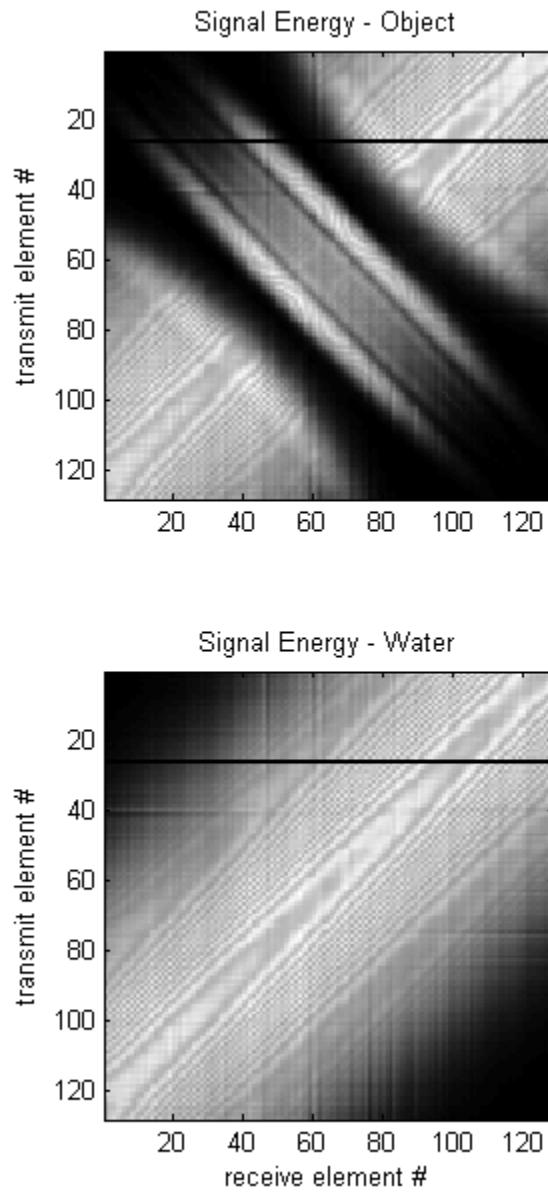


Figure 4.2: Raw signal energy data is shown, uncorrected. The large bands of low energy for the object data illustrate the diffraction and multipath phase cancellation of the wave at the edge of the low SOS cylinder.

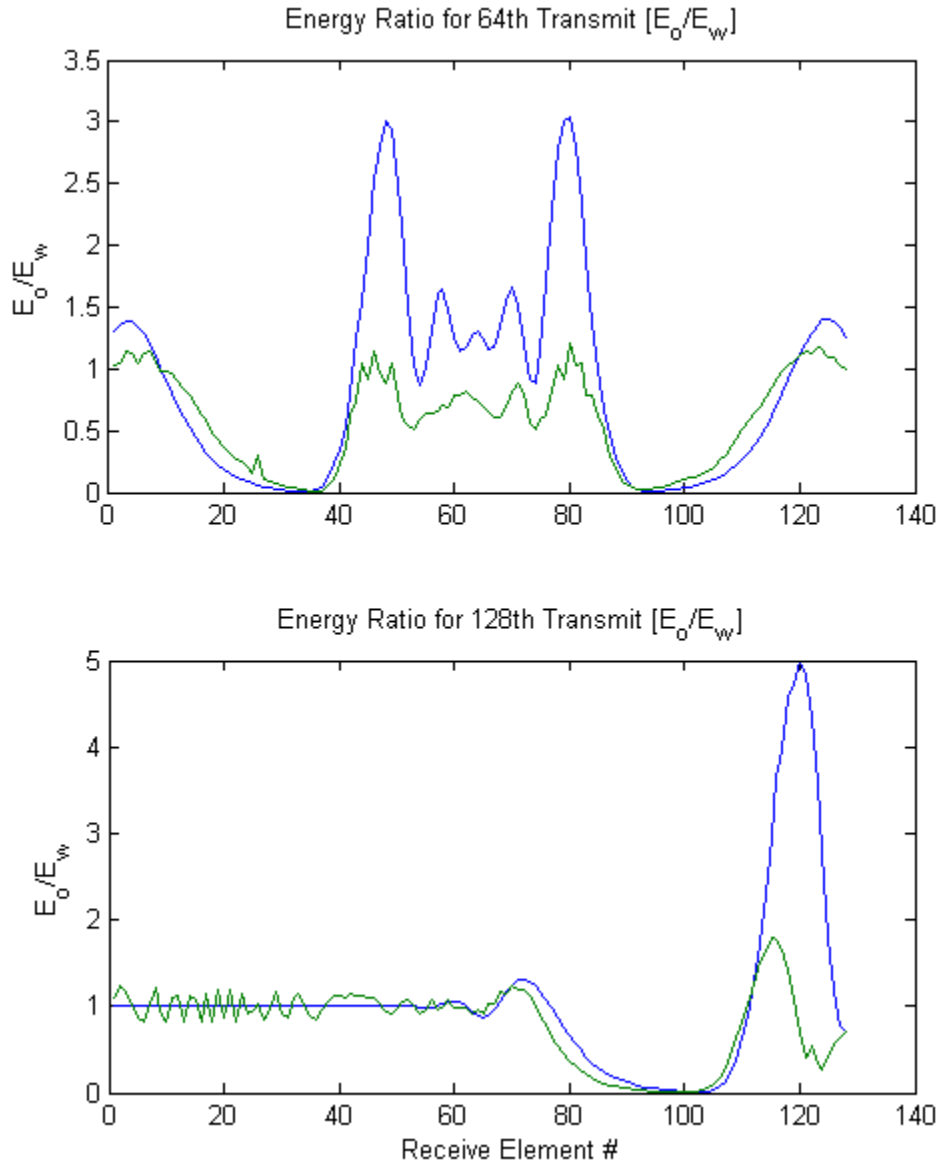


Figure 4.3: The energy ratio across the receivers when transmitting with the 64<sup>th</sup> element is shown. The dips in energy shown in experimental data (green) align closely with those found from simulation (blue).

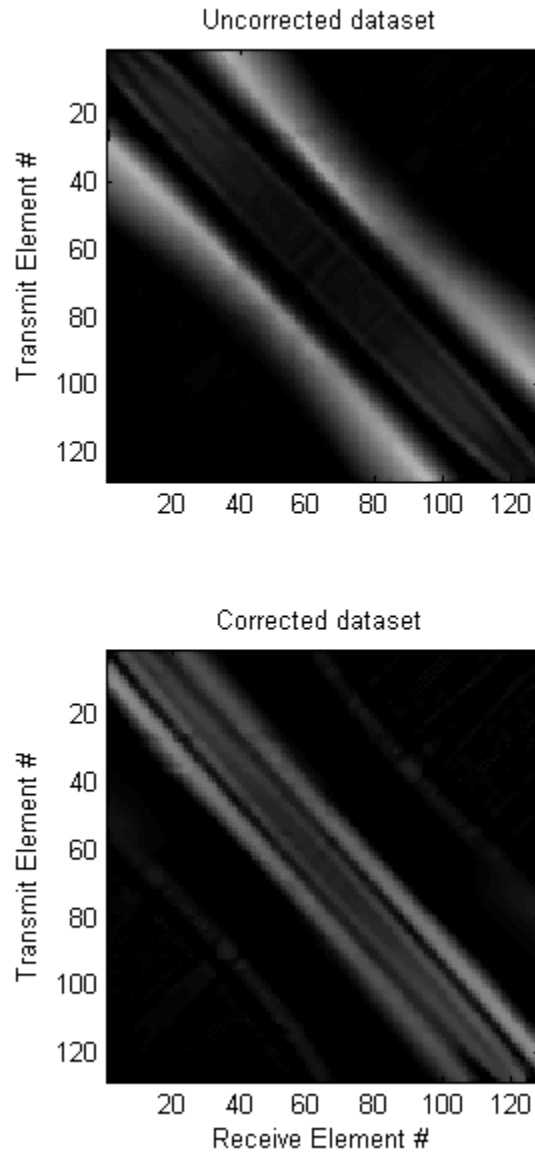


Figure 4.4: The corrected attenuation data (lower image) to be fed into the reconstruction algorithm is illustrated. The low energy bands corresponding to the edge of the cylinder are removed, while the beams that traverse the center of the cylinder indicate a much higher attenuation than the uncorrected data.

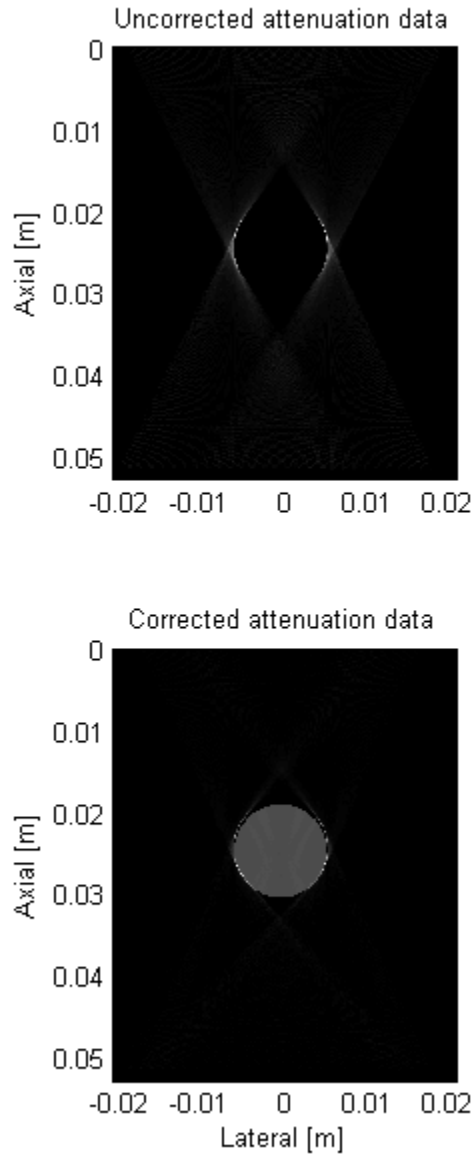


Figure 4.5: The resulting attenuation image using a weighted least squares model with *a priori* information is depicted for the uncorrected (top image) and corrected dataset (bottom). The cylinder is recovered with a high relative attenuation compared to the background of water when the dataset is corrected. When uncorrected, the resulting image shows only a strong silhouette of the contrasting cylinder with faint attenuation within the cylinder.

## 4.4 Discussion

The algorithm used to reconstruct the attenuation image is analogous to the method used for speed of sound images, except that the covariance matrices hold different values to account for the physical values expected in each respective problem. The advantage of this approach is the flexible regularization to account for this information, and also the ability to regularize spatially based on expected homogeneous areas of the medium, or at least areas one is willing to treat as homogeneous. This benefit is particularly useful in the limited aperture configuration because we lack information from all viewing angles. Incorporating *a priori* information in the model covariance matrix aids the inversion to reduce smearing artifacts caused by limited viewing angles.

Regular attenuation tomography methods differ from each other primarily in the method of generating the attenuation data to be fed into the inverse problem. Some algorithms account for the refraction of beam paths and account for the changing pathlength to improve attenuation images [11, 12]. An example of attenuation correction is to modify the attenuation data by a constant attenuation factor based on the traversal of the bending beam ray path. Examining the signal energy from the obtained phantom data (Fig. 4.2), it can be seen that there is excessive energy loss corresponding to the edge of the cylinder. This energy loss is not due to the bulk, isotropic, attenuative properties of the medium, but rather because of the diffracting wave that is not recorded by the receiving transducer. This error is exacerbated when acquiring with only a limited aperture, since the wayward wave due to diffraction and/or scattering as a result of variable sound speed is not recorded at all. Correcting for this phenomenon via pathlength traversal would be insufficient to produce reasonable attenuation images in this geometry.

The acoustic wavefront is diffracted mostly at the edges of speed of sound contrasts as noted in our simple phantom experiment data. Without properly

accounting for this energy loss, the calculated attenuation would therefore be much higher than the actual attenuation due to energy absorption and isotropic scattering in tissue. This suggests that attenuation images constructed with traditional algorithms without sufficient correction would be highly edge enhanced, which has been observed in essentially all high speed lesions in transmission tomography studies of attenuation imaging of the breast [1–7, 9, 10]. The same figure (Fig. 4.2) illustrates the constructive and destructive interference of waves as they pass through the center of the cylinder. This phenomenon illustrates how second-arrival effects can affect the energy calculation, and thus it is necessary to use short transmission, or at least wide bandwidth, pulses to be able to isolate first arrival from second-arrival interactions. This aberration is also most pronounced when inclusions have a high speed of sound compared to the background.

To model the forward acoustic field, a k-space algorithm was implemented using a known speed of sound map of the medium. Proper modeling relies on accurate knowledge of the transducer element positions, which have been solved with an inverse problem using water shot data. A simpler 2D forward solver was chosen to reduce computation time since the imaged object is a cylinder, whose long axis is parallel to the long axes of the elements on the transducer. There is a current assumption that diffraction of the wave outside of the plane of the transducer is small, which is reasonably valid in this cylindrical experimental geometry, given that the modeled field closely aligns with the field recorded with the transducer.

It is important to note that the modeled field is only an approximation of the field recorded at the transducer elements. To obtain more accurate results, the forward model can be improved by performing an accurate characterization of the transducer. The characterization would relate the transducer response to an effective source to input in the model in order to generate a field that matches well in both phase and amplitude. This process is an inverse problem in and of itself and may be very time



consuming as it is extremely sensitive to error due to the operating wavelengths of ultrasonic transducers. However, as we are not using the field information to solve an inverse problem based on wave fields, but rather as an approximate normalization of attenuation data, this method is sufficiently accurate for our purposes.

A similar method is employed in [12] to account for refraction due to a known speed of sound distribution using the angular spectrum method. While the angular spectrum method for wave propagation is fast to compute, it does not model variations in the x and y-directions as well as the propagating z-direction. A straight path assumption is also used in their reconstruction of the attenuation coefficient map, and any data not satisfying this criterion was discarded. We choose to implement a full-wave model to account for the different effects of wave propagation in a variable velocity medium and also to accommodate bending ray paths, albeit at the expense of some computation time.

The data is normalized based on computed energy because this method is more robust than adjusting the raw amplitudes. The reasoning is similar to attenuation imaging using the complex signal energy ratio because the amount of noise affecting the data is largely decreased in comparison to an amplitude based method. Also, normalizing based on the ratio of background to object data is also ideal because it takes into account possible errors, known and unknown, in the forward model, including not adjusting for receive element sensitivity and also numerical artifacts that would be present in both object and water shot simulations.

The corrected dataset is not perfect, as there is still some noise present that corresponds to the edges of the diffracted wave (Fig. 4.4). The algorithm does not aim for a perfect correction because in a practical problem there can be multiple sources of errors; for example, the true velocity distribution will vary slightly from the reconstructed speed of sound, which will result in an imperfect match with the forward model. Instead, the goal of the algorithm is to provide a robust approach

that can account for such discrepancies, and with the use of the covariance based algorithm, data errors can be readily provided for in the data covariance matrix as well. The use of energy ratios within this minimization problem demonstrates that a relative attenuation image can still be reconstructed in the presence of noise.

Without the needed correction, the resulting attenuation image is, as expected, highly edge enhanced (Fig. 4.5, top image). This effect is most pronounced in this geometry because there is missing information using only a limited angle aperture, and because the phantom used for this experiment also represents a high SOS contrast scenario with a high amount of diffraction present and signal loss that is not attributed to energy absorption and isotropic scattering. When imaging a compressed breast, as the acoustic beam is traveling through a thick block of tissue that extends the length of the aperture, the extent of diffraction and lost energy usually should be considerably less, except for high speed of sound masses in fatty breasts.

The computation time of a full wave forward model for a complete dataset is not trivial. However, the needed computation is not overwhelming since the field need only be calculated once and does not require iterations. Furthermore, as the problem is highly parallel, the task can be easily divided over a computing cluster based on the number of transmitters in the problem to greatly reduce overall computation time.

This normalization approach can and should be readily extended to 3D by converting the forward model into a 3D model, and also acquiring a 3D volume set with the paired transducers, which shall be investigated for future more complex phantoms and *in vivo* studies. The 3D model will account for energy lost out of the imaging plane, and thereby be essential for reconstructing accurate attenuation images of complex objects. The MATLAB k-wave toolbox supports 3D modeling, so the existing code can be easily extended.

We need to note that the formation of the attenuation image is highly reliant on the sound velocity distribution for two reasons: (1) the speed of sound reconstruction algorithm provides the pathlength matrix  $L$  by which to solve the attenuation inverse problem and (2) the speed of sound map is required to compute the necessary normalization to account for extraneous energy loss. Coupled with the precise knowledge of transmit and receive locations and a 3D mode of the forward solver, this algorithm is readily applicable to more complex phantoms and *in vivo* data as well.

Although the range of viewing angles is decreased, there are a few advantages to the opposing array setup. In the compressed breast, the overall travel thickness is smaller which enables the use of a higher central carrier frequency for B-mode imaging, and therefore, increased resolution and soft tissue contrast, without excessive signal attenuation. When compared to a free-floating breast, the reduced thickness and the flattening of some structures decreases the amount of complex acoustic interaction such as refraction and multiple scattering [16, 17]. Furthermore, with a lower overall thickness, the size of the domain is also decreased, which eases the computation storage and time required of full-wave solvers. Also, dealing with transmission instead of pulse echo data is advantageous as most of the energy of the acoustic wave is transmitted, with only a small portion backscattered [18]. Lastly, this acquisition mode will also enable co-registration with other modalities obtained in this geometry including mammography, tomosynthesis, and photoacoustics.

The next logical step to validate this algorithm will be to implement a 3D forward model and modify the acquisition setup to accommodate 3D volume acquisitions, which will be investigated in a future study. With the aforementioned improved setup, more complex phantoms and *in vivo* studies can be readily imaged with the proposed algorithm.

## 4.5 Conclusion

In the opposed array geometry, attenuation images can be reconstructed side by side with speed of sound images using the same RF data. Correction of the attenuation data is implemented using a forward model of the expected diffraction based on a variable speed of sound map with no attenuation due to energy absorption. The corrected attenuation data is then fed into the covariance based inverse problem to reconstruct an attenuation image with limited viewing angles. Results show that the attenuation data is highly improved with this correction. Small studies over several decades indicate that obtaining both speed of sound and attenuation maps should be useful for diagnosis of breast cancer lesions. When acquired in this geometry, both imaging modes enable co-registration with companion modes and modalities such as B-mode ultrasound, tomosynthesis, and photoacoustic imaging. We suspect these techniques will become particularly useful in breast cancer screening, but no screening studies have been performed.

## BIBLIOGRAPHY

- [1] G. H. Glover, “Computerized time-of-flight ultrasonic tomography for breast examination,” *Ultrasound in Medicine & Biology*, vol. 3, pp. 117–127, Jan. 1977.
- [2] J. F. Greenleaf, S. A. Johnson, and A. H. Lent, “Measurement of spatial distribution of refractive index in tissues by ultrasonic computer assisted tomography,” *Ultrasound in Medicine & Biology*, vol. 3, pp. 327–339, Jan. 1978.
- [3] J. F. Greenleaf and R. C. Bahn, “Clinical Imaging with Transmissive Ultrasonic Computerized Tomography,” *Biomedical Engineering, IEEE Transactions on*, vol. BME-28, pp. 177–185, Feb. 1981.
- [4] A. L. Scherzinger, R. A. Belgam, P. L. Carson, C. R. Meyer, J. V. Sutherland, F. L. Bookstein, and T. M. Silver, “Assessment of ultrasonic computed tomography in symptomatic breast patients by discriminant analysis,” *Ultrasound in medicine & biology*, vol. 15, no. 1, pp. 21–28, 1989.
- [5] M. P. André, C. H. Barker, N. Sekhon, J. Wiskin, D. Borup, and K. Callahan, “Pre-Clinical Experience with Full-Wave Inverse-Scattering for Breast Imaging Acoustical Imaging,” vol. 29 of *Acoustical Imaging*, ch. 10, pp. 73–80, Dordrecht: Springer Netherlands, 2009.
- [6] N. Duric, P. Littrup, E. West, B. Ranger, C. Li, and S. Schmidt, “In-vivo imaging of breast cancer with ultrasound tomography: probing the tumor environment,” *Proceedings of SPIE*, vol. 7968, pp. 796812+, Mar. 2011.

- [7] S. A. Johnson, T. Abbott, R. Bell, M. Berggren, D. Borup, D. Robinson, J. Wiskin, S. Olsen, and B. Hanover, “Non-Invasive Breast Tissue Characterization Using Ultrasound Speed and Attenuation Acoustical Imaging,” in *Acoustical Imaging* (M. P. André, I. Akiyama, M. Andre, W. Arnold, J. Bamber, V. Burov, N. Chubachi, K. Erikson, H. Ermert, M. Fink, W. S. Gan, B. Granz, J. Greenleaf, J. Hu, J. P. Jones, P. Khuri-Yakub, P. Laugier, H. Lee, S. Lees, V. M. Levin, R. Maev, L. Masotti, A. Nowicki, W. O’Brien, M. Prasad, P. Rafter, D. Rouseff, J. Thijssen, B. Tittmann, P. Tortoli, A. Steen, R. Waag, and P. Wells, eds.), vol. 28 of *Acoustical Imaging*, ch. 17, pp. 147–154, Dordrecht: Springer Netherlands, 2007.
- [8] A. C. Kak and K. A. Dines, “Signal Processing of Broadband Pulsed Ultrasound: Measurement of Attenuation of Soft Biological Tissues,” *Biomedical Engineering, IEEE Transactions on*, vol. BME-25, pp. 321–344, July 1978.
- [9] C. Li, N. Duric, and L. Huang, “Breast Imaging Using Transmission Ultrasound: Reconstructing Tissue Parameters of Sound Speed and Attenuation,” *BioMedical Engineering and Informatics, International Conference on*, vol. 2, pp. 708–712, 2008.
- [10] R. Jirik, R. Stotzka, and T. Taxt, “Ultrasonic attenuation tomography based on log-spectrum analysis,” in *Medical Imaging 2005*, vol. 5750, pp. 305+, The International Society for Optical Engineering., Apr. 2005.
- [11] S. Li, M. Jackowski, D. P. Dione, T. Varslot, L. H. Staib, and K. Mueller, “Refraction corrected transmission ultrasound computed tomography for application in breast imaging.,” *Medical physics*, vol. 37, pp. 2233–2246, May 2010.
- [12] S.-W. Huang and P.-C. Li, “Ultrasonic computed tomography reconstruction of

- the attenuation coefficient using a linear array,” *Ultrasonics, Ferroelectrics and Frequency Control, IEEE Transactions on*, vol. 52, pp. 2011–2022, Nov. 2005.
- [13] C. Li, L. Huang, N. Duric, H. Zhang, and C. Rowe, “An improved automatic time-of-flight picker for medical ultrasound tomography,” *Ultrasonics*, vol. 49, pp. 61–72, Jan. 2009.
- [14] M. Haynes and M. Moghaddam, “Large Domain, Low-Contrast Acoustic Inverse Scattering for Ultrasound Breast Imaging,” *IEEE transactions on bio-medical engineering*, July 2010.
- [15] B. T. Cox, S. Kara, S. R. Arridge, and P. C. Beard, “k-space propagation models for acoustically heterogeneous media: Application to biomedical photoacoustics,” vol. 121, pp. 3453+, June 2007.
- [16] O. M. Bucci, N. Cardace, L. Crocco, and T. Isernia, “Degree of nonlinearity and a new solution procedure in scalar two-dimensional inverse scattering problems,” *J. Opt. Soc. Am. A*, vol. 18, pp. 1832–1843, Aug. 2001.
- [17] P. L. Carson, B. Wang, G. L. LeCarpentier, M. M. Goodsitt, C. Lashbrook, R. Pinsky, G. Narayanasamy, J. B. Fowlkes, and K. Saitou, “Local compression in automated breast ultrasound in the mammographic geometry,” pp. 1787–1790, Oct. 2010.
- [18] F. Simonetti, L. Huang, N. Duric, and P. Littrup, “Diffraction and coherence in breast ultrasound tomography: a study with a toroidal array,” *Medical physics*, vol. 36, pp. 2955–2965, July 2009.

## CHAPTER V

# Reconstruction Algorithm Refinements for Grayscale, Speed of Sound, and Attenuation Imaging

### 5.1 Summary of Developed Algorithms

In the previous chapters, proposed algorithms for, but not limited to, the compressed breast geometry improved grayscale beamforming, speed of sound reconstructions, and attenuation imaging. Beamforming was addressed in the form of an upcoming reconfigurable array technology, which allows for superior B-mode ultrasound images because reconfigurable arrays are amenable to annular beamforming. Not only does annular focusing have improved elevational focus in comparison to linear arrays, but using reconfigurable arrays also remove the need to mechanically translate the array which decreases image quality due to backlash and possible misalignment.

To reconstruct speed of sound images, a forward model based on the eikonal wave equation using first-arrival traveltimes was used to develop a cost function. Solving the cost function via regularization yielded speed of sound updates, and through iteration the speed of sound map was recovered. The advantage of the proposed cost function lies in the fact that it is based on two spaces, a model space, and a data space, which enables elegant regularization without the need for fine detail tweaking. The regularization parameters are based on true physical values expected within the reconstruction. The developed cost function also enables regularization in the model



space that incorporates *a priori* information of homogeneous regions, which is shown to minimize the inherent streaking artifacts inherent with limited viewing angles.

Attenuation imaging was approached using the same method. However, as the ultrasound beam diffracts when it passes through a different speed of sound, the recorded signal is not only comprised of the attenuation of the beam as it passed through the object, but also of the amount of energy lost due to wayward scattering. In order to generate a viable attenuation image, the attenuation data is first normalized using the known speed of sound map, and then fed into the cost function. Using similar regularization methods as the speed of sound algorithm, an attenuation image is then recovered properly.

## 5.2 Future Work

There are many avenues to further explore and improve the proposed algorithms in this dissertation. Testing the beamforming proposed in Chapter 2 would be primarily a hardware effort, which can be done when the reconfigurable hardware is ready. Current efforts to produce a usable reconfigurable array are well underway, and should be obtainable within a few years.

The speed of sound and attenuation work explored in this dissertation has been primarily based on phantom studies and algorithm development in a 2D setting. A very natural and logical next step would be to image a more complex phantom or a breast tissue specimen. This allows a stable, controlled environment to continue testing the algorithm and address any particular nuances that might arise when imaging tissue instead of a well-behaved phantom.

After various attempts and experiments, we found that an absolute must in reconstructing accurate speed of sound images, especially in the compressed geometry, is that the transducers are placed in a fixed, known, location. The given setup with two opposed linear arrays satisfies such requirements in a phantom

study environment. As the ultimate goal of the imaging method is to move to a clinical setting for patient screening, an imaging system must be built that can accommodate patient movement without allowing for any transducer movement during an acquisition. Placing the setup within a water bath is also most practical in order to achieve convergence within the speed of sound reconstruction problem.

For further refinements with attenuation imaging, a 3D full wave model should be implemented for normalization when moving to more complex phantoms and/or breast tissue specimens. 2D simulations were sufficient in the current work because the imaged object was a cylindrical phantom. Adding the extra dimension will be necessary to capture out of plane energy loss with a more complex imaged object.

Lastly, using 2D arrays will be ideal for both speed of sound and attenuation imaging because they are both inherently 3D problems. Using dual opposed 2D arrays will allow us to use information when the ultrasound beam is diverted off the elevational plane, thereby increasing information for the already severely underdetermined problem because we only have limited viewing angles. However, this is inherently a hardware limitation as 2D arrays are not as prevalent, and much more expensive, than 1D linear arrays. Thus, acquiring 3D volume datasets with a pair of translating arrays will be the intermediate goal, making sure that the relative locations of both transducer's elements are known precisely to orders of a wavelength.